Electronic Theses and Dissertations, 2004-2019

2004

Thermal Management, Beam Control,and Packaging Designs For High Power

Te-yuan Chung
University of Central Florida

Showcase of Text, Archives, Research & Scholarship

THERMAL MANAGEMENT, BEAM CONTROL, AND PACKAGING DESIGNS FOR HIGH POWER DIODE LASER ARRAYS AND PUMP CAVITY DESIGNS FOR DIODE LASER ARRAY PUMPED ROD SHAPED LASERS

by

TE-YUAN CHUNG
BS in Physics, National Tsing Hua University, 1993
MS in Physics, National Central University, 1996
MS in Optics, University of Central Florida, 2001

A dissertation submitted in partial fulfillment of the requirements
for the degree of Doctor of Optics
in the College of Optics and Photonics
at the University of Central Florida
Orlando, Florida

Fall Term
2004

ii

ABSTRACT

Several novel techniques for controlling, managing and utilizing high power diode lasers are described. Low pressure water spray cooling for a high heat flux system is developed and proven to be an ideal cooling method for high power diode laser arrays. In order to enable better thermal and optical performance of diode laser arrays, a new and simple optical element, the beam control prism, is invented. It provides the ability to accomplish beam shaping and beam tilting at the same time. Several low thermal resistance diode packaging designs using beam control prisms are proposed, studied and produced. Two pump cavity designs using a diode laser array to uniformly pump rod shape gain media are also investigated.

ACKNOWLEDGMENTS

TABLE OF CONTENTS

LIST OF FIGURES

LIST OF TABLES

LIST OF ABBREVIATIONS

BCP   Beam Control Prism

BCPP   Beam Control Prism Package

FWHM   Full Width at Half Maximum

VCSEL   Vertical Cavity Surface Laser

ESP   Evaporated Spray Cooling

1. INTRODUCTION

The diode laser is a very special type of laser. It has several interesting properties which are quite different from ordinary lasers.   The most attractive property is its outstanding high efficiency which typically can reach 45-50%. 65% wall-plug efficiency has been reported recently.[1,2] Also, the output power can be as high as 2 W per emitter from a volume less than 0.01 mm^3. However, the trade offs are high divergence angles, an astigmatic output beam and extremely high heat flux. Also, multi-transverse modes and multi-longitudinal modes are not preferred in some applications. When making a diode laser array, the total output power will grow linearly with respect to the number of emitters, yet the thermal management of such an array will be a non-trivial problem. In addition, each emitter is incoherent with the other emitters. The whole array operates as an incoherent line of discrete emitters which limits the applications of the diode array.

Figure 1.1 shows the techniques we propose and/or develop to improve or to use the high power diode laser array. Since the heat flux of the diode laser array is one of the major limits to its use, we introduce spray cooling which has a high heat transfer coefficient. To reduce thermal resistance as much as possible, we propose a beam control prism package (BCPP) which makes possible much shorter cooling paths compared to traditional stack packaging. BCPP, as its name implies, needs beam control prisms (BCPs) to make it feasible. It is an innovative idea to combine a prism and lens in one piece. BCP can reduce or collimate the fast divergence angle of the diode laser. It also provides the ability to aim the output beam to a specific direction. To achieve total

1

control of the diode laser beam, we propose to use a micro cylindrical lens array to manage the slow divergence angle as well as a BCP to control the fast divergence angle.

Spray Cooling

Beam control prism package (BCPP)

Beam Control Prism (BCP)

Micro cylindrical lens array

Diode laser array
Efficiency ~ 50%
Optical power ~ 2 W/emitter
Output linewidth ~ 3 nm
Heat flux ~ 1.3×10^7 W/m^2
Operating temperature < 60°C
Fast divergence angle (FWHM) ~ 35°
Slow divergence angle (FWHM) ~ 10°

Laser machining

Diode pumped solid state lasers

Pump cavity design for rod shape gain media

Coherent coupling of emitters

Figure 1.1: Diode laser array properties and related techniques and applications

The considered high power light source can be used in material processing if the aforementioned undesired optical properties can be controlled. Also, the high power diode can be a great light source for pumping solid state lasers because of its high efficiency and narrow linewidth. However, its light emitting direction and distribution is quite different from a traditional flash lamp. Special arrangements for diode position and/or pump cavity design have to be made to achieve uniform gain distribution in the laser material. We conducted a systematic study of pump cavity design for rod shape gain media pumped by a standard, commercially available stack packed diode laser array.

2. DIODE LASER ARRAY PROPERTIES

2.1 Basic physic concepts of the diode laser [3,4]

The most commonly used materials for diode lasers are GaAs and other III-V elements. The energy difference or the bandgap between the valence band and the conduction band is the origin of the laser action. Essentially, a diode laser and a LED have a similar semiconductor structure. Both of them use a forward biased p-n junction to inject electrons and holes to generate light emission. However, the diode laser has an optical resonator which is basically a waveguide for an edge emitting laser diode. The resonator confines the emitting light between the end "mirrors" of the resonator. The mirrors can be distributed Bragg gratings, multilayer dielectric HR coatings, or even Fresnel reflection from cleaved end surfaces if the gain in the active region is high enough. Population inversion is the necessary condition for positive gain. Figure 2.1 shows the very basic concept of a diode laser achieving population inversion by the application of forward bias. Quasi-Fermi levels of p-type and n-type semiconductors are separated and population inversion is achieved in the active region. Therefore, a resonance cavity can be set up along the active region. For better efficiency, better mode confinement and better transparency outside the active region, several complicated semiconductor structures are employed.
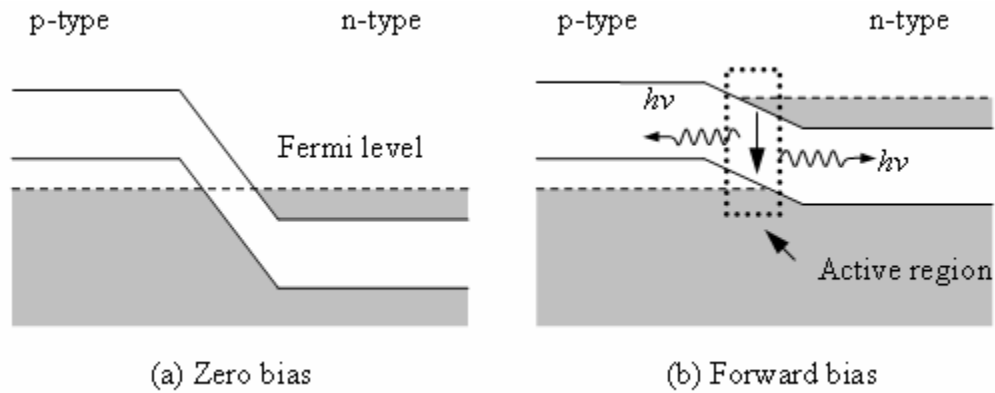
Figure 2.1: Energy band structure of a diode laser

Considering the cavity and laser emission direction, the diode laser can be categorized into two major groups: edge emitting and surface emitting. Figure 2.2 shows the basic structure of a surface emitting diode or vertical cavity surface laser (VCSEL) [5]. Since the gain length is relatively short, the output power is lower than possible for edge emitters. Because of its shorter cavity length, the VCSEL has larger free spectral range and it generates single longitudinal mode. Its aperture is usually wider than that of an edge emitter allowing multiple transverse modes in its output. The VCSEL aperture is generally circular which gives the output beam cylindrical symmetry. As the figure shows the substrate is actually much thicker than the laser structure so that the active region is close to the p-electrode.
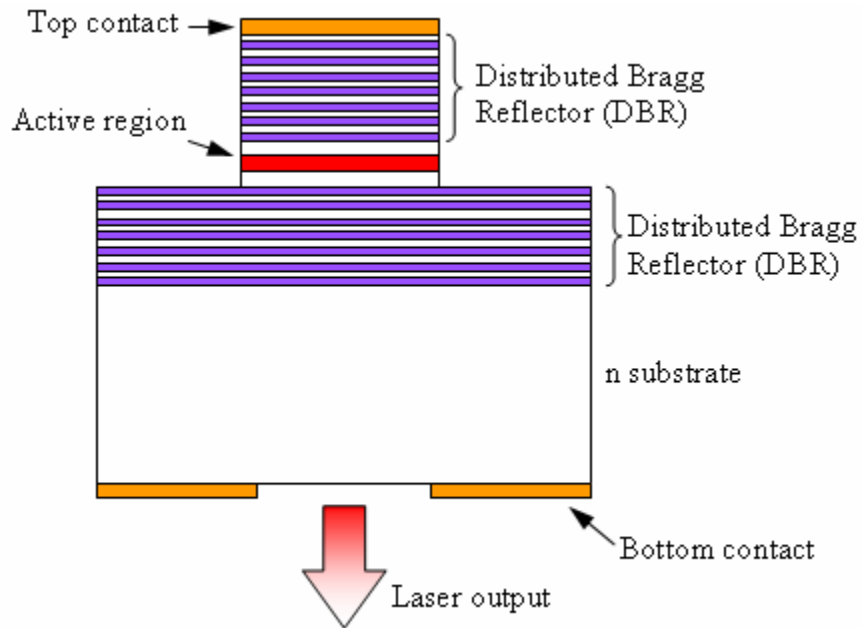
Figure 2.2: Structure of a surface emitting diode

Figure 2.3 shows the basic structure of an edge emitting diode laser. Since the active region is long it is much easier to achieve higher output power than in a VCSEL. That's the reason all of the high power diode laser arrays are currently made of edge emitting diodes. Nevertheless, because of the extremely high gain of semiconductor lasers, a longer cavity also implies that multiple longitudinal modes will arise. Typically the thickness of the active region is about 1 μm but the width is always much larger: about 100-150 μm for a typical high power diode laser emitter. This structure allows an edge emitting diode to achieve high output power at the cost of unsatisfactory output beam properties. Along the thickness direction, the aperture size is about the laser wavelength giving the output beam a large divergence angle in this direction. It is called the fast divergence angle and is typically about 60° at full angle or 35° at full width at half maximum of the power (FWHM). Along the width direction, the diode aperture is

much larger than the wavelength; consequently, the divergence angle is smaller. However, because the active area is too wide, multi-transverse modes and amplified spontaneous emission (ASE) occur in this direction. It makes the divergence angle larger than that of an ideal Gaussian beam. A typical slow divergence angle is about 10° at full angle or 5° FWHM. The active region is also close to p-electrode because the substrate is much thicker than the diode laser structure as shown in Figure 2.3.

The semiconductor bandgap becomes smaller when its temperature increases. Therefore, the output wavelength of a diode laser increases with increasing temperature. The GaAs output has a temperature coefficient 0.273 nm/K. The diode laser we use is $Ga_{1-x}Al_xAs$ where x equals 0.08 or the emission wavelength is about 808 nm. Its temperature coefficient is 0.28 nm/K which is slightly higher than GaAs.

The life expectancy of a laser diode is expected to decrease about 50% if the temperature increases 10ºC. This is because the impurity dopants tend to diffuse to other areas. The higher the temperature is, the higher the mobility the dopants have, and the faster the diffusion process will be.
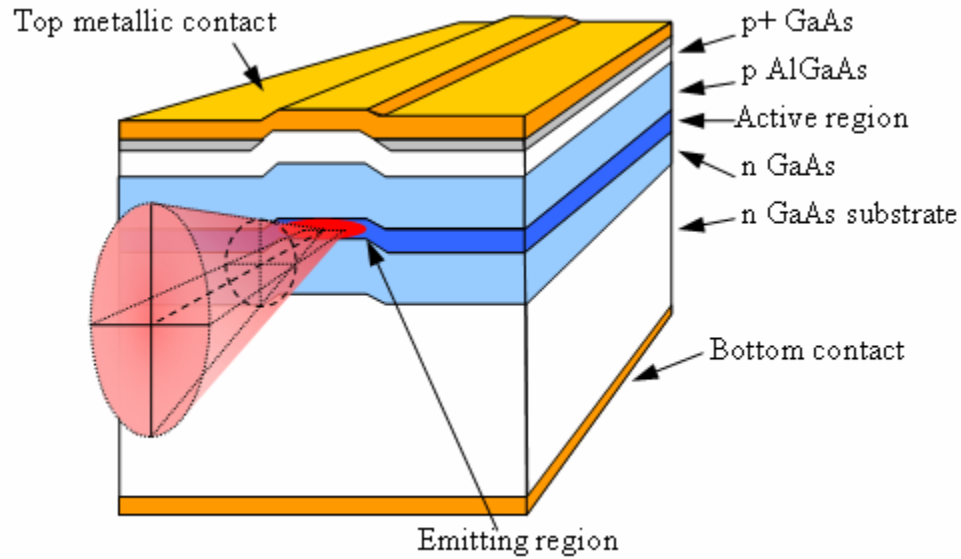
Figure 2.3: Structure of an edge emitting diode

2.2 Thermal properties

The diode laser has a longer lifetime, lower threshold, shorter output wavelength, and better efficiency when operating at lower temperatures[4]. Thus, keeping the emitter temperature as low as possible is essential to good operation of diode lasers. Even though the typical efficiency can reach about 50% [6], the diode laser generates 50% of waste heat that must be dissipated through a tiny area. Figure 2.4 shows the heat flux versus the temperature of various systems. There is no direct way to cool a laser diode. We can either increase the heat transfer surface area and/or use a high heat transfer coefficient method to remove the waste heat. When using a single emitter large area heat spreading can be utilized to reduce the demand on the cooling system. However, a high power, high emitter density, diode laser array might not allow large area heat spreading. Considering a typical diode laser array stack with bar-to-bar spacing of 1 mm, assume 40

W bars are used and 50% efficiency is achieved. Such an array generates a heat flux of about 400 W/cm^2 that needs to be removed or else the diodes will heat up and fail catastrophically.
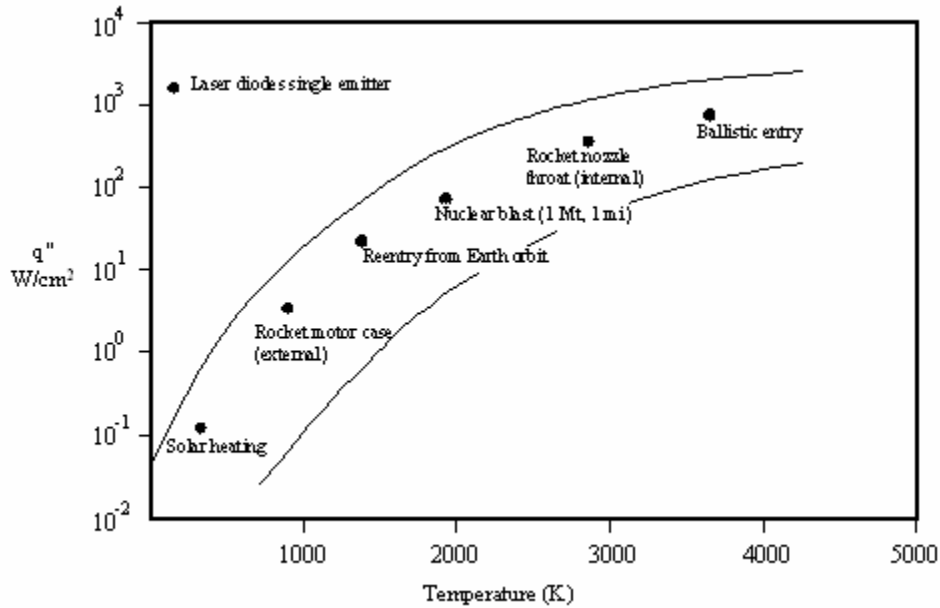
Figure 2.4: Heat flux versus temperature of various systems

There are several techniques available for the thermal management of high power diode arrays. The most mature technology employs a conventional cold-water heat exchanger which has many fins in the heat exchanger to increase the surface area. A typical heat exchanger cools a diode array of 2 cm^2 (made of 40 W bars) and requires a water flow rate of approximately 4 gpm at 10° C to maintain the emitters of this power level within a desired temperature range. This flow rate results in a pressure drop across the heat exchanger of approximately 30 psi or 20.7 nt/cm^2. Larger diode arrays will require many such heat exchangers. The size of the coolant pump and amount of coolant

8

has to be scaled up. For a high-energy laser when the size of diode arrays is increased

from a few cm^2 to several hundreds cm^2, this cooling technique will likely lead to an

unacceptably large thermal subsystem.

A more sophisticated approach to cooling high power diode arrays involves the use

of micro/macro channels that are etched into metal or silicon.[7] This technology is very

effective in the acquisition of heat. The coolant flow rate is determined by the allowable

temperature rise within the diode array and the pressure drop across the micro/macro

channels. Heat acquired by the coolant causes the temperature of the coolant to increase

in the flow direction. Thus the need for temperature uniformity would require the flow

rate to be high. However, since the micro/macro channels are very small, pressure drop

limitations restrict the coolant flow rate possible.

In our experiment, we use low pressure water spray cooling to achieve a high heat

transfer coefficient. Spray cooling will be discussed in detail in Chapter 3.

It is also important to consider the packaging of the diode array. A good package

not only will use a good cooling method, but also will use large thermal conductivity

materials to spread the heat and shorten the distance between emitter and coolant as much

as possible. In any such package the emitted light must be extracted efficiently and with

sufficient control to enable desired applications.

2.3 Optical properties

The most undesirable optical property of the edge emitting diode laser is the

astigmatic output beam. As mentioned above, the fast divergence axis is along the

thickness direction of the active area and the slow divergence axis is along the width

direction. A typical fast divergence angle is about 60° at full angle (or 35° FWHM). If we need to collimate the beam the collimating optic will have f/0.87 or even smaller to collect 95% of the light assuming a Gaussian beam. Fortunately, because of the small aperture size the output in the fast axis direction is still a single transverse mode. Also, for a diode bar, as shown in Figure 2.5 all the emitters can share a common cylindrical lens to control the fast divergence angle because the emitters are in a line parallel to the slow divergence axis and perpendicular to the fast divergence axis[4].
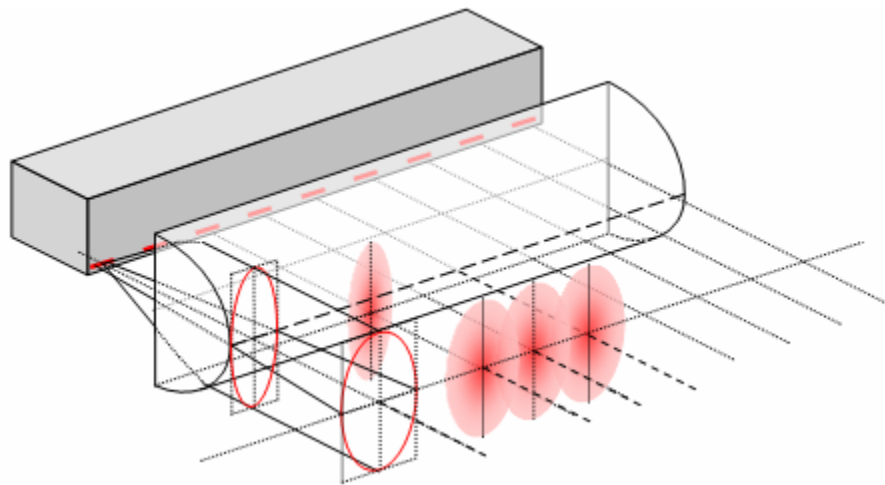
Figure 2.5: All emitters in a diode bar can share a cylindrical lens

The slow divergence axis has totally different properties. Its larger aperture size allows multiple transverse modes and ASE. An edge emitting laser diode built for high power can be as wide as 100-150 μm making its optical properties become more like those of an incoherent line source. The typical slow divergence angle is about 10° at full angle or 5° FWHM. For an incoherent line source, there is no simple geometric optical way to collimate the light without throwing away power. However, if we know the exact

position where we want to focus, we can use micro cylindrical optics to image the

emitters to the working plane. However, the image we have will still be an incoherent

line source. More details will be discussed in Chapter 6.

3. THERMAL MANAGEMENT AND SPRAY COOLING

The removal of waste heat from diode lasers is, as we mentioned in Chapter 2, one of the major issues in utilizing high power diode laser arrays. In this chapter, we discuss the basic physics of cooling and spray cooling which we proposed and applied to a high power diode laser array.

3.1 Thermal conduction and convection [8]

Heat transfer is energy in motion due to a temperature difference. Here we discuss the simple heat transfer mechanisms we utilize in our experiments and simulations. There are three different heat transfer modes: conduction, convection and radiation. Since the radiation effect is negligible when the subject temperature and the ambient temperature are close, we will focus mainly on heat conduction and convection.

The rate equation for heat conduction is also known as Fourier's law

$$q''_x = -k \frac{dT}{dx} \tag{3.1}$$

The heat flux q_x'' (W/m^2) is the heat transfer rate in the x-direction per unit area perpendicular to the direction of transfer. It is proportional to the temperature gradient, dT/dx. The coefficient k is the thermal conductivity (W/m·K), a property of the material through which the heat transfer takes place. The minus sign indicates that the direction in

which the heat flux is transferred toward a lower temperature. A more general form of the time independent heat conduction equation is

$$\bar{q} = -k\nabla T \tag{3.2}$$

Here, q is the vector form of heat flux. If we consider heat generation as well, the equation is

$$\nabla \cdot (k\nabla T) + \dot{q} = \rho \cdot c_p \frac{\partial T}{\partial t} \tag{3.3}$$

where $\dot{q}$ is the volume heat generation (W/m^3), ρ is the density (kg/m^3) and c_p is the specific heat (J/kg·K) of the material. At the steady state condition, the temperature distribution is independent to time. Therefore, Equation can be simplified as Equation .

$$\nabla^2 T + \dot{q} = 0 \tag{3.4}$$

Heat convection is more complicated than heat conduction because the fluid mechanics has to be considered. However, a very simple equation can be written down as

$$q'' = h(T_s - T_\infty) \tag{3.5}$$

$$q = \int_{A_s} q'' dA_s \tag{3.6}$$

Here, q'' is the local heat flux and h is the heat transfer coefficient. T_s is the surface temperature and T_∞ is the coolant temperature.

3.2 Spray cooling

As mentioned in the previous chapter, traditional forced convection and micro/macro channel cooling have some inherent problems with the coolant flow rate and system complexity. Therefore, we developed an evaporated spray cooling (ESP)[9] technology that can considerably reduce the required coolant flow rate and pump pressure drop.

Evaporated spray cooling uses a nozzle to spray fine droplets on a surface at a temperature higher than the boiling point of the liquid. The liquid droplets evaporate and absorb heat corresponding to the latent heat of vaporization when striking the hot surface. However, when the droplets wet the hot surface with a layer of water, vapor forms a thin layer of bubbles which isolates the cold water from the hot surface. Under such condition, the heat transfer coefficient will be dramatically lowered. Therefore, one role of the impinging droplets is to break up the bubbles and blow away the water vapor to assure that the hot surface is continuously cooled efficiently.

This technique utilizes the phase change boiling/evaporation transition as the heat transfer mechanism; unlike micro/macro channels or cold-water heat exchangers that are limited by single-phase convection and the specific heat of the coolant. The use of spray cooling allows all the diodes in an array to be cooled in parallel. It is therefore readily scaled to cool any size array. Utilization of spray cooling also makes possible smaller, lighter thermal subsystems because a much lower coolant flow rate is needed. A comparison of the typical coolant flow rates for a 2 cm^2 diode array is given in .[10]
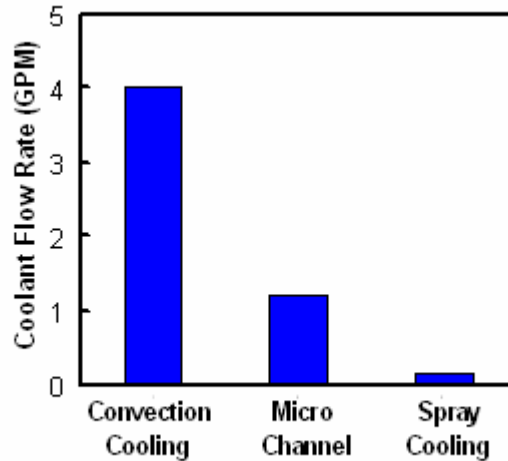
Figure 3.1: Coolant flow rate comparison of different cooling methods

To keep the emitters at a desired temperature, the pressure in the spray cooling chamber can be adjusted or with a wide variety of fluids other than water to be used. The combination of fluid and system pressure will determine the temperature of the diodes. A spray cooling experiment using water at a low chamber pressure was carried out using thick film resistors as the heat source [10]; this proved that spray cooling at low chamber pressure can remove comparable heat fluxes at a low temperature and with similar heat transfer coefficients as can other techniques. represents the system pressure versus water boiling point temperature [11]. This figure shows water boiling point is 100°C at 1 bar, or 1 ATM. shows the experimental results of low pressure water and ammonia evaporated spray cooling. At 1 bar the water ESP can remove heat flux up to 600 W/cm^2. However, the surface temperature is about 40°C higher than the water boiling point at 1 bar which is 100°C. In order to reach a lower surface temperature, a lower system pressure is needed. Since the diode laser performs better at lower temperature, we choose the system

pressure of 0.02 bar which corresponds to water boiling temperature of about 17°C. Other

liquids should be considered if an even lower temperature is preferred.
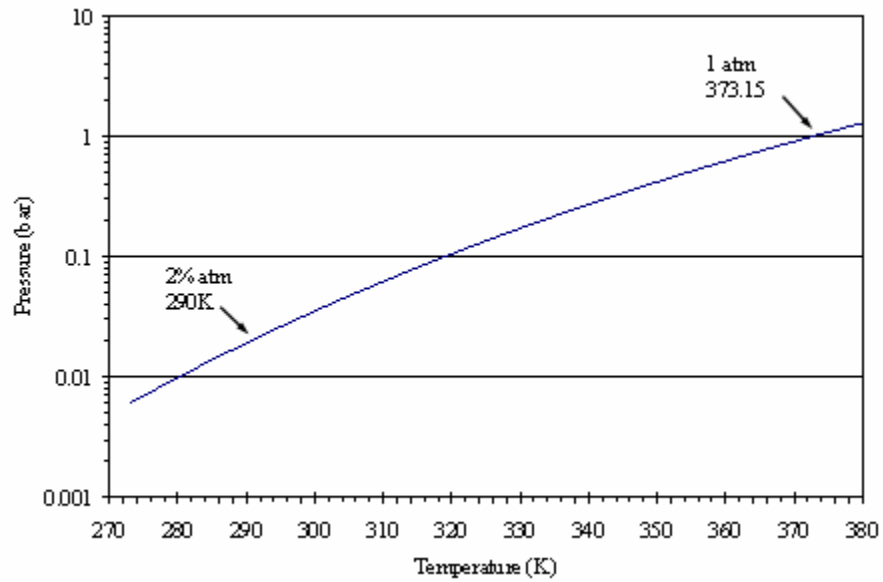
Figure 3.2: The system pressure versus water boiling temperature
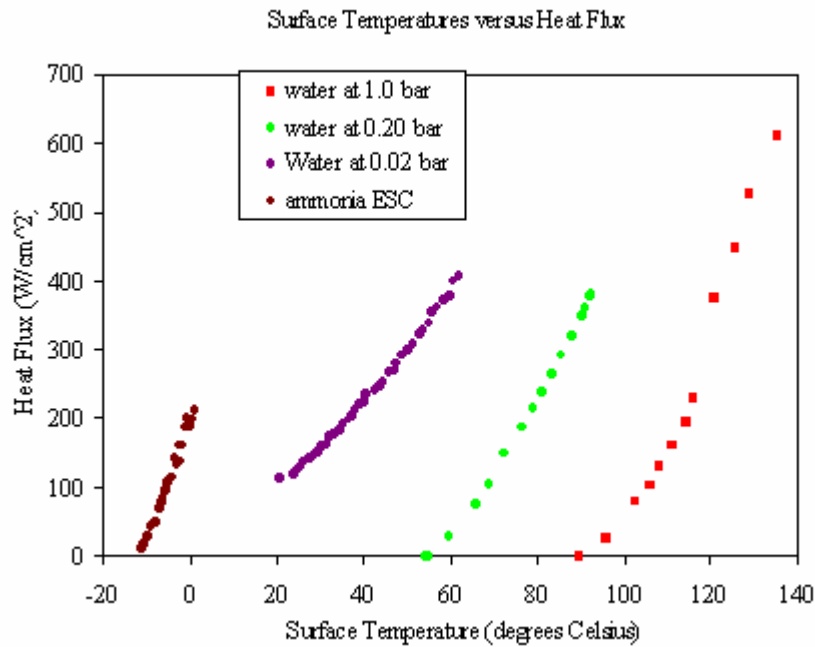
Figure 3.3: Low pressure water and ammonia spray cooling experimental results

3.3 Spray cooled diode laser array

A diode laser array was installed so that it could be cooled by spray cooling with a controlled chamber pressure to set the vaporization temperature of the water coolant. Four Coherent 808 nm B1-40C-19-30-A diode bars (with 19 emitters each) were used for the laser array. The output power of each diode bar is 40 W. The detailed specifications are listed in Table 3.1. The diode bars were packed in a traditional stack package and water was sprayed onto the back copper plate, as shown in . Diode bars were separated by indium coated copper blocks which were 1.1 mm thick. The copper blocks were 1.5 mm deep and their length were the same as the diode bar or 1 cm. A 0.5 mm layer of BeO serves as the common substrate and electrical insulation layer for the array. A 1.2 mm thick copper layer separates the diode array and the spray cooling chamber. Since the

17

system pressure is only 0.02 bar, we designed the chamber to maintain this pressure as shown in .

The spray cooling chamber was made of stainless steel except the top cover plate which was made of copper and the high power diode array module was soldered to it. The spray water had to be boiled to remove any dissolved gas before being put into the chamber. Otherwise, the presence of such gas will prevent the chamber pressure from reaching the desired 0.02 bar. A gear pump forces water through a TG.3/.6 nozzle with a pressure of 48 psi or 33.1 nt/cm^2 to form the spray. Water droplets strike the back of the surface to which the diode laser array is soldered. They evaporate and absorb heat from the surface and hence from the diodes. Eventually, the water vapor condenses on the cooling coil and returns to the reservoir of the spray water to complete the cooling cycle.

Table 3.1 Coherent 808 nm B1-40C-19-30-A diode specification[2]

Coherent 808nm B1-40C-19-30-A diode		Value	Unit
Optical Characteristics	Output power	40	W
	Center wavelength	808	nm
	Center wavelength Tolerance	±2.5	nm
	Wavelength temperature coefficient	0.28	nm/°C
	Spectral Width (FWHM)	<2.5	nm
	Array Length	10	mm
	Number of Emitters	19	
	Emitter Size	150×1	μm
	Emitter Spacing (center-to-center)	500	μm
	Slow Axis Divergence (FWHM) SA	<10°	Degrees
	Fast Axis Divergence (FWHM) FA	<35°	Degrees
	Polarization	TM	
Electrical Characteristics	Slope Efficiency	1.1	W/A
	Conversion Efficiency	>45	%
	Threshold Current	<10	A
	Operating Current	45	A
	Operating Voltage	1.8	V
	Series Resistance	<0.005	Ω
Thermal Characteristics	Thermal Resistance	0.7	°C/W
	Recommended Case Temperature	25	°C
	Operating Temperature Range	15 to 30	°C
	Storage Temperature Range	-40 to 60	°C

---

[2] http://www.coherent-lasergroup.de/laserdioden/download/LaserDiodeBars/3.1_CCP.pdf

Figure 3.6 shows another spray cooling chamber design. It uses two mist cooling nozzles instead of the cooling coil. The mist cooling spray nozzles spray droplets to cool the water vapor. Also, the heat exchanger is moved outside the chamber. Other parts in this chamber are identical to the design in Figure 3.5.

BeO substrate

Copper blocks and diode bars

Copper substrate

1.1

Spray nozzle

Unit: mm

1.2   1.5
   0.5
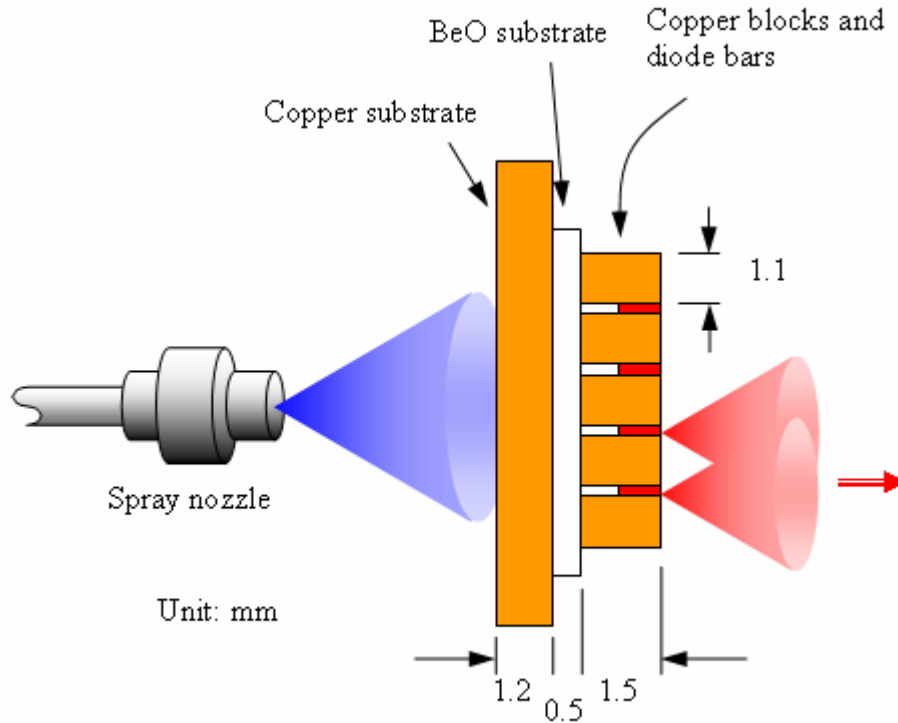
Figure 3.4: The arrangement of the diode array and the spray nozzle
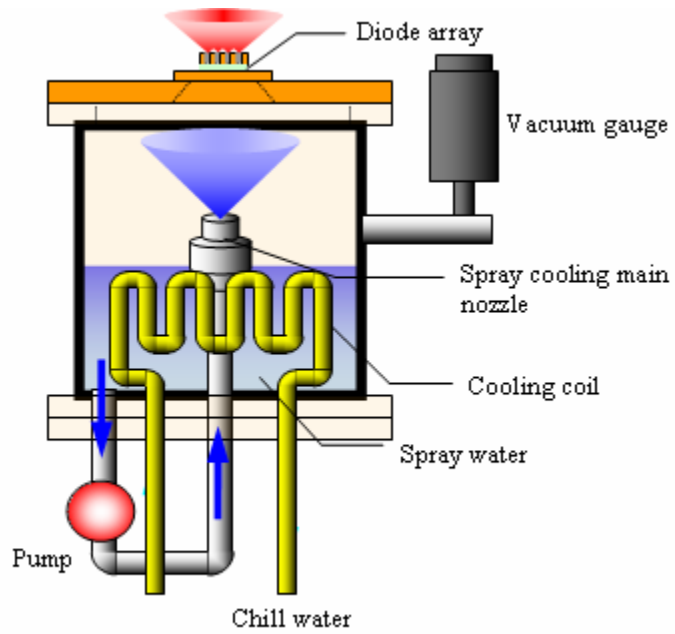
Figure 3.5: The spray cooling experimental set up with the cooling coil design
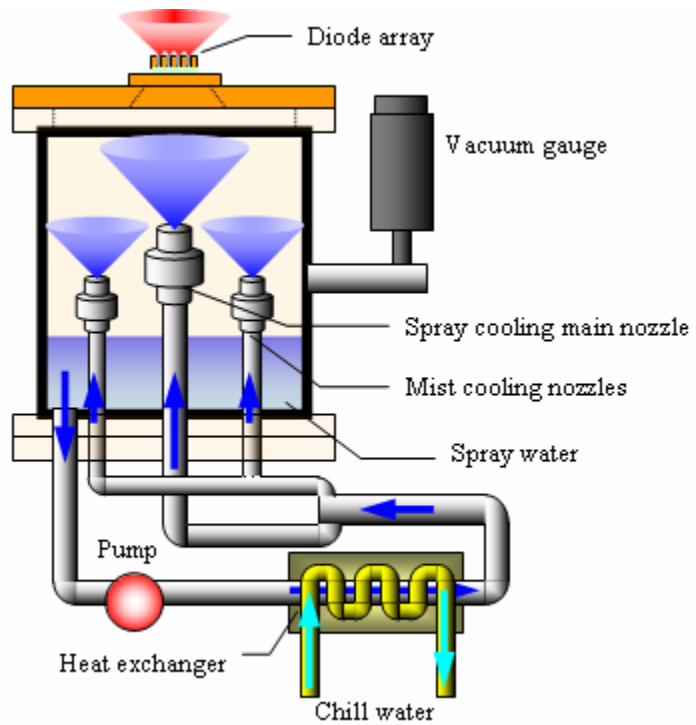
Figure 3.6: The spray cooling experimental set up with the mist cooling design

The power output versus the power input measured for the spray cooled diode array is shown in Figure 3.7. It shows that the efficiency can reach 46% when we increase the current to 45 A. The maximum optical output power was 165 W.

160W Coherent bar, Spray-cooled
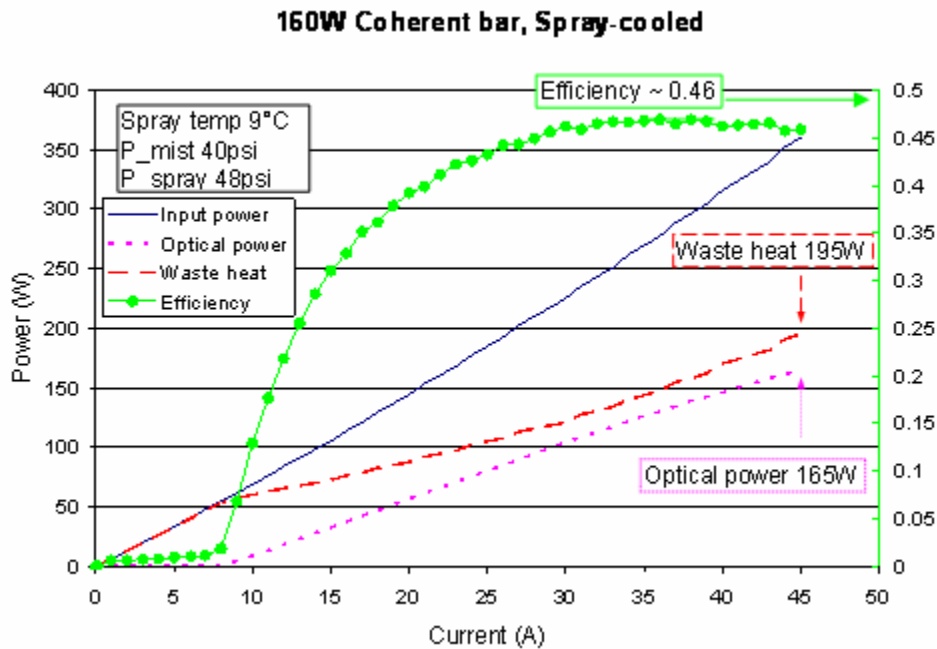
Figure 3.7: Diode laser array input and output power versus current

Using a lens to project an image of the individual emitters we can separately measure the output spectrum of any one. By slightly defocusing the image to make the neighboring emitters' images merge together, we can measure the average spectrum of several emitters at the same time. An Ocean Optics HR2000 spectrometer with high resolution centered at 800 nm was used to measure the output spectrum of several emitters at the right and left sides of the diode array. The results are shown in Figure 3.8.

22

The center output wavelength is about 812.3 nm and the FWHM is less than 2 nm when the array is running at full power.

The wavelength temperature coefficient of the diode laser is given as 0.28 nm/°C in Table 3.1. The temperature versus wavelength chart is shown as Figure 3.9. We also measured the output wavelength of each emitter. In this figure, we list the longest and shortest wavelengths of the emitters when the total current is 8.5, 30 and 45 A. We can easily find the corresponding temperature of the emitters. The diode emitters are labeled from 1 to 19. The coding in is based on the position of the emitter location. For example, 30A10_4 indicates this emitter is at the 4th bar and it's the number 10 emitter on this bar when the driving current is 30 A. Since the diode bars have only 19 emitters, the 10th emitter is at the center of the bar. Also, because we have four bars in this array, 2nd and 3rd bars are in the middle of the array. Edge effects reduce the emitter temperature of the emitters on the outer edges of the array; consequently, we can expect emitter 10_2 and 10_3 to have higher temperatures as compared with 01_1 or 19_4. We observe that the 2nd bar has higher temperature than bars 1 or 4. When the driving current is higher, the temperature distribution range becomes significantly larger. The experimental data show this trend, but the data is not symmetrical, most likely due to solder layer non-uniformity.
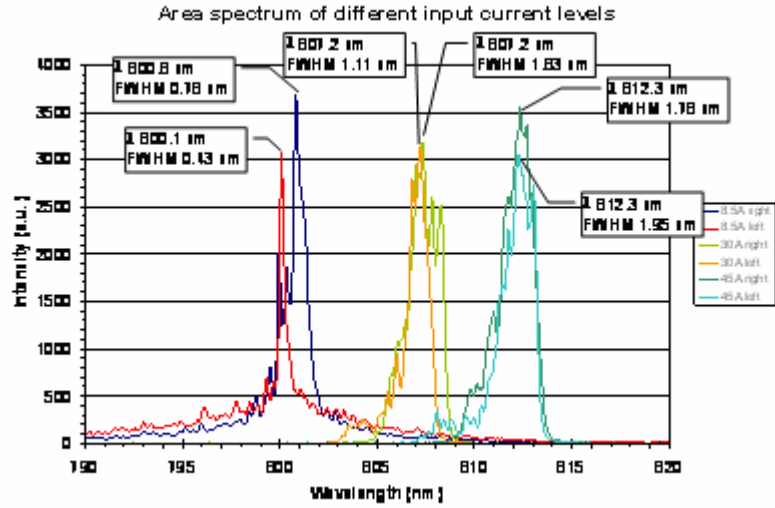
Figure 3.8: Average spectrum at different input current levels
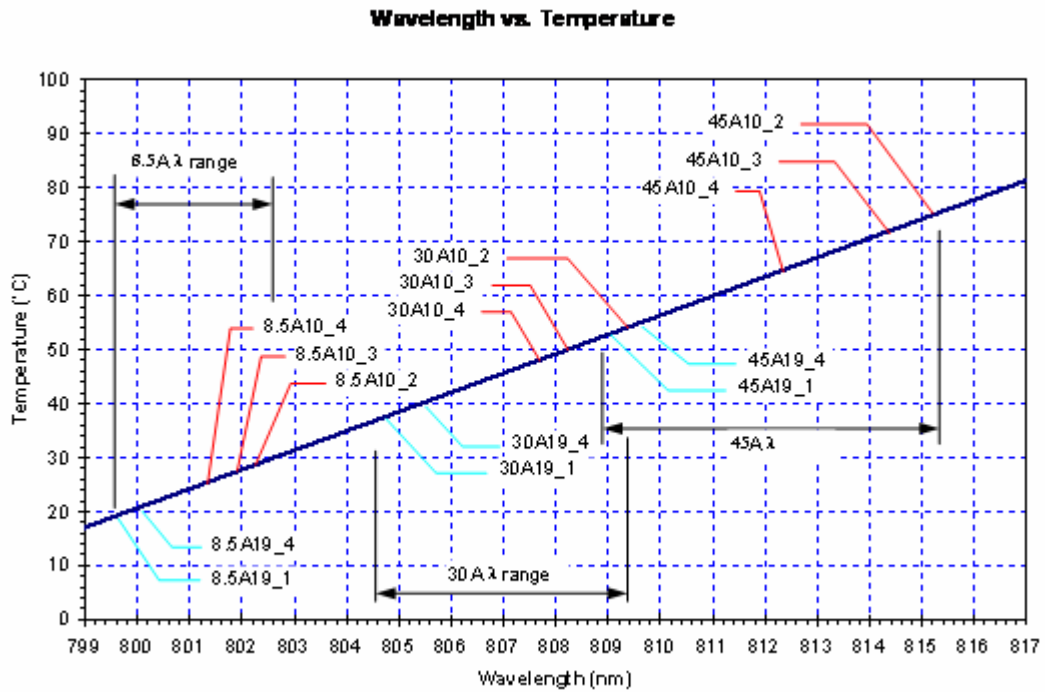
Figure 3.9: Wavelength and temperature of different emitters at different driving currents

24

The wavelength spread at full power is about 6.3 nm. This implies a temperature difference of about 20° C from place to place in the array. Further the central wavelength is higher than desired indicating that the average emitter temperatures are still too high. Not only does the high temperature and large gradient make the diode emitting wavelength mismatch the Nd:YAG peak absorption wavelength reducing the utility of the array for pumping this medium, it also reduces the emitter operating lifetime and efficiency. Consequently, further packaging improvements are necessary to reduce thermal resistance, lower operating temperature and increase uniformity.

3.4 Spray cooled stack packaging results and analysis

By putting the HR2000 fiber probe far away from the diode laser array, it can measure the average output wavelength of the whole array and this measurement at full power gives an average emitter temperature of 62°C. Figure 3.10 shows the relation between estimated average emitter temperature and the waste heat flux at different operating power levels. The total thermal resistance is about $0.082°\text{C}\cdot\text{cm}^2/\text{W}$ based on the bar area (0.65 mm by 1 cm). This includes the thermal resistance for conduction from the emitter to the back plate and the thermal resistance for spray cooling. In order to determine the thermal resistance of this package, the heat conduction at full laser power operation was simulated with finite element methods using the commercially available code called Femlab®. Figure 3.11 gives the computed temperature distribution. In the simulation, a coolant temperature of 10°C was assumed with a heat transfer coefficient of $180,000 \text{ W/m}^2\cdot\text{K}$. It can be seen that simulation results are consistent with data from the optical measurements in which also gives the temperature of the sprayed surface at

25

different power levels. The temperature difference between the emitter and the back plate is about 27°C resulting in a thermal resistance for conduction in this package of about 0.047°C·cm^2/W. These results demonstrate that it is very important to reduce the conduction resistance between the emitters and the back surface by reducing the thickness of the diode substrate and the copper plate (see Figure 3.4). If the distance were changed from the value in present package (2.7 mm) to 1.5 mm, the temperature difference between the emitter and the back plate could be reduced to 16°C. The thermal resistance for conduction becomes 0.021°C·cm^2/W if the total thickness of the copper is 1.5 mm which includes the thickness of back plate and diode spacers. In such a case, the temperature of the emitter is estimated to be about 51°C which corresponds to operation at 808 nm, or very near the peak absorption wavelength for Nd:YAG. However, a thin structure like this might not have enough mechanical stiffness to sustain the pressure difference of the spray cooling chamber.

Figure 3.10 Heat flux versus average diode temperature

Heat flux 2 W/(150 μm x 1 mm)
Heat trans. Coeff = 1.8 x 10^5 W/m^2·K
$T_0 = 10°C$

62.1°C ×1e-3

49.0°C

Max: 62.1

Min: 30.093

1.5 mm spacer Cu + 0.5 mm BeO

1.5 mm Cu spacer + 0.5 mm BeO
+ 1.2 mm Cu substrate
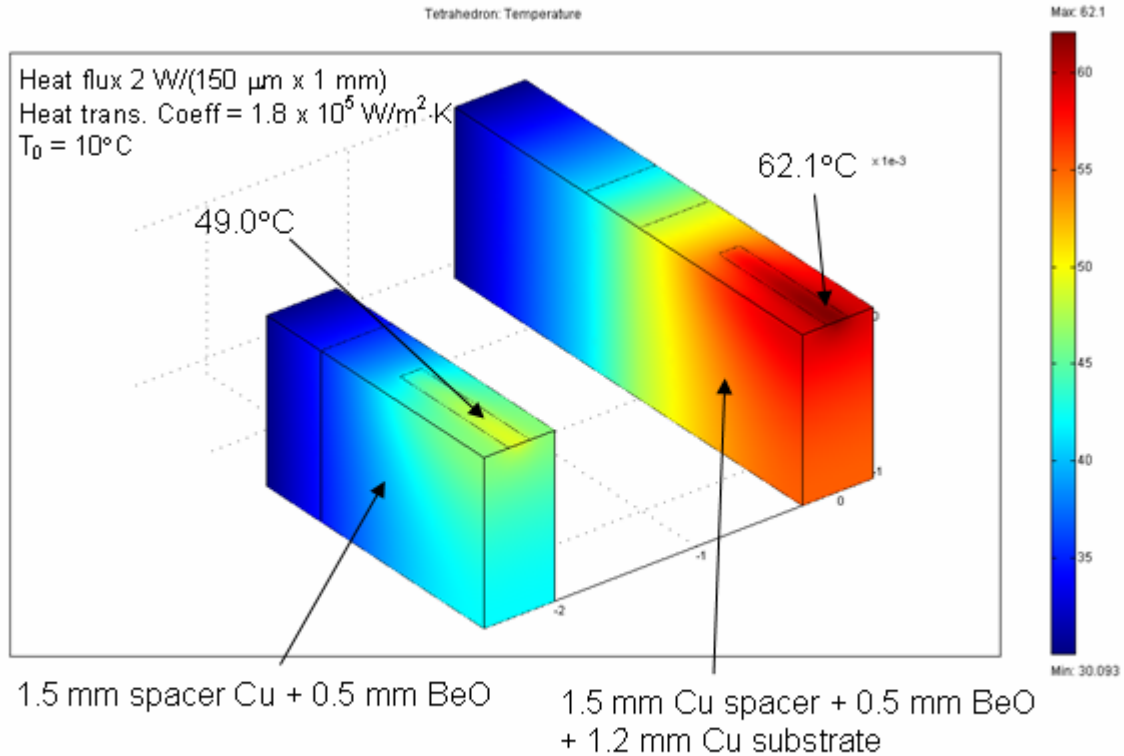
Figure 3.11: FEA result of temperature distribution of diode array stack with 2.7 mm and 1.5 mm thick copper spacers

3.5 Summary of spray cooling experiment

We demonstrated the capability of low pressure water spray cooling to handle a typical diode laser array with heat flux of about 400 W/cm^2. The individual emitter spectra we measured enabled us to estimate the emitter temperatures by using the known temperature coefficient of the diode laser wavelength. The result shows the emitter temperatures are quite high for the array tested. There are three main ways to reduce the diode temperature. One is to improve the cooling technique by using another liquid, for example Ammonia or R134a, for spray cooling. The second is to improve the nozzle design and optimize the droplet velocity and size to achieve an even higher heat transfer

coefficient and the third is to develop a new packaging design which shortens the cooling

path and/or uses materials with higher thermal conductivity.

4. BEAM CONTROL PRISM (BCP) DESIGNS

4.1 Prior work

Several designs have been proposed to manipulate the diode laser output beam direction and/or the beam shape. The simplest one is a plane mirror which redirects the beam [12]. The mirror can be integrated with the diode laser with the substrate [13,14]. An improved design employs a parabolic reflective surface to re-directed and collimate the output beam [15]. However, these designs can't provide angular tuning. Also, these designs are usually having poor thermal properties because the active region is far from the coolant. Other practical issues such as the packing spacing and the manufacture feasibility have not been considered thoroughly.

4.2 Basic BCP concepts

Conceptually, a BCP is a folded lens. It combines a mirror and a lens into one optical element. The mirror redirects the beam direction and the lens controls the beam spread or the beam divergence. Figure 4.1 shows different designs of BCPs. They are curved-reflective, curved-entrance, curved-exit, folded-ball and refractive BCPs. Each design has different optical properties.
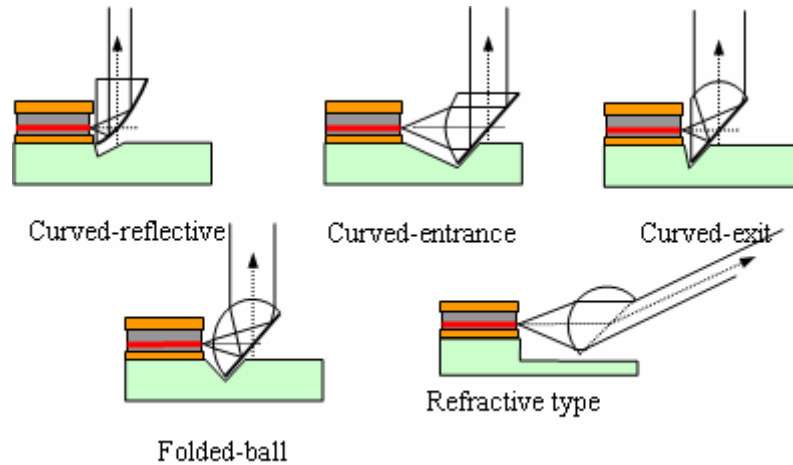
Figure 4.1: Different types of BCP

A diode laser, in general, has divergence angle of 35° FWHM (or 60° at full angle). In other words, its numerical aperture (NA) is about 0.5 at full angle. Various aberrations will be a very large for a spherical surface optic with such small NA. Consequently, it is necessary to consider an aspheric optic and/or some other approach to eliminate aberrations[16].

Since BCPs are essentially folded lenses, the curved surfaces need to be conic surfaces to achieve the stigmatic condition. Figure 4.2 shows the ideal conic surfaces to achieve the stigmatic condition for different lenses or BCP designs. A curved-exit surface BCP demands an elliptical surface. A curved-entrance surface BCP requires a hyperbolic surface, and a parabolic surface is needed for a curved-reflecting surface BCP. However, these conic surfaces are not easy to make. The most readily employed surface is still circular which requires that we use a ray tracing program such as ASAP to simulate the optical properties of BCPs by using geometric and wave optics approaches to show how the idea might work.

31
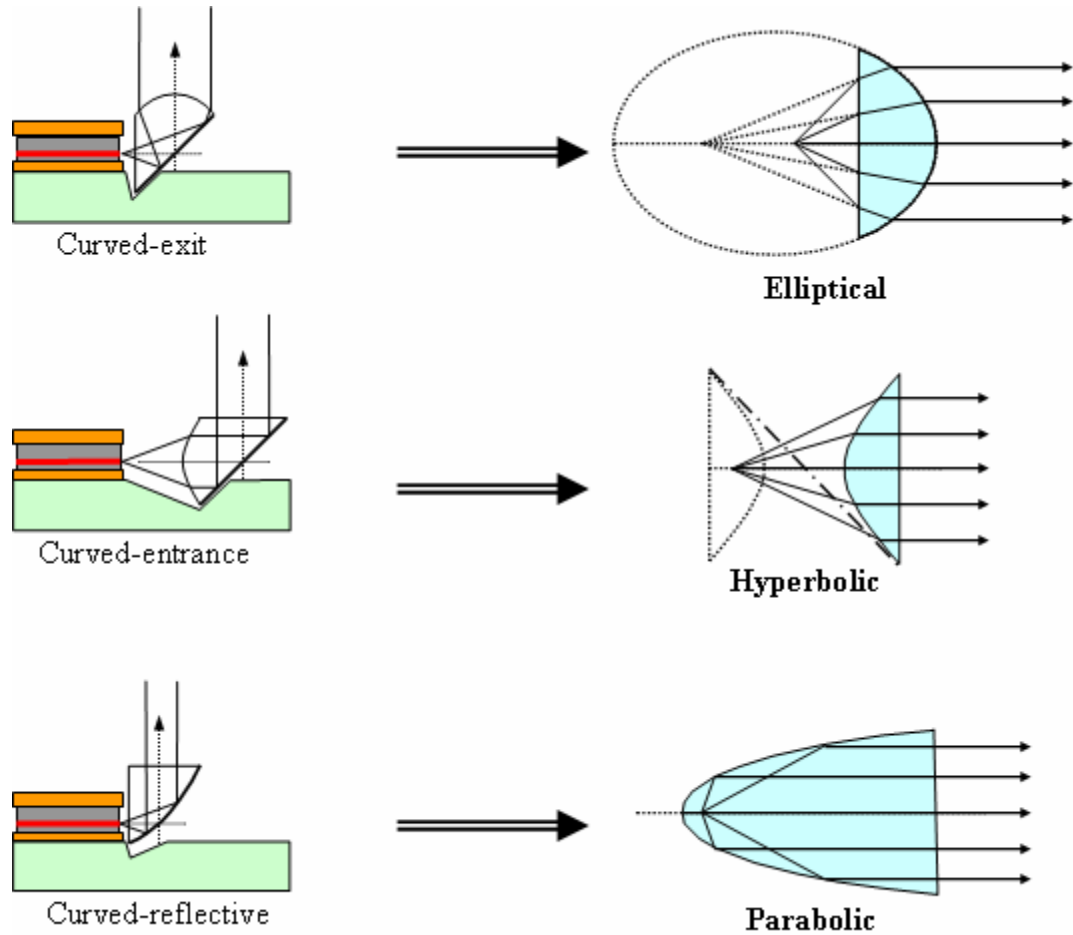
Figure 4.2: Ideal conic surfaces for stigmatic BCP designs

The geometric ray tracing gives a simplified approach to understand BCPs. Taking the folded-ball BCP case as an example, we need to consider the power loss due to the long focal length as shown in Figure 4.3. When the tilting angle of a BCP is selected, the beam angle and the optics axis are decided as well. In the folded-ball case, the beam angle is twice of the BCP tilting angle. Once the material of the BCP is determined, the focal length of the BCP is fixed. Use of low index of refraction material makes the focal length longer. In other words, the BCP will have larger NA and there will be power losses. Use of BCPs to control diode laser light can offer a higher packing density than

using the technique in Ref. [14,15] and the capability of angular tuning the output beam.

Also, the manufacture demand is relatively lower.

Most optical lenses are still made with spherical surfaces, which reduce the cost and complexity, yet the trade off is the optical performance as mentioned above. Because BCPs are mainly operated on axis, the most severe aberration is the spherical aberration (SA). The two most practical types of BCP are the curved-exit and folded-ball BCP because of their properties and ease of manufacture. It is well known that the plano-convex lens has low spherical aberration. This corresponds to the curved-exit BCP. The folded-ball BCP is a very simple design. Moreover, its corresponding lens, the ball lens, is widely used for large beam divergence or large NA system such as coupling a diode laser output into an optical fiber. These two cases are the most feasible designs for mass production and applications that do not demand high optical performance.

4.3 Analysis of the folded-ball and curved-exit designs

4.3.1 Acceptance angle analysis

As defined in Figure 4.3, the acceptance angle is another representation of NA. The incident rays with their angles larger than the acceptance angle are not directed into the beam angle direction. By using ASAP geometric ray tracing, we can determine the relations between the acceptance angle, the tilt angle and the index of refraction of the material. These can also be calculated by using simple geometrical analyses (Appendix

A). In the folded-ball case, there are two charts for this analysis because the acceptance angles are different on the positive side and the negative side of the optical axis. We define the positive side as the upper acceptance angle and the negative side as the lower acceptance angle. The aperture limit is the angle that the ray has 90° incident angle.
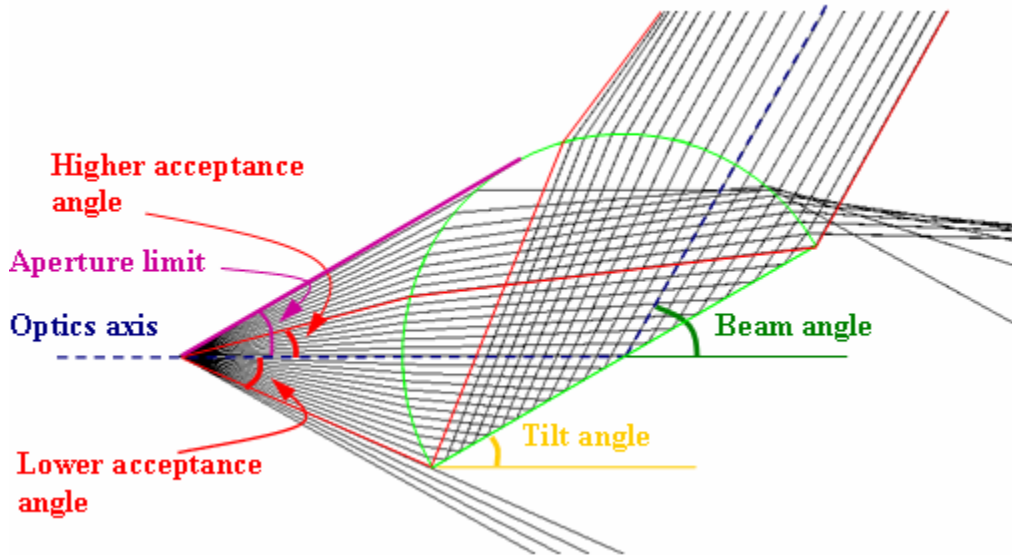
Figure 4.3: The folded-ball BCP parameters

Figure 4.4 shows the upper acceptance angle versus the index of refraction of the material at different beam angles. This chart shows that folded ball BCPs prefer to be operated at higher beam angles. A 90° or higher beam angle operation gives a lower power loss. Figure 4.5 shows that the lower acceptance angle is not as critical as the upper acceptance angle as long as the beam angle is larger than 50°.
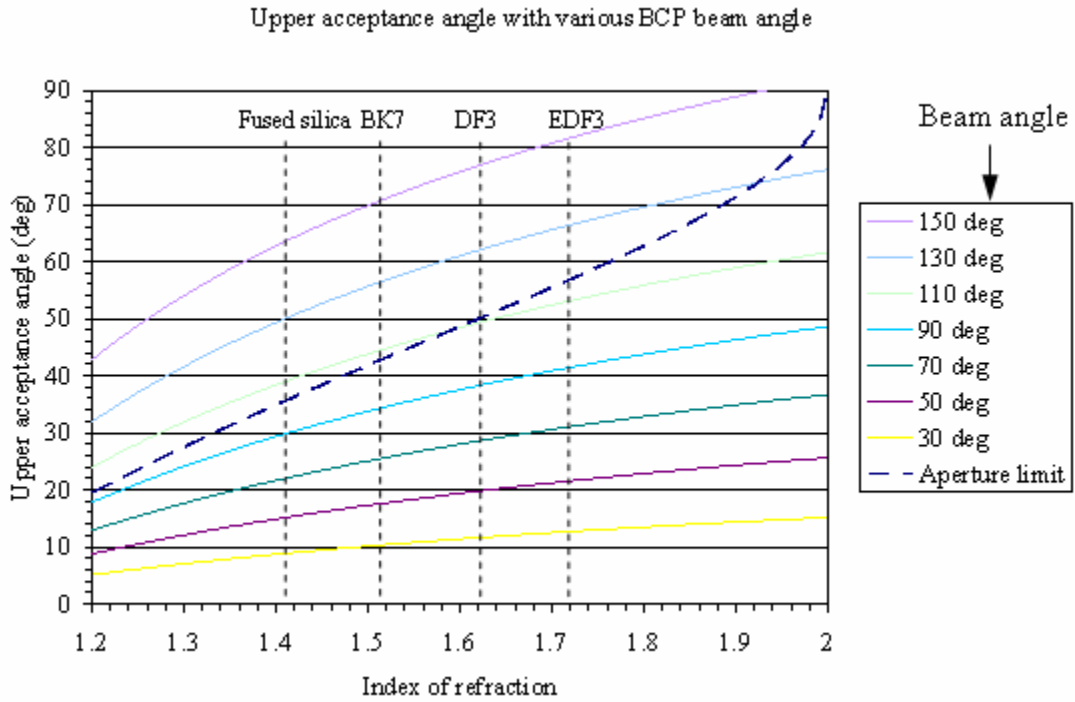
Figure 4.4: The upper acceptance angle versus the index of refraction of BCP at different beam angles

Figure 4.6 shows the energy fraction outside a Gaussian distribution e^{-x^2} with respect to the position x. When x is equal to 0.83, it is the position corresponding to the full width half maximum (FWHM) of the Gaussian function. We consider a symmetric aperture case. If 95% of the output power needs to be delivered to the beam angle of the BCP, the BCP has to extend to x values of at least 1.38 on both sides of the Gaussian beam axis. In other words, the BCP will have both acceptance angles larger than 27.7°. Similarly, if both acceptance angles are 31.9°, this indicates that x = 1.64 and the delivered power will be 98%. In treating an actual BCP it will be necessary to include the surfaces' Fresnel reflectivity.

A reasonably good BCP design will deliver more than 95% of the power from diode emitter to the beam angle direction. If the BCP is made of BK7 glass with n=1.51, from Figure 4.4 we know the upper acceptance angle is larger than 30° when the beam angle is larger than 80°. Also the lower acceptance angle is larger than 30° when the beam angle is larger than 30°. This implies that a folded-ball BK7 BCP has the angular tuning range from 80° to 180°.
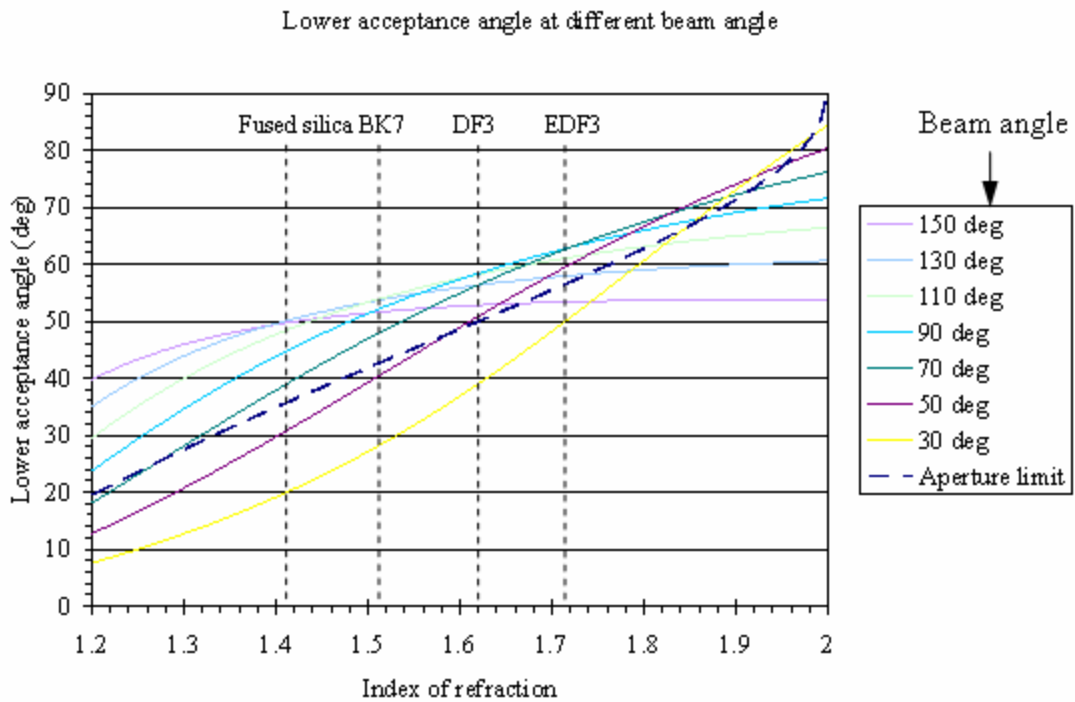
Figure 4.5: The lower acceptance angle versus the index of refraction of BCP at different beam angles
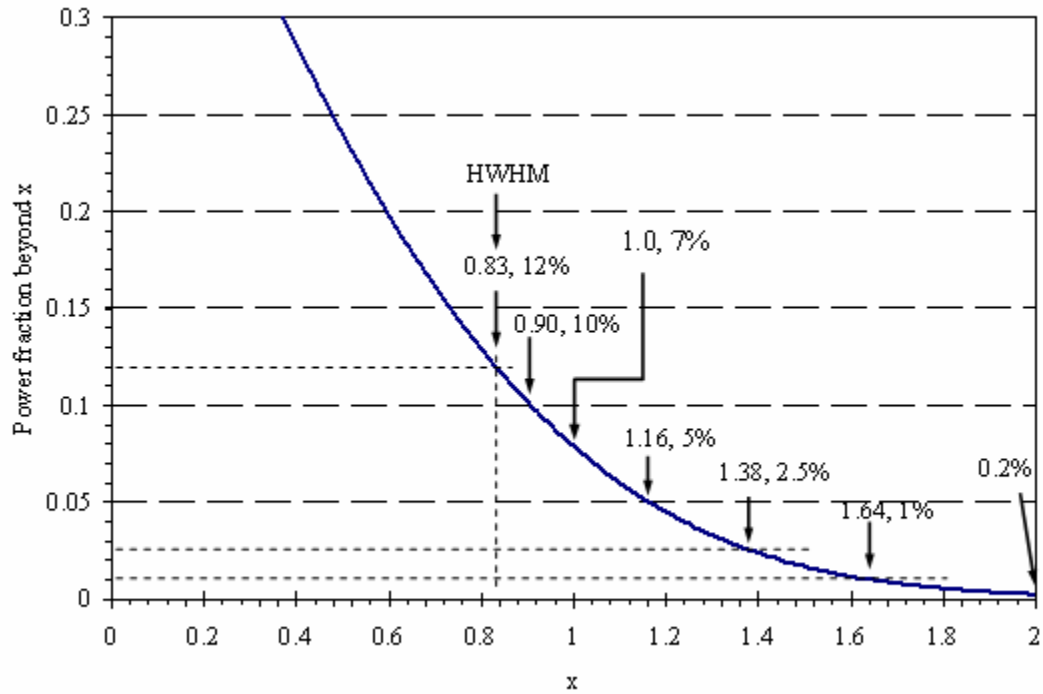
Figure 4.6: The integration of the Gaussian function

A similar analysis of the curved-exit design was also performed. As mentioned, the curved-exit design has much less spherical aberration. However, the optical power of this type of BCP is smaller compared with the folded-ball design. Consequently, the focal length is longer and the acceptance angles are smaller than for the folded-ball BCP. Figure 4.7 shows the parameters of the curved-exit BCP design which shows the wide and the narrow acceptance angles. They are symmetrical to the 90° beam angle. In other words, 70° and 110° beam angle have the same wide and narrow acceptance angles, but they correspond to different parts of the incident beam. For a beam angle less than 90°, the upper half of the incident beam is limited by the narrow acceptance angle as shown in

37

Figure 4.7. If the beam angle is larger than 90°, the upper half of the incident beam will be limited by the wide acceptance angle.
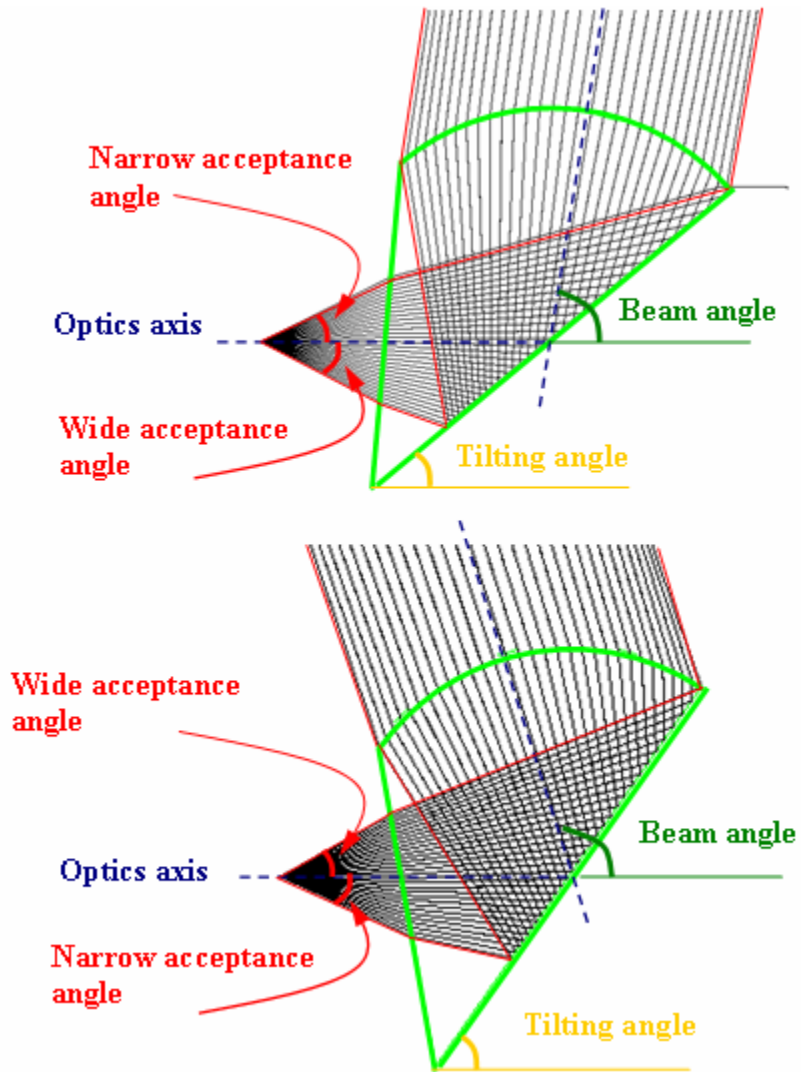
Figure 4.7: The curved-exit BCP parameters

Figure 4.8 is a plot of the narrow acceptance angle versus the index of refraction of the material. The wide acceptance angle versus the index of refraction of material is shown in Figure 4.9. Since only one surface has optical power, the acceptance angles are

smaller than in the folded-ball case. Therefore, higher index of refraction materials are preferred. This result also implies that the curved-exit design has poor angular turning capability.
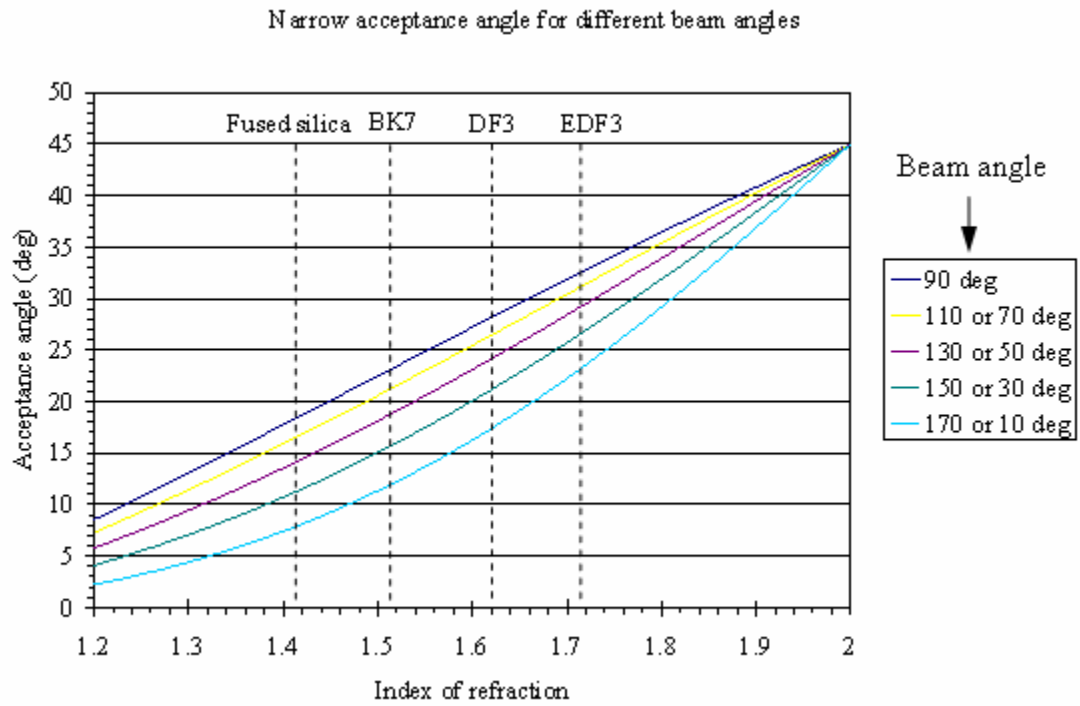
Figure 4.8: The narrow acceptance angle versus the BCP index of refraction at different beam angles
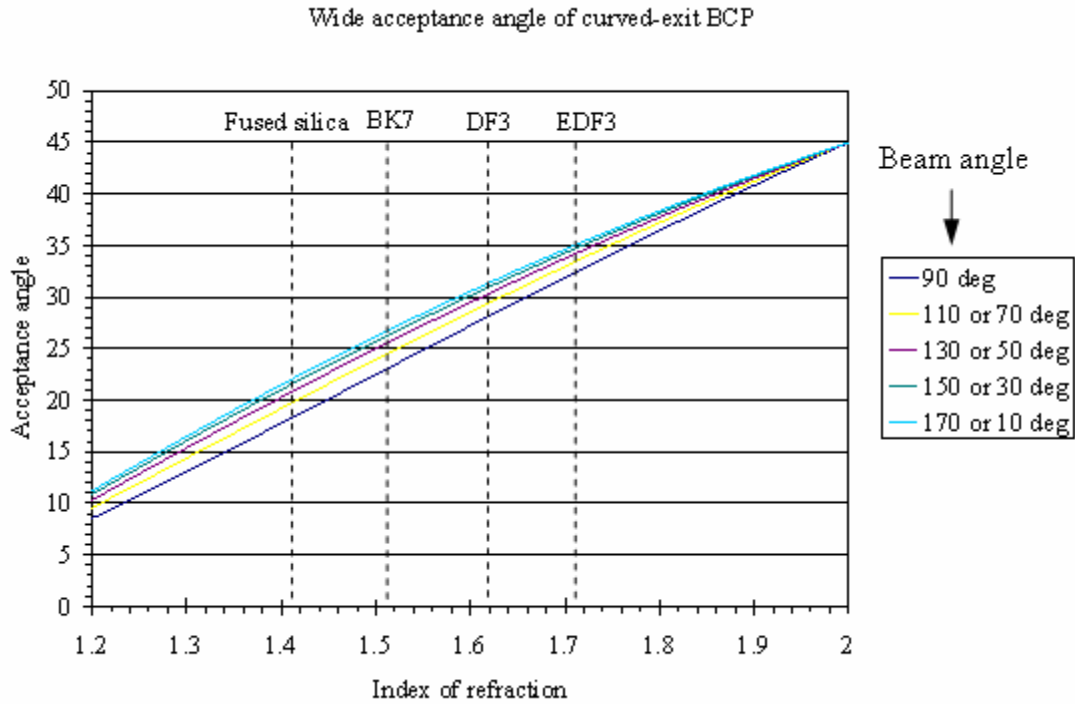
Figure 4.9: The wide acceptance angle versus the BCP index of refraction at different beam angles

For 90° beam angle operation a curved-exit BCP has to have the index of refraction higher than 1.71 to deliver 98% of the incident laser power. Also, the focal point is not the same when changing the beam angle. These two properties make curved-exit BCP design not suitable for angular tuning applications. However, its spherical aberration is much lower than that of a folded-ball BCP.

4.3.2 Aberration analysis

If the diode emitter is on axis, spherical aberration only needs to be considered. A series of calculations was performed using Code V to evaluate the aberration. The image distance is set as 50 mm and the BK7 glass BCP radii are set to be 0.5 mm for different

cases. Because Code V is a sequential ray tracing program, BCPs are unfolded as thick lenses. Their aperture sizes are all 0.7072 mm as shown in Figure 4.10. The half acceptance angle obtained here is equivalent to the upper acceptance angle of the folded-ball case when the beam angle is 90°. For the curved-exit case, the half acceptance angle described here is equal to both acceptance angles at the 90° beam angle discussed in the previous section.

Figure 4.11 shows four ray aberration plots at four different points of interest. If the object distance is smaller than the position corresponding to Fig. 4.11 (a), none of any two rays from the exit pupil is projected to the same point in the image plane. In other words, no interference can be observed. The marginal focal point has the ray aberration plot shown in Fig. 4.11(b). Every point of the image receives contributions from two rays from the exit pupil except the point on axis which is the combination of the marginal rays and the chief ray. Minimum spot size is achieved when each point of the image is formed by three rays from the exit pupil except the outmost points as shown in Fig. 4.11 (c). The paraxial focal point ray aberration plot is in Fig. 4.11 (d). If the object distance is even larger, each point of the image again corresponds to a single ray from the exit pupil. In other words, there is no interference for larger object distances.
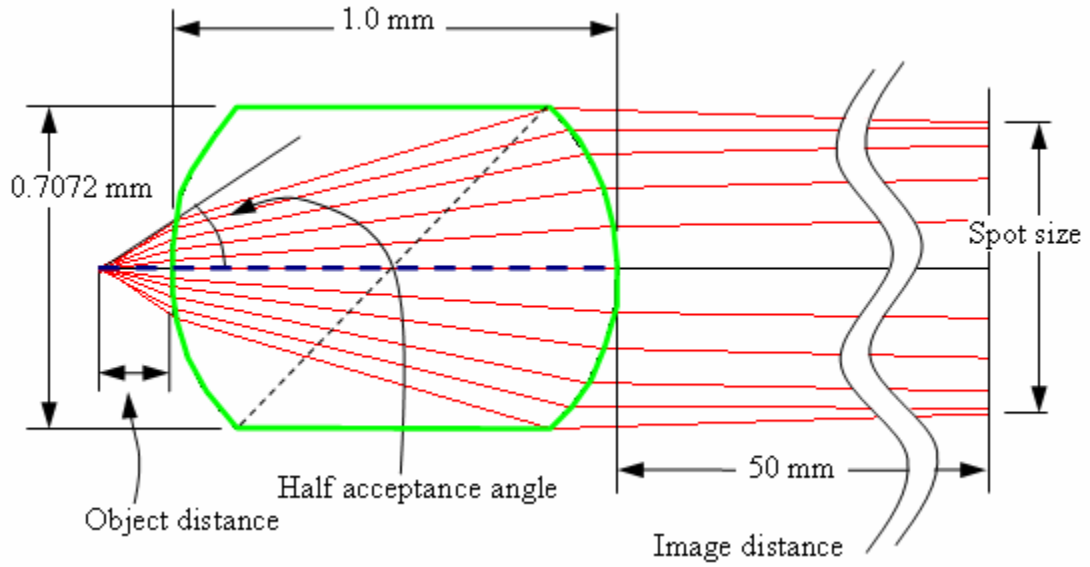
Figure 4.10: Parameter definitions for Code V aberration analysis
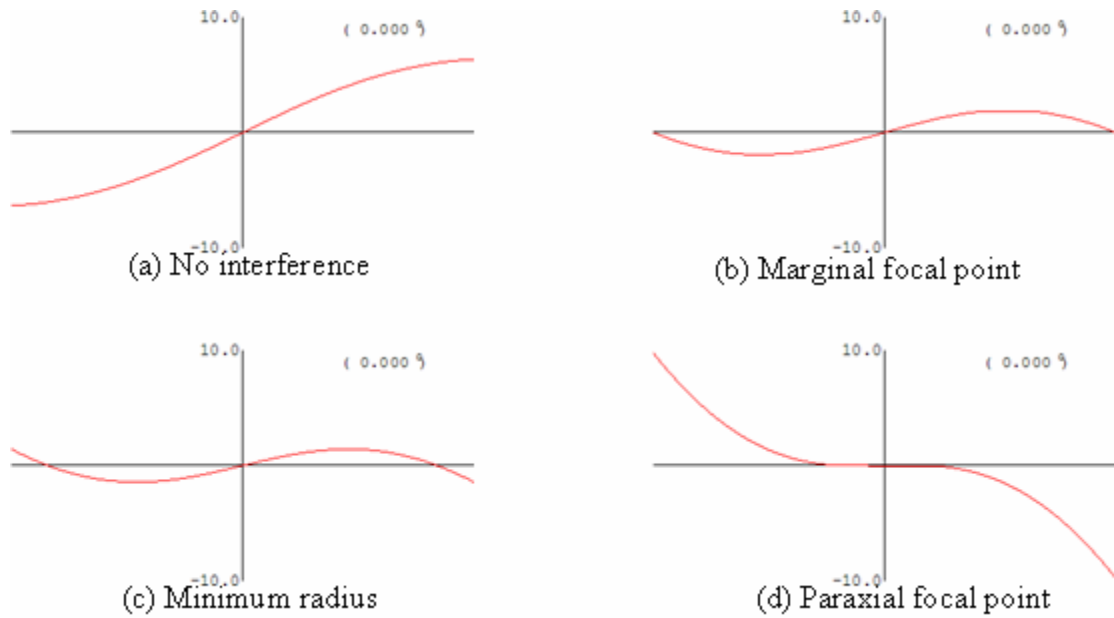
Figure 4.11: Four ray aberration plots at the points of interest

Figure 4.12, Figure 4.13 and Figure 4.14 show the spot sizes and half acceptance angles versus the object positions for folded-ball, curved-exit and curved-entrance BCPs.
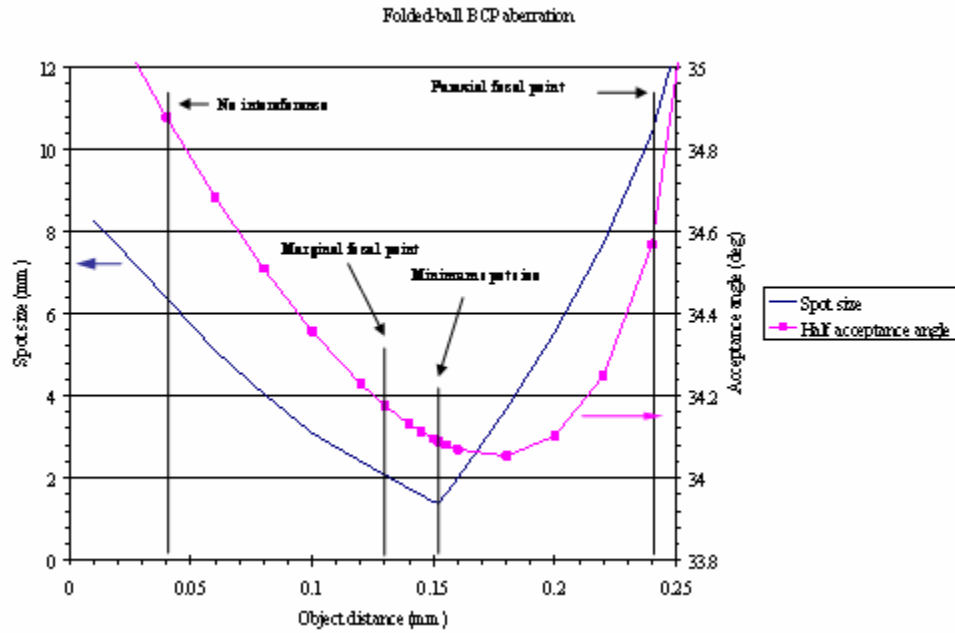
Figure 4.12: The folded-ball BCP aberration analysis
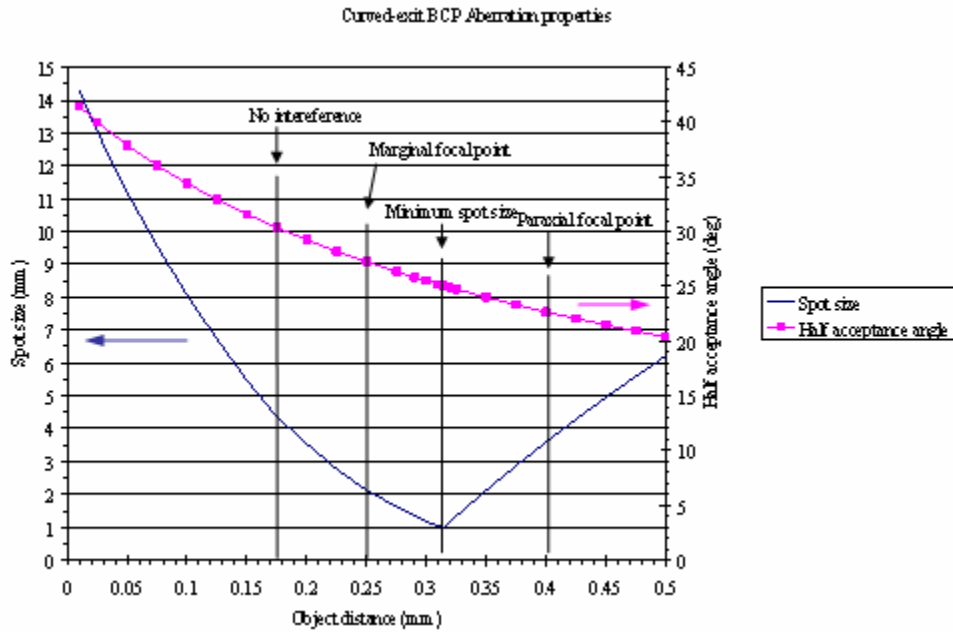
Figure 4.13: The curved-exit BCP aberration analysis
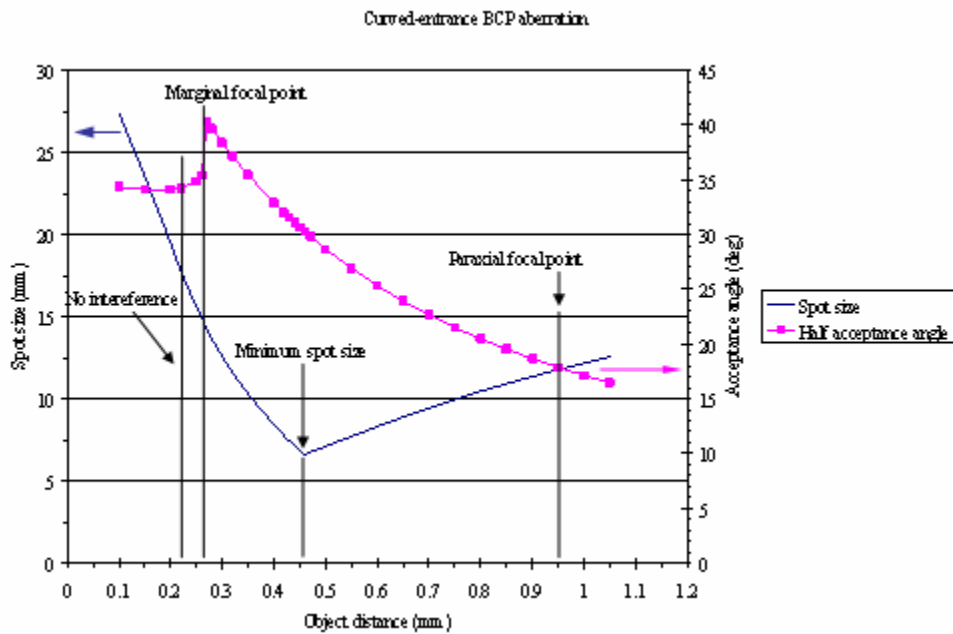
Figure 4.14: The curved-entrance BCP aberration analysis

44

These three figures can be plotted together if the minimum spot size positions are set as zero as shown in Figure 4.15. Also, only the regions with interference pattern are plotted. The folded-ball half acceptance angle is always larger than 34°. However, the curved-exit BCP can only achieve half acceptance angle of 25° at the minimum spot size point. The folded-ball BCP has a slightly larger minimum spot size compared with the curved-exit BCP. However, because of the stronger optical power of the folded-ball BCP, its spot size curve shows steeper slopes which imply the folded-ball BCP is most sensitive to the object position.

The curved-entrance case shows a much stronger aberration and a much larger interference range comparing with the other two designs. This is a direct proof that a circular surface curved-entrance BCP is not a practical design. The spike of the half acceptance angle of the curved-entrance BCP comes from the aperture stop. If the object is close to the BCP, the exit pupil is the aperture stop. On the contrary, if the object is far from the BCP, the entrance pupil is the aperture stop. In the curved-entrance case, the spike position is exactly the marginal focal point position. A similar half acceptance angle spike takes place in the folded-ball BCP for the same reason, but the location of its spike is not in the interference range.

Spherical aberration is inevitable if the BCP is using a spherical (for cylindrical optics such as BCPs this means circular) surface and will cause interference fringes in the image plane. There are not many choices available to the BCP designer to reduce or avoid the interference fringes. Making the object position smaller than the no interference point or larger than the paraxial focal point can avoid the interference fringes

but the trade off is a much larger beam divergence angle. The paraxial focal point gives a strong center lobe but a considerable amount of energy will appear outside the central region.
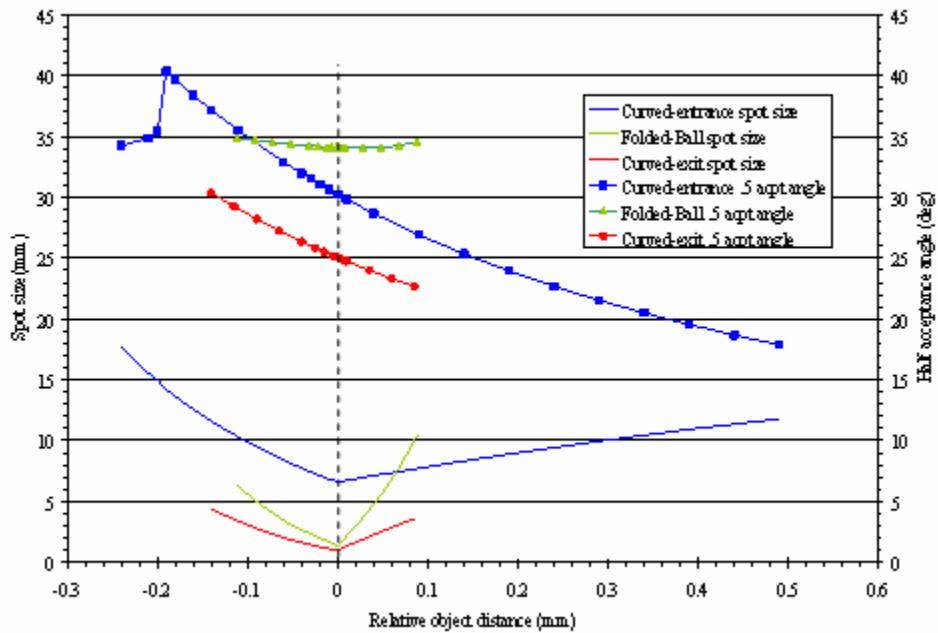
Figure 4.15: Comparison of three BCP designs performance

4.3.3 Tolerance analysis

A smaller BCP requires more precise translation and rotational positioning. Figure 4.16 shows the 5 degrees of freedom that will influence the output beam.
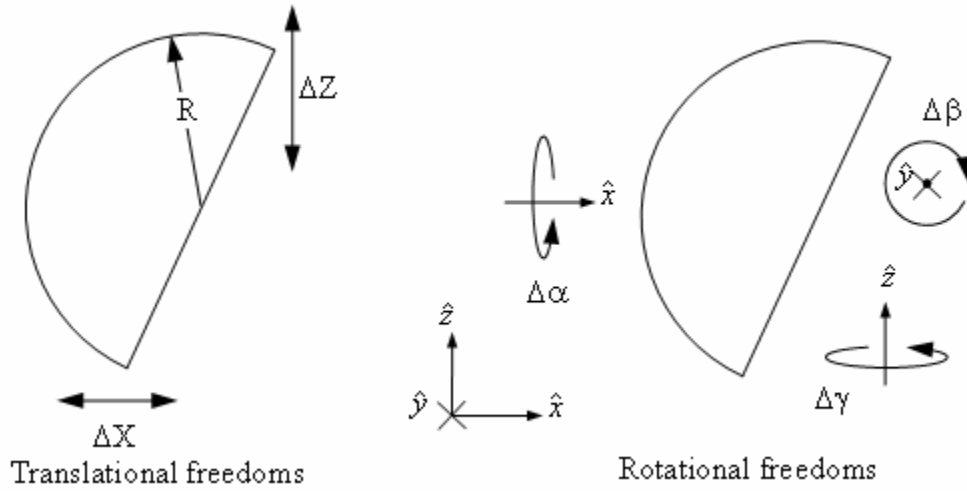
Figure 4.16: Five degrees of freedom that influence the output beam

$\Delta\alpha$ is limited by the ΔZ translational position tolerance, and $\Delta\gamma$ is limited by the ΔX translational position tolerance. We obtain the small beam angle change with respect to ΔX and ΔZ as:

$$\Delta\Theta_{defocus} = \frac{(n-1)\cdot\tan\phi}{n} \cdot \frac{\Delta X}{R} \tag{4.1}$$

$$\Delta\Theta_{angular} = \frac{n\cdot(n-1)}{(n-1)^2 + 1} \cdot \frac{\Delta Z}{R} \tag{4.2}$$

From Equation (4.1) and (4.2), the radius of curvature, R, or the BCP dimension is inversely proportional to the position tolerance. In other words, a larger BCP has better positioning tolerance and is easier to align. ϕ is the acceptance angle which can be obtained from Figure 4.4 and Figure 4.5. For the angular positioning precision, it is trivial to show that

$$\Delta\Theta_{angular} = 2\cdot\Delta\beta \tag{4.3}$$

Let the BCP length along the y direction be L so that

47

$$\Delta X = \Delta \gamma \cdot L \tag{4.4}$$

$$\Delta Z = \Delta \alpha \cdot L \tag{4.5}$$

These two equations give the angular tolerance for aligning the BCP.

We also used the wave optics approach of ASAP to evaluate BCPs. This procedure gives the diffraction patterns and the flux distribution for the considered BCP. We analyzed the folded-ball, the curved-exit and the curved-entrance cases and found that the folded-ball BCP is the most efficient design, however the curved-exit surface design gives minimum spherical aberration. All three designs can focus a diode laser output beam very tightly. The beam size can be reduced to 0.23° or 4.2 mrad. Figure 4.17 shows the simulation results for different BCP designs. The number on top of each chart indicates the relative peak intensity of each case.
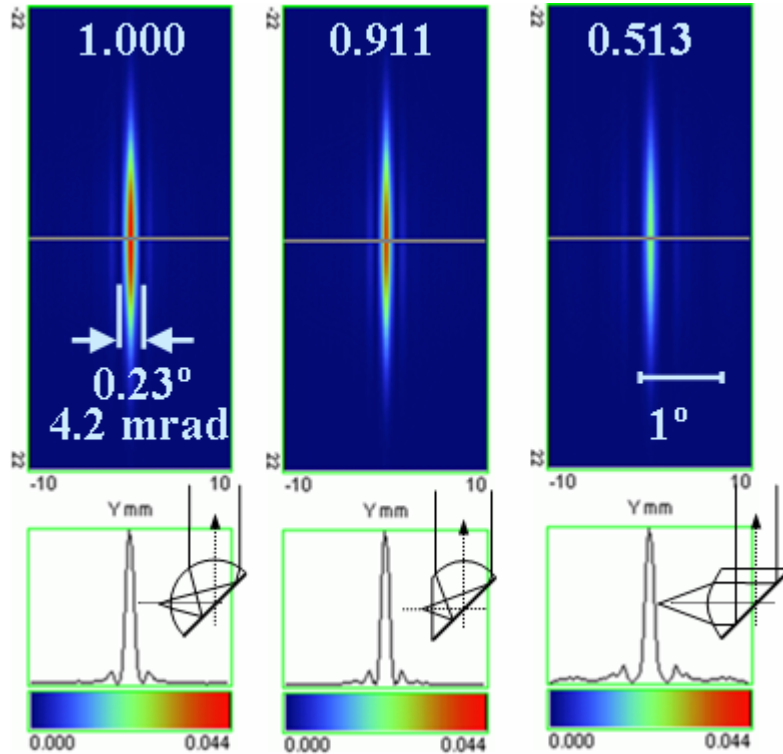
Figure 4.17: ASAP wave optics simulation

4.4 Experiment results of different BCPs

The experimental setup of the BCPs test is shown in Figure 4.18 where the spray cooled diode laser array mentioned in the previous chapter was used. The BCP was held in front of one of the diode bars by XYZ stages and rotational stages to ensure all six degree of freedoms of the BCP could be adjusted. A CCD camera was placed 5 cm from the BCP to monitor the output beam shape.
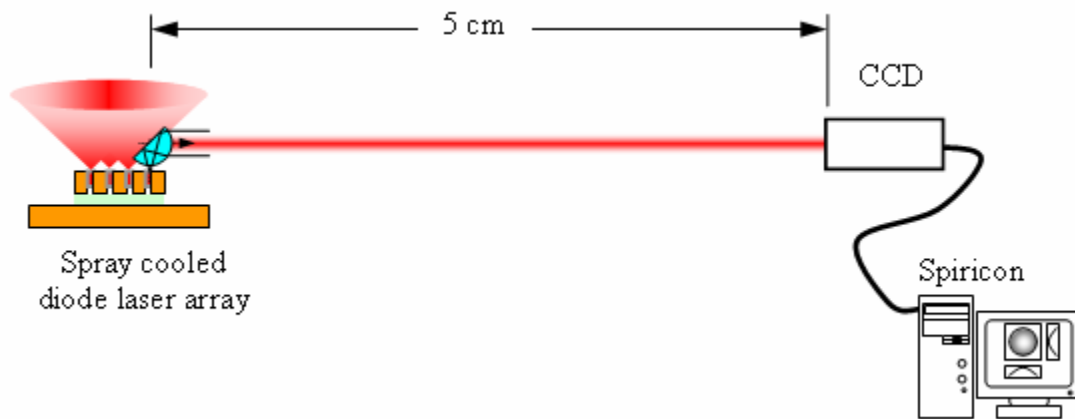
Figure 4.18: Experimental setup for BCP test

Figure 4.19, Figure 4.20 and Figure 4.21 show the experimental results of three different BCPs. For the curved-entrance and the curved-exit BCP designs, the radius of curvatures of the BCPs are 2 mm. The folded-ball BCP design has 0.5 mm radius of curvature. Figure 4.19, Figure 4.20(a) and Figure 4.21(a) represent the beam profiles

when emitters are located very close to paraxial focal points. A PULNiX TM745 CCD

camera was placed 19 cm away from the BCP to acquire the image of the beam profile.
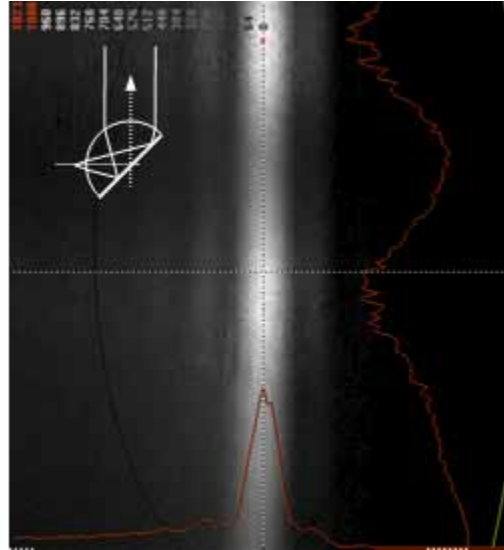
Figure 4.19: Folded-ball BCP output beam profile (R=0.5mm)
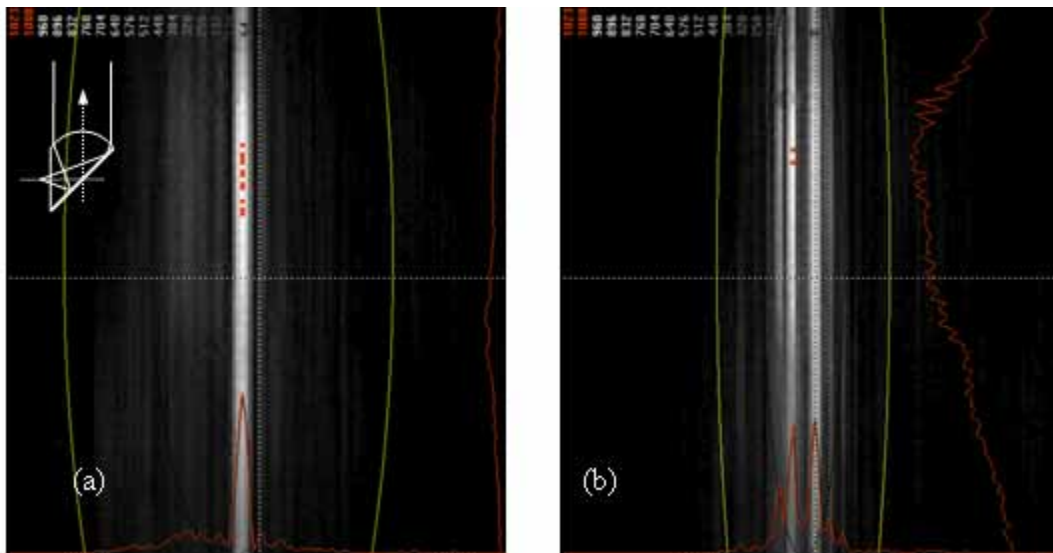
Figure 4.20: Curved-exit BCP output beam profile (R=2mm)

Figure 4.20(a) and (b) and Figure 4.21 (a)-(d) show a series of beam profiles when the emitter position is moved from the paraxial focal point toward the marginal focal point of the curved-entrance BCP. They show typical spherical aberration interference patterns. It is obvious that the curved-entrance BCP has the most severe spherical aberration as discussed above. The interference pattern due to spherical aberration might cause problems in certain applications. There are two major ways to eliminate the interference patterns: one is to use a conic surface or use the curved-exit BCP design to minimize the spherical aberration, and the other is to move the emitter closer than the marginal focal point to avoid the overlapping of rays. The draw back of the second approach is that the beam divergence angle is much larger. For a BK7 folded-ball BCP, the no interference condition will result in beam divergence about 5°.

Figure 4.22 shows the cross sections of the beam profiles of Figure 4.19, Figure 4.20(a) and Figure 4.21(a). The FWHM is smaller than 0.5° for all three different designs and is consistent with ASAP simulations for these BCPs.
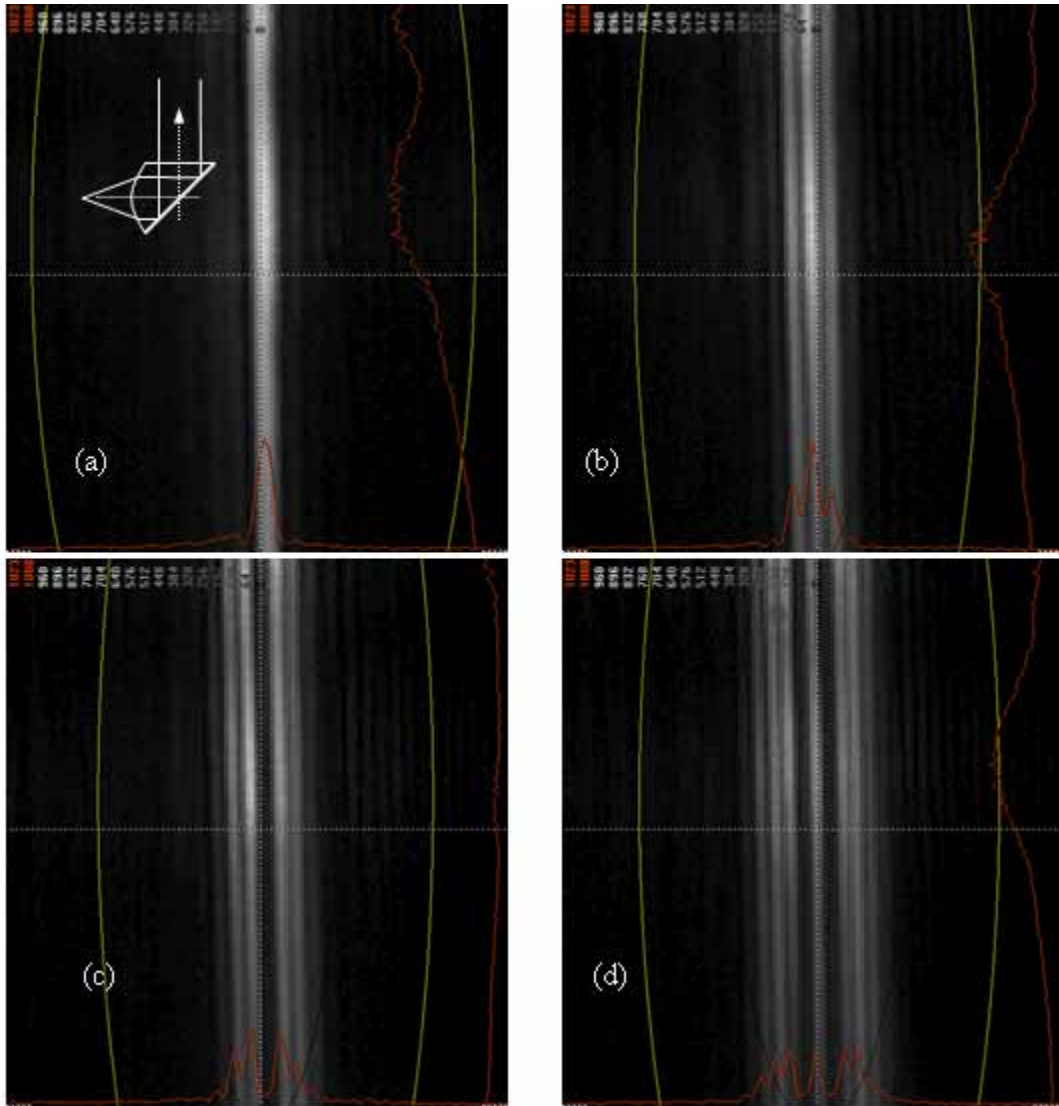
Figure 4.21: Curved-entrance BCP output beam profile (R=2mm)
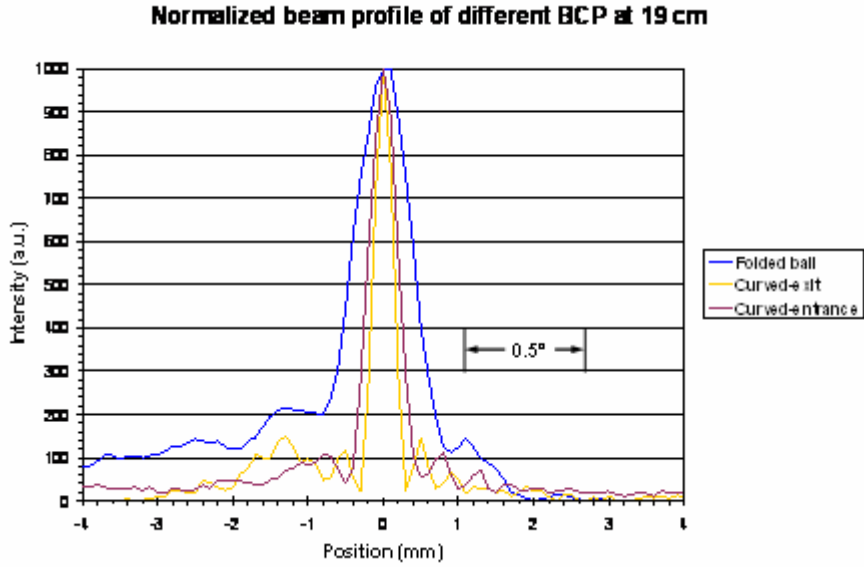
Figure 4.22: BCP beam profiles of different BCP designs

Based on the study of allowed acceptance angle described above we experimentally attempted to tune the beam angle by titling the BCP. Because of the capability of angular tuning shown in Figure 4.4 – Figure 4.9, we demonstrated that two BCPs can bring the two outputs from two different diode bars to the same position. This implies we can use BCPs in a diode laser array to recover the power density with less cooling demand. The concept is shown in Figure 4.23. However, because this capability is based on the angular tuning, it is limited by the angular tuning range of the BCP. Therefore, the illuminated area can't be too close to the diode laser array because it will require too large tuning angles for the BCPs far from the illuminated area.
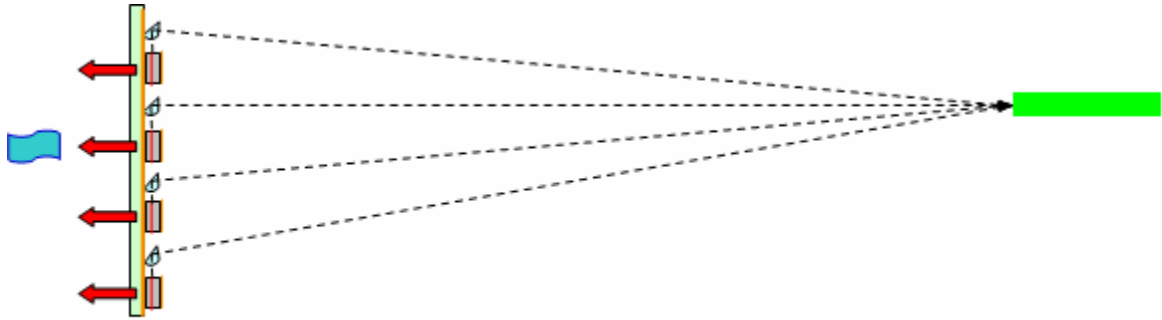
Figure 4.23: The concept of using BCPs to recover the power with less cooling demand

4.5 Summary of the properties of BCPs

A BCP is a new type of optic which is a combination of mirror and lens. It provides the capabilities to collimate the fast divergence angle and to adjust the output beam angle of a diode laser bar. Detailed analyses of the properties of the folded-ball design and the curved-exit design have been presented. The results show that BCPs should be made from higher index refraction materials to achieve larger acceptance angles and shorter focal length. Also, ASAP simulations agree with the experimental results for focusing a diode laser bar's output with BCPs. A BCP can focus the fast divergence angle from 35° to less than 0.5°.

5. BEAM CONTROL PRISM PACKAGING DESIGN (BCPP)

In chapter 3, we demonstrated that spray cooling is an effective and efficient way to cool a diode laser array generating a heat flux of 400 W/cm^2 or even higher. In a traditional stack package of diode bars there is a relatively long cooling path resulting in unwanted thermal resistance. Even though spray cooling can provide very a high heat transfer coefficient a long cooling path can keep the emitter temperature too high. Therefore, a new packaging method is needed. The most straightforward packaging arrangement is to put the p-side of the diode emitters closer to the coolant and lying parallel to the cooling surface. In such a circumstance extracting the light from the diode requires such optical devices as BCPs..

5.1 Basic design concept

An improved package design for diode laser arrays has to result in lower emitter temperatures and good optical output. We categorize BCPP design issues into four different groups. They are optical, thermal, mechanical and electrical considerations and their interactions with each other. These issues make the BCPP design complex.

Optical issues are directly related to the performance of the diode array. The concepts of the BCP have been discussed thoroughly in the previous chapter. A good BCP needs to have no absorption at the diode wavelength, large acceptance angles, low

aberration, small size, short back focal length, minimal positioning accuracy requirements, and a large angular tuning range.

Thermal issues focus on reducing the emitter temperature. For a good design, lower emitter temperature, faster thermal response time, and good temperature uniformity along the diode bar are the targets to be achieved.

Mechanical issues are really related to how to make the final product. These issues are very practical concerns. High packing density, ease of manufacture, simple assembly procedure, better positioning tolerance, and fewer parts are considered in improved mechanical design.

Electrical issues are conceptually simple. A serial electrical connection of diode bars is preferred for the diode laser array because the voltage drop across a typical diode bar is only a few volts, but the current can be quite high, 40 A or more. If the electric connection is in parallel, this requires a very high current, but low voltage power supply which is difficult to obtain.

Beyond these four packaging issues cost is also a major consideration for a practical design. The smaller the BCP is, the higher the packing density can be. A smaller BCP, however, requires higher positioning accuracy and it's also harder to make. On the contrary, if we use a larger BCP, the part of BCP below the optical axis (see Figure 5.1) is larger. This can mean a longer cooling path in the package. We can remove some part of the BCP to solve this problem but it will require extra work and add to the cost of the package.

The substrate design determines the thermal properties of the whole system. The chosen material should have high thermal conductivity and should be easily machined.

Also, the p-electrode of the diode bar will be directly attached to the substrate through the p electrode and so a proper method of attachment should be chosen. Thermal resistance in the interface between substrate, electrodes and diode bar is also critical.

The thermal resistance, temperature uniformity and electronic connection are the three major issues in selecting a package design. Lower thermal resistance requires shortening the cooling path from heat source to the coolant and/or use of a high thermal conductivity material as the substrate. This low thermal resistance provides a faster thermal response time. In other words, we can have better control of the diode temperature and consequently, of the output wavelength. Good temperature uniformity gives a better wavelength distribution along the diode bar. In most cases, the end emitters in a bar have lower temperatures than the emitters at the center because they lack emitters on one side. Therefore, we may have to change the substrate design to keep the edge emitters warmer.

Since BCPs can redirect the light into the desired direction, we can put the p-side of the diode laser much closer to the coolant to achieve lower thermal resistance. In the following example, we consider using a commercially available 1 mm diameter BK7 half-rod with a high reflection coating on the flat surface as our BCP. AR coatings might be needed on the curved surfaces.

Figure 5.1 shows the basic BCPP we suggest. The substrate can be either a piece of metal or an electrical insulator. If we choose a metallic substrate, another layer of insulator, e.g., GaAs, must be deposited on top of the substrate in order to enable serial electrical connection. The p-side electrode is deposited or placed directly on the insulator layer of a metallic substrate or directly on the insulator substrate. Since there will be

about 40 A passing through the electrodes, heat will be generated in these electrodes. However, the p-electrode is immediately on top of the substrate and the waste heat so generated can be removed directly. Therefore, the thickness of the p-side electrode is not too critical. However, the n-side electrode has a longer cooling path. Hence, we must make the cross section of n-side electrode large to reduce Ohmic heat generation.
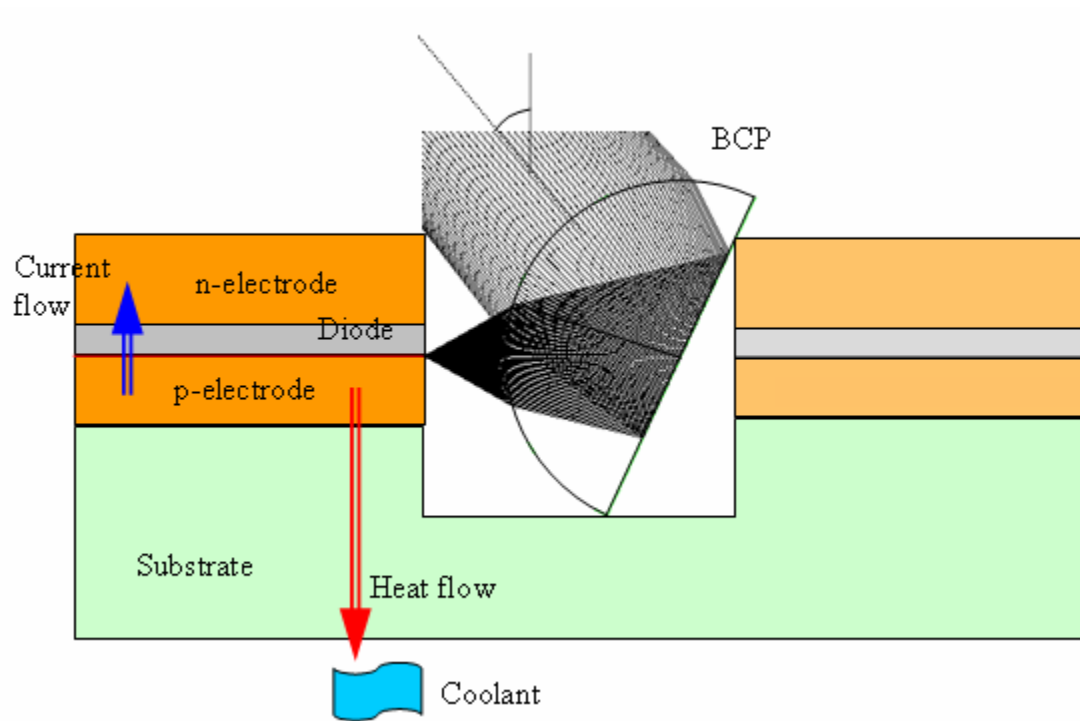
Figure 5.1: The Basic structure of the BCPP

The BCP has a finite size and the diode laser has to be on the optical axis. To reduce the emitter temperature, the p-side of the diode bar has to be placed closer to the coolant. Consequently, the diode has to be lifted higher or the BCP has to sit in a groove. The larger the BCP, the further will be the vertical distance between the p-side and the

lower part of BCP. In other words, assuming the bottom of the substrate is flat, the distance between the p-side of the diode and the coolant will be larger if the BCP is large.
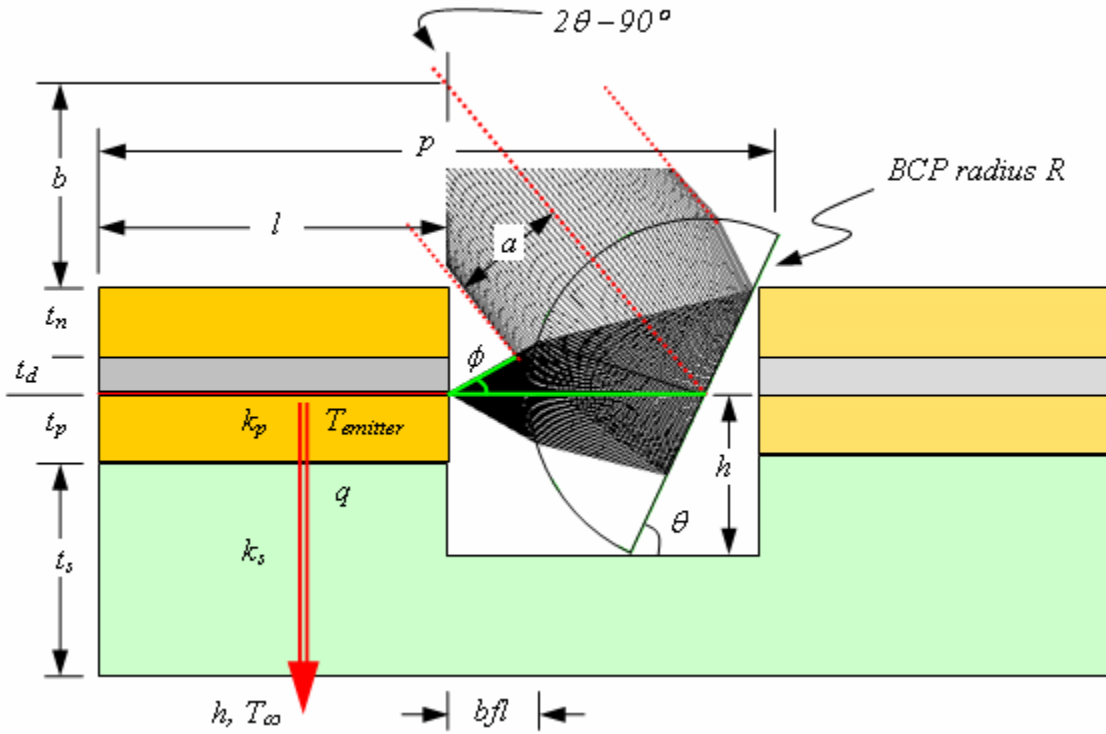
Figure 5.2: Parameters of the BCPP

5.2 Optical issues

Figure 5.2 defines several parameters for the BCPP design. We can write down several equations to represent the relationship among these parameters.

1. Channel depth equation

$$\sin \theta = \frac{h}{R} \tag{5.1}$$

2. Pitch equation

$$p = l + bfl + R + R\cos\theta \tag{5.2}$$

3. N-electrode non-blocking condition

$$b + t_n + t_d = (bfl + R) \cdot \tan 2\theta \tag{5.3}$$

$$b\cos 2\theta < a \tag{5.4}$$

4. Output beam radius equation

$$a(R, n, \phi) \tag{5.5}$$

Equation (5.5) can't be represented in a simple form. For a typical 60° full divergence angle, we can use numerical methods to obtain the beam radius a versus the folded-ball BCP index of refraction as shown in Figure 5.3 for the case where the light source is placed at the paraxial focal point. A larger divergence angle does not have a solution when the position of light source is farther than this because the marginal rays might not enter the BCP. The folded-ball radius is set as 0.5 mm in this figure. For convenience and simplicity, we can consider a, the output beam radius defined in Figure 5.2, is 0.3 mm for the following calculation.
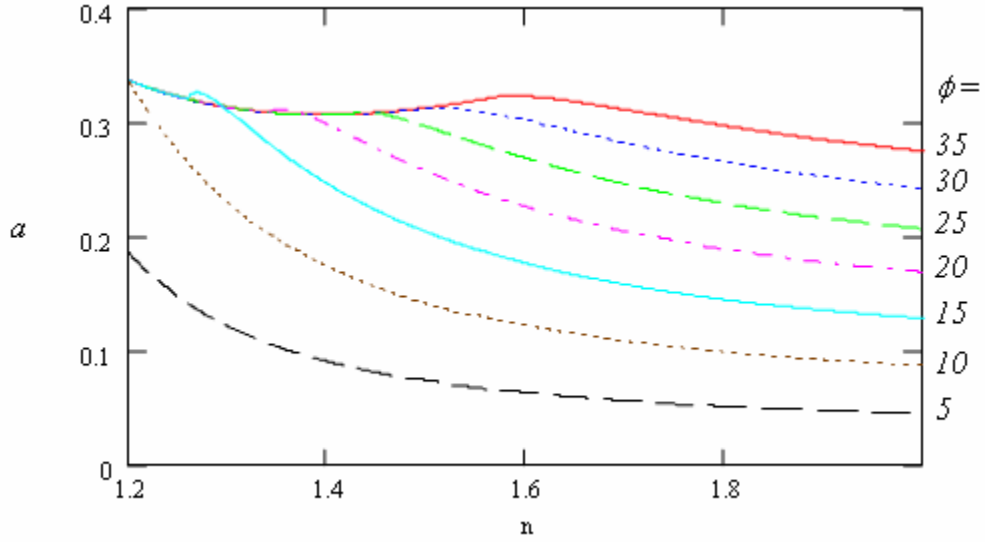
Figure 5.3: Output beam radius, a, versus BCP index of refraction for different ϕ angles

Equation (5.6) is the paraxial focal length of a cylindrical lens.

$$f = \frac{nR}{n-1} \tag{5.6}$$

$$bfl = f\frac{2-n}{n} = \frac{2-n}{n-1} \cdot R \tag{5.7}$$

Equations (5.1)-(5.7) provide the guidelines for the BCPP design. A preferred BCPP should have small p, $T_{emitter}$, and satisfy equation (5.4).

If we consider a beam angle of 90° or the BCP tilt angle $\theta = 45°$, Equation (5.4) will automatically be satisfied. Obviously, we should choose smaller BCPs to reduce the pitch and the cooling path. From Equations (4.1)-(4.5), we know, however, that a smaller BCP will require higher positioning precision. Also, a smaller BCP is much harder to make. In addition, if a smaller BCP is used, the angular tuning range will be limited by Equation (5.4).

61

5.3 Electric connection

Figure 5.2 shows the basic design concept and the structure of the BCPP without considering the electrical connection. As discussed above serial electrical connection is preferred. Several ways have been proposed to achieve the desired series connection. There is also another concern about the current directions on the electrodes as shown in Figure 5.4. We call a design in which the current direction in the p-electrode is the same as in the n-electrode a case of parallel current. If the direction is opposite we call the case one of anti-parallel current.
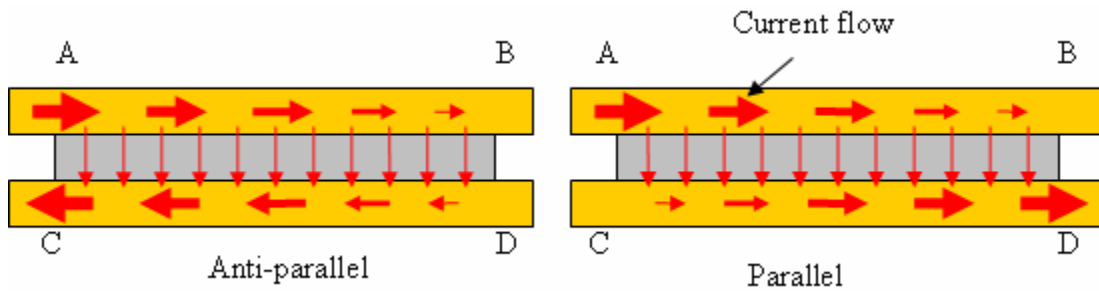
Figure 5.4: Current directions in the p- and n-electrodes

The current direction will influence the temperature distribution in the diode bar because of Ohmic heating in the electrodes. Under anti-parallel conditions, Sides A and C have higher current densities, higher ohm heating, and higher temperature compared with sides B and D (See Figure 5.4). Consequently, the parallel current case is preferred.

Figure 5.5 shows a large array with patterned p-electrodes, known as a "vertical" connection. This design provides a simple way to connect the diode bars and extend the size of the array. However, the current direction in the p-electrode and the n-electrode

are anti-parallel. Figure 5.6 is the modified version of Figure 5.5 which is known as the "horizontal" connection.
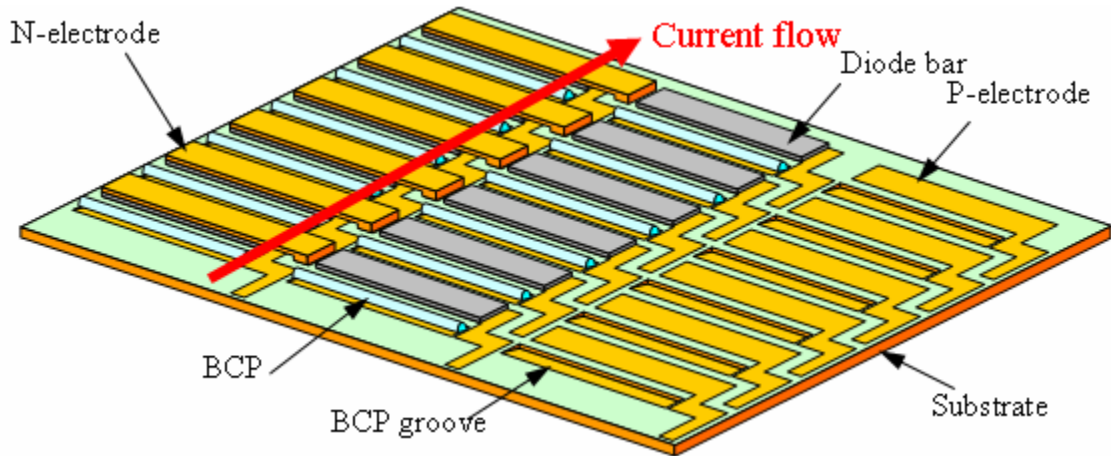
Figure 5.5: Packing example for larger array with "vertical" electrical connections
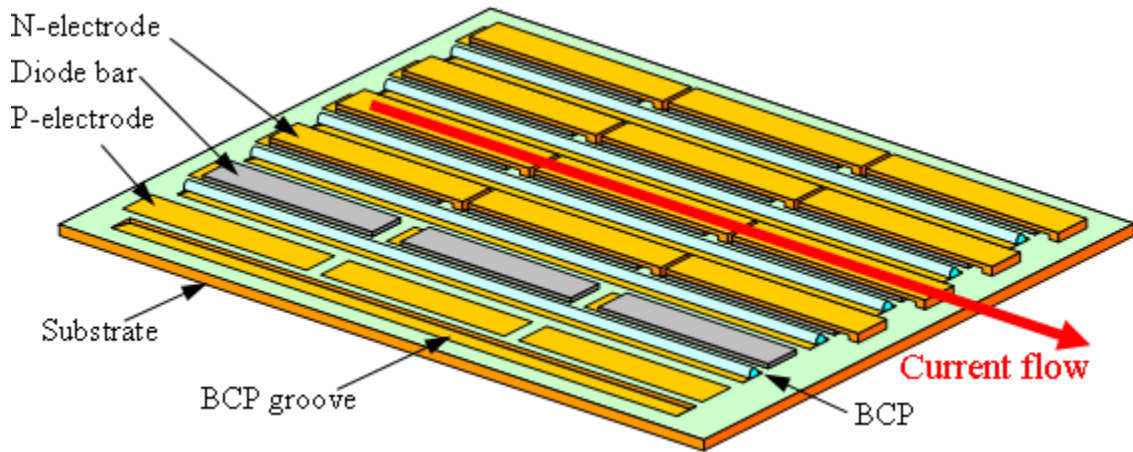
Figure 5.6: Packing example for larger array with "horizontal" electrical connections

In the case shown in Figure 5.6 the electrode shapes are relatively simple. The spacing between bars can be shortened compared to that required in Figure 5.5. This design can also use long BCPs which allow several diode bars to share a single BCP.

Also, the current direction is parallel. However, as Equations (4.4) and (4.5) show, a longer BCP requires a higher angular positioning precision. Also, between each row, a serial connection is harder to achieve. Therefore, this design is not suitable for a small size array which only contains a few diode bars. Another approach is shown in Figure 5.7. It is also the design used in our experiments. This design uses the n-electrode to achieve the serial connection. Its n-electrode is complicated and needs two different designs which are mirror images of each other. The higher end of the n-electrode ensures it doesn't short circuit. Essentially, this design is also a modification of Figure 5.5. It is suitable for any size of the array. Also, the current directions on the p-electrode and the n-electrode are parallel.
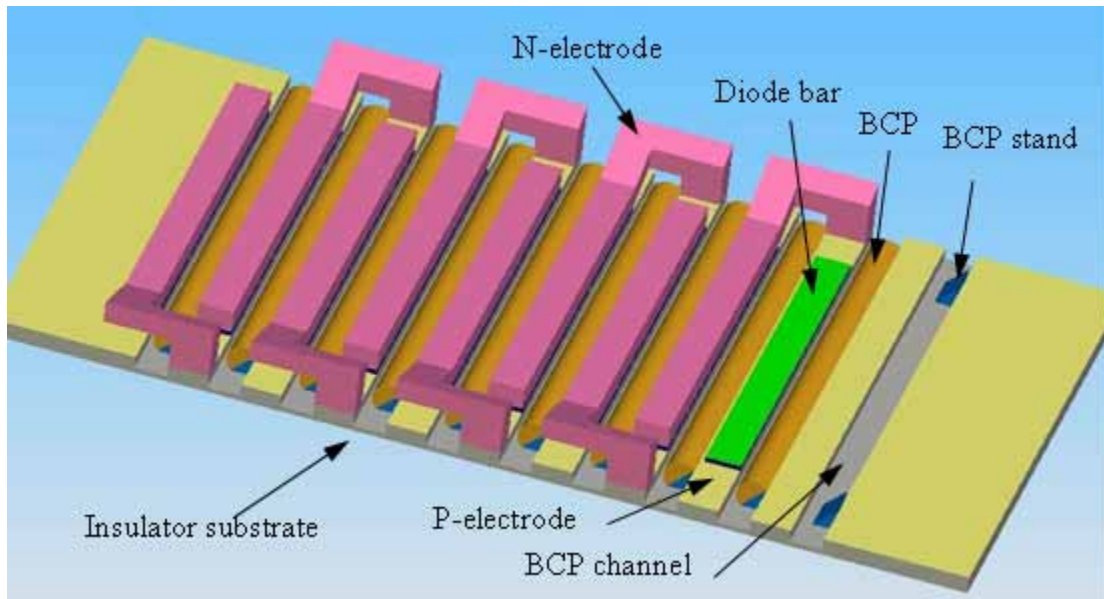
Figure 5.7: BCPP with shaped n-electrodes

5.4 Thermal issues

Thermal issues are the major concern of BCPP design. 1D temperature distribution can be computed using Fourier's law and Newton's law of cooling. The system as shown in Figure 5.2 can be described as having thermal resistance given by

$$R_{th} = \frac{1}{h \cdot A} + \sum_i \frac{t_i}{k_i \cdot A} = \frac{1}{h \cdot A} + \frac{t_p}{k_p \cdot A} + \frac{t_s}{k_s \cdot A} \qquad (5.8)$$

$$T_{emitter} = T_\infty + R_{th} \cdot q \qquad (5.9)$$

k are the thermal conductivities of the materials. h is the heat transfer coefficient between the coolant and the contacting surface. A is the area of the interface. t_i is the thickness of the material and q is the heat flow of the heat source. We know that choosing materials with high thermal conductivities and using a very thin substrate will reduce the emitter temperatures. Also, a higher heat transfer coefficient cooling method should be employed.

For the conductive p-electrode, the most convenient material with high electric and thermal conductivity is copper. An electrically insulating material with a high thermal conductivity is not common. The most desirable insulating material is diamond. It has the unbeatable thermal conductivity of 2300 W/m·K. However, its hardness and availability present major problems. Also, attaching copper or some other material on the diamond is not an easy task. Another commonly used material is BeO which has the thermal conductivity of 272 W/m·K. It is easier to obtain and all of the peripheral techniques for handling BeO are well-developed. The direct bond copper is a mature technique to adhere the patterned copper film on top of the BeO substrate. Also, BeO is

relatively easy to machine. The only draw back is its toxicity, but many companies have facilities to safely machine this material.

A diode emitter generates waste heat of about 2 W, and the emitter area is about 10^{-7} m^2. Therefore, an effective cooling method is necessary. In our experiment, we use evaporated low pressure water spray cooling for our test diode array as mentioned in Chapter 3.

When dealing with the real system, we should consider the 3D case and use the heat diffusion equation:

$$k\nabla^2 T + \dot{q} = \rho \cdot c_p \cdot \frac{\partial T}{\partial t} \qquad (5.10)$$

For a complicate geometry like the BCPP, the only way to solve the problem is through numerical methods. We used FemLab®, the finite element analysis software program, to simulate the temperature distribution of the BCPP.

5.5 Mechanical issues

Mechanical issues are the most practical and trivial part of the design. The thermal expansion coefficients of the conduction layer and the insulator layer are usually different. This mismatch might cause thermal stress or even distort the substrate. Also, the total thickness of the substrate needs to be strong enough to sustain the pressure difference due to the active cooling. For example, the low pressure water, evaporative spray cooling we used must sustain a pressure difference of about 1 atm between the diode array and the spray cooling chamber.

Keeping the BCP precisely positioned is also an important mechanical issue. Equations (4.1)-(4.5) calculate the translational and the angular position tolerances. In a practical design a passive means to align the BCP is essential.

5.6 Experimental design

We consider the folded-ball BCP design with BCPs made of BK7 glass (n=1.51 at 808 nm) with radius of curvature 0.5 mm. We chose the folded ball BCP because it is simple and inexpensive to prepare. The output beam angle was selected as 90° and so the BCP tilt angle is 45°.

Assume the beam angle tolerance $\Delta\Theta$ is equal to 3° and we can obtain the translational and the angular positioning tolerance from Equations (4.1)-(4.5) as

Table 5.1 BCP positioning tolerance

$\Delta X=$	67 μm
$\Delta Z=$	43 μm
$\Delta\alpha=$	4.3 mrad
$\Delta\beta=$	26 mrad
$\Delta\gamma=$	6.7 mrad

The substrate design was most critical. A BeO substrate with directly bonded copper to serve as the p-electrode was chosen because of it is inexpensive to produce using relatively mature methods. Copper films can be directly bonded to a BeO surface through a high temperature reaction. However, the expansion coefficients of the copper and BeO are quite different. This difference induces stress in the substrate when the substrate cools down to room temperature. Therefore, an additional direct bond copper film needs to be added on the opposite side of the BeO substrate to balance the stress.

Hence, the final substrate with the p-electrode directly bonded to the BeO became a copper-BeO-copper sandwich. A diamond saw was used to cut through the top n-electrode copper layer to achieve electrical isolation between the copper stripes serving as the p-electrodes. Figure 5.8 shows the top and side view of the substrate.
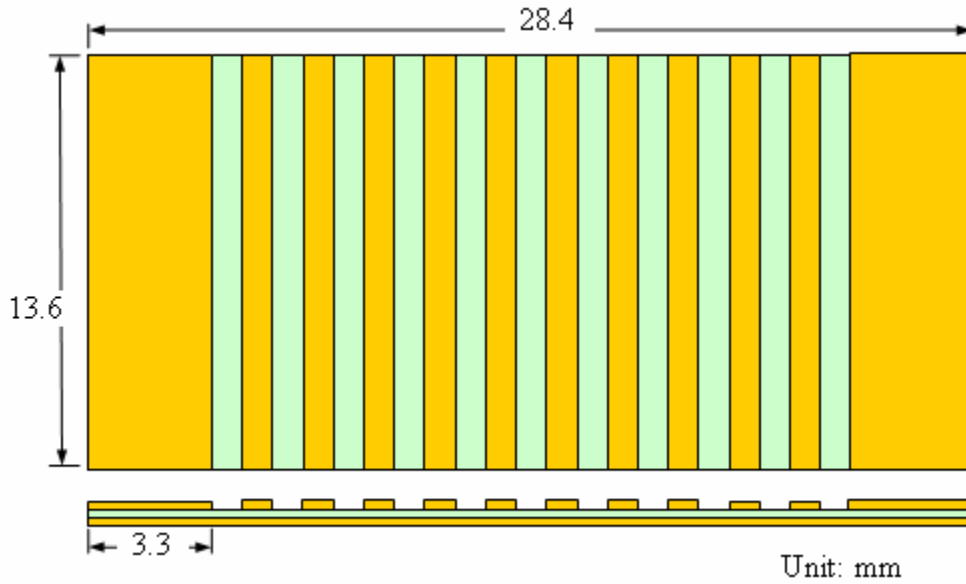
Figure 5.8: Sandwiched copper-BeO-copper BCPP substrate design

There are two methods to fix the BCP in place. One is using a BCP stand and the other is using dual BCPs design. The BCP stand is a triangular piece of glass or any material that is sturdy, stable and easy to machine. Figure 5.9: shows the detailed dimensions of the BCPP substrate employing the BCP stand concept.
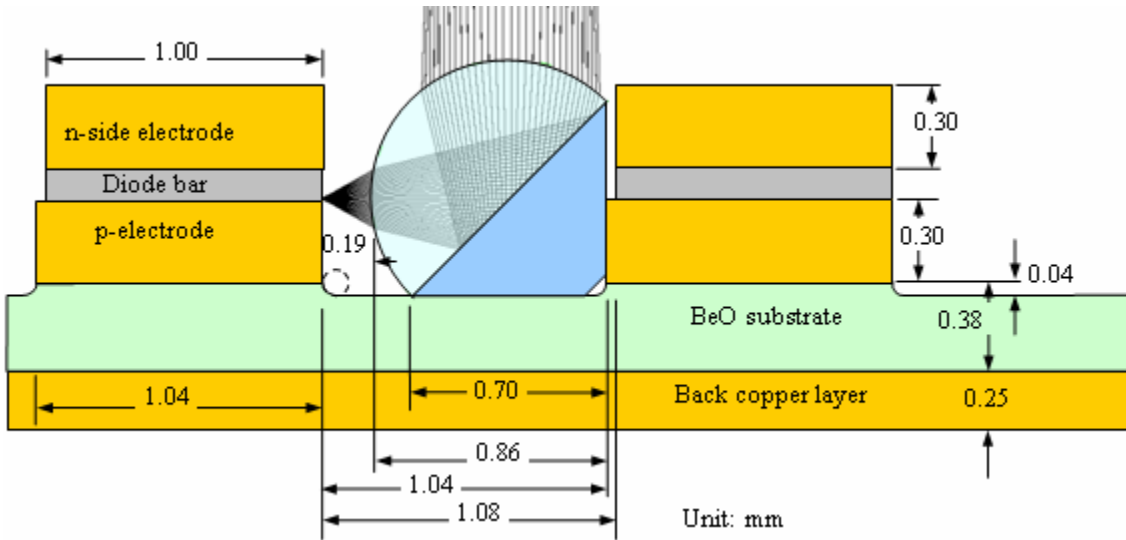
Figure 5.9: Detailed dimensions of BCPP substrate employing BCP stand concept.
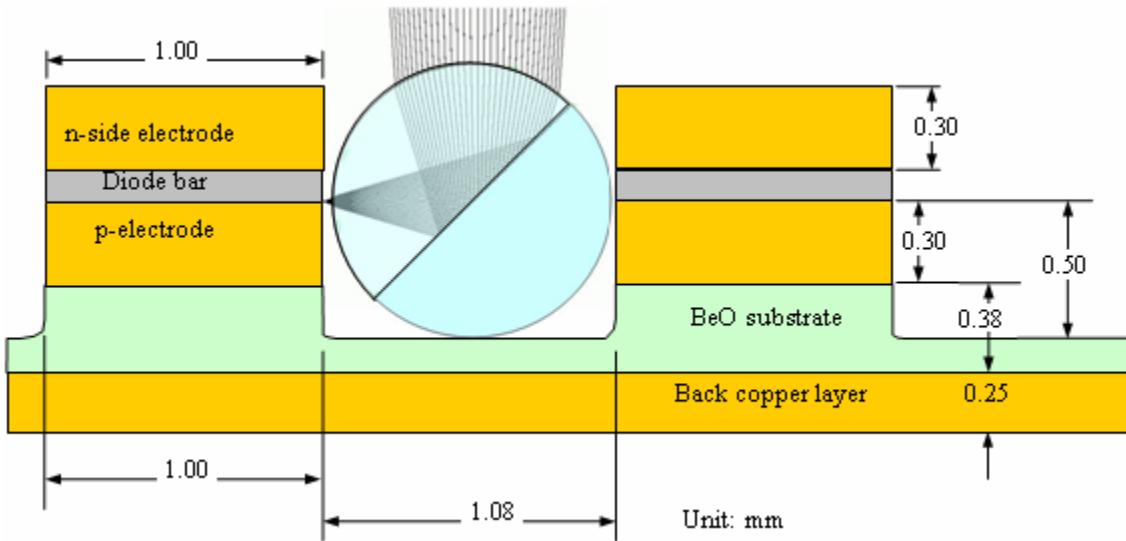
Figure 5.10: Detailed dimensions of BCPP substrate employing a dual BCP

A BCP stand design gives a fixed beam angle and a more compact design, and this design has the potential to achieve a shorter cooling distance between the diode and the coolant. The dual BCP or the glued-BCP design is accomplished by gluing the BCP

to another piece of a half rod which has the same dimension of the BCP. This makes the whole piece become a complete rod. Figure 5.10 shows the detailed dimensions of the glued-BCP design. Because of the symmetry, this feature gives more freedom for angle tuning as long as the HR coating on the flat surface remains reflective. Because the rod-shaped BCP has only one point in contact with the bottom of the BCP channel the flatness of the channel is not as critical as in the design employing a BCP stand. Currently, it is difficult to use a diamond saw to produce a flat bottomed cut for the BCP channel. Figure 5.11 shows microscope photos of several typical cross sectional views of the BCP channels produced using different size diamond saws.
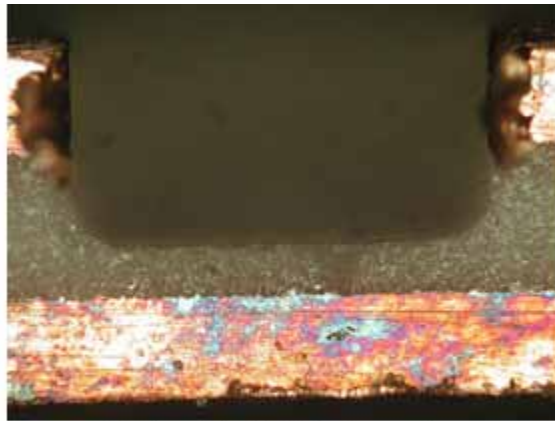
(a) An ideal BCP channel
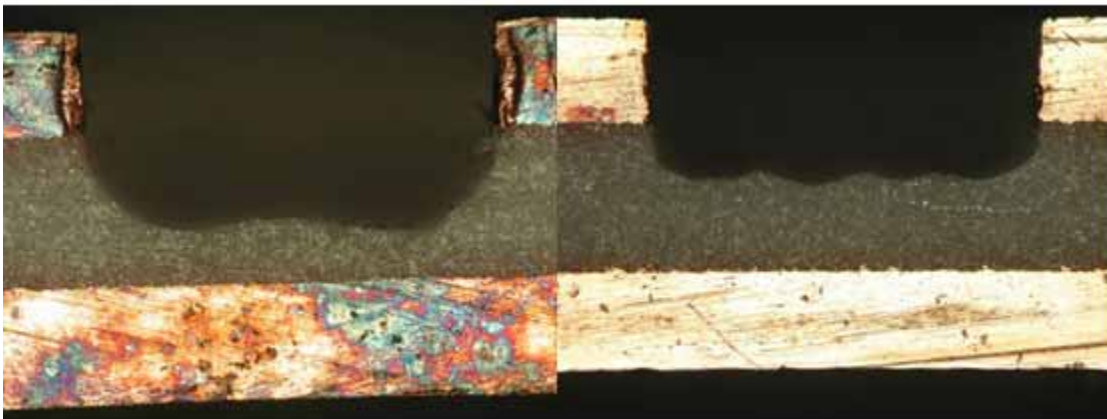
(b) 1 mm wide saw cutting result   (c) 0.3 mm wide saw cutting result

Figure 5.11: BCP channel side views of different cutting methods

Figure 5.11 (a) shows a cross section of a cut made using a new 1 mm thick diamond saw. The edge and the bottom of the channel are flat and smooth. However, a diamond saw tends to wear out and makes a channel with cross section as shown in Fig. 5.11 (b). Using a narrower diamond saw will leave several lumps at the bottom of the channel as shown in Fig. 5.11 (c). The lumpy bottom might make the BCP stand have an undesirable tilt. However the dual BCP design is quite insensitive to the uneven channel bottom. As long as the contact points between the dual BCP and the channel bottom

71

have the same height, the beam output remains the same. Since copper is a relatively soft material for machining, the diamond saw pushes and distorts the copper edges of the channel when cutting. Such distortion causes all p-electrode surfaces to become concave. Figure 5.12 shows the surface profile of a p-electrode after the cutting process. The height difference between the center and the edge of the p-electrode can be as large as 12 μm. An uneven surface potentially can cause a solder void between the electrode and the diode bar and/or an extra thickness of solder. Consequently, all surfaces were polished after the cutting process.
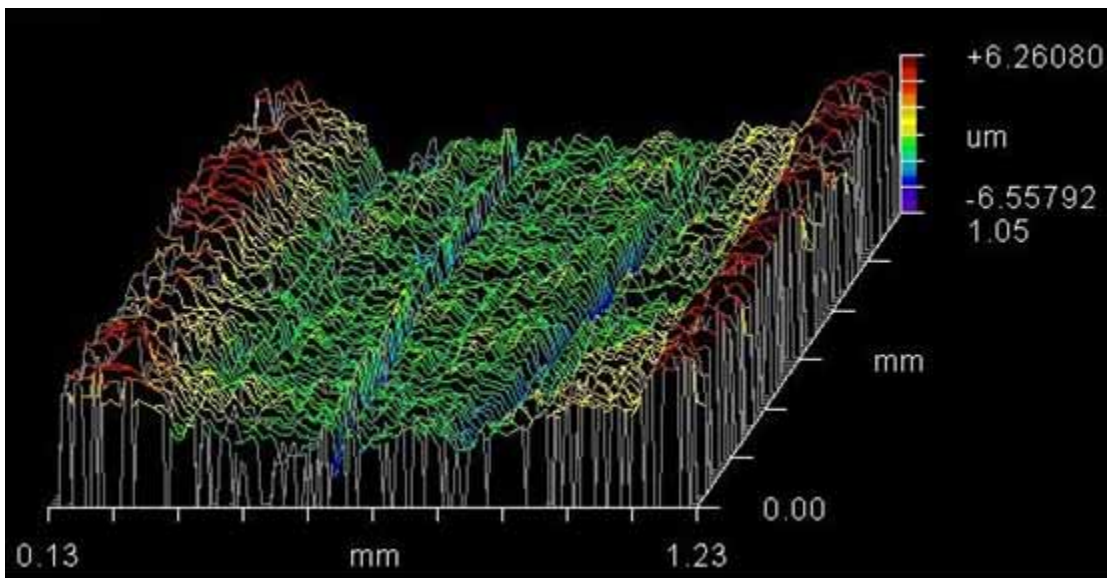
Figure 5.12: The n-electrode surface plot after cutting the channel

The N-electrodes have two designs because of the alternating connection directions along the array as shown in Figure 5.7. Figure 5.13 shows one of the designs. The two designs are mutual mirror image of each other. The end structure of the n-electrode ensures the electrodes don't short each other electrically.

72
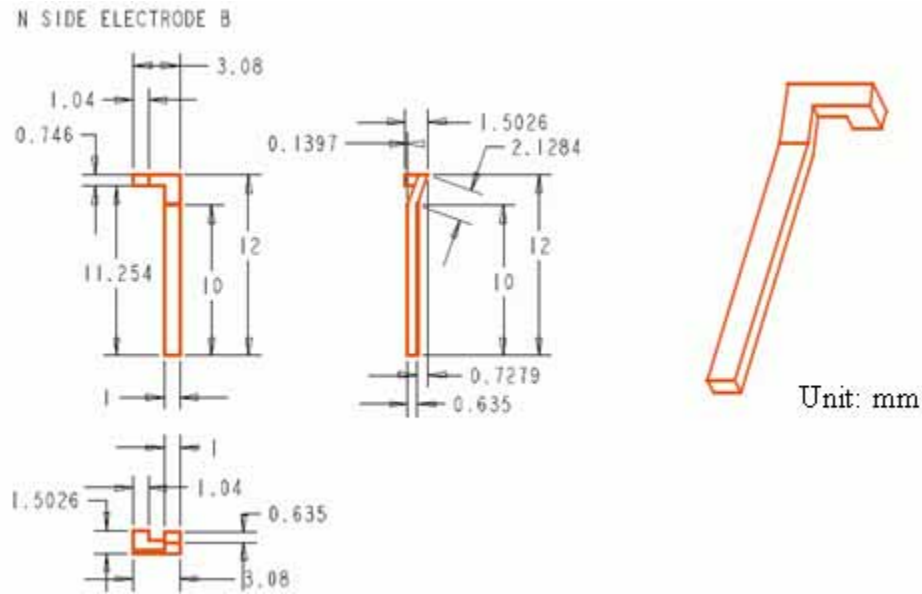
Figure 5.13: The n-electrode design

The assembly of the studied array was carried out by Decade Optical Systems. The first step was to assemble the diode bars and the n-electrodes on top of the substrate. Thin film solder sheets were inserted between the diode bars, p-electrodes and n-electrodes. The whole system was placed on a special mount and placed in an oven that melts the solder films and completes the soldering process.

We did not cool the array directly through the back copper layer of the substrate. Instead the array was soldered to a heat exchanger which can be a traditional forced convection heat exchanger or a spray cooling chamber. The soldering step is similar to soldering the diode bars and the n-electrodes.

In our experiment, we used low pressure water spray cooling as the cooling method. Its heat transfer coefficient was about $1.5\text{-}2.0 \times 10^5$ W/m^{2}K as discussed in Chapter 3. However, an extra 1 mm thick copper layer was necessary to provide mechanical stiffness and to sustain the pressure difference between the spray cooling

chamber and the external environment. This extra copper layer increased the resulting emitter temperature slightly.

Placing a BCP in its channel in place is a major issue. For the BCP stand design, the positioning relies on the precision of the parts. It will only have a very limited range of fine tuning before curing the epoxy used to hold the BCP to the stand. On the contrary, the dual BCP design has a relatively large tuning range and the dual BCP is very easy to tune by rotating the rod slightly. This fine tuning procedure can be done two ways. One way is to drive the diode bars in the LED mode and the output light projected to a screen to monitor the beam angles while adjusting them as desired. The other way is to look directly into the BCPs under a microscope. If the BCP is well-aligned, the observer should see the image of the p-electrode and the diode bar p-edge at the center of the BCP. After the fine tuning process the BCPs were secured by UV curing the epoxy glue used to hold the BCP.

5.7 BCPP temperature distribution FEA results

We used FEMLAB finite element analysis to calculate the temperature distribution. Our calculation was based on the numerical values of dimensions and material parameters given in the diode bar manufacturer's data sheets Lasertel LT1200-40W and LT1300-60W shown in Table 5.2.

The simplest way to calculate the temperature distribution of the package was to set the heat source exactly on top of the p-electrode. Because the first BCPP diode array utilized micro channel cooling, a constant temperature boundary condition was used at the bottom surfaces in the following simulations. All other surfaces were selected as

insulating surfaces. Figure 5.14 shows that the single emitter temperature would be about

38°C. Figure 5.15 shows the temperature distribution along a diode bar. The edge

emitters have relatively lower temperatures compared to the emitters in the middle of the

bar. A similar effect can be observed when an entire BCPP array FEA is calculated. The

two end-most bars show slightly lower temperatures compared to the central bars. Figure

5.16 shows the temperatures of different bars in the array. Since there are channels

between bars the data points are discrete. As presented in Figure 5.17, the edge emitters'

temperatures are about 8°C lower than that of the central emitters when the waste heat is

60W. This is because the edge emitters lack heat sources to keep them warm. Similarly,

the edge effect makes the edge bars about 1.5°C cooler than the central bars as shown in

Figure 5.18.

Table 5.2 LaserTel LT1200-40W and 1300-60W diode laser specifications

LaserTel diode laser bars		LT1200-40W[3]	LT1300-60W[4]	Unit
Optical Characteristics	Output power	40	60	W
	Center wavelength	808	808	nm
	Center wavelength Tolerance	±5	±5	nm
	Wavelength temperature coefficient	0.3	0.3	nm/°C
	Spectral Width (FWHM)	2.5	2.5	nm
	Array Length	10	10	mm
	Number of Emitters	19	24	
	Emitter Size	150×1	200×1	μm
	Emitter Spacing (center-to-center)	500	200	μm
	Slow Axis Divergence (FWHM) SA	10°	10°	Degrees
	Fast Axis Divergence (FWHM) FA	35°	35°	Degrees
	Polarization	TE or TM	TE or TM	
Electrical Characteristics	Slope Efficiency	1.1	1.16	W/A
	Conversion Efficiency	50	49.19	%
	Threshold Current	8	12.35	A
	Operating Current	43	64.2	A
	Operating Voltage	1.9	1.9	V
	Series Resistance	0.004	0.00349	Ω
Thermal Characteristics	Thermal Resistance	-	-	°C/W
	Storage Temperature Range	-40 to 85	-40 to 85	°C

---

[3] http://www.lasertel.com/media/LT1200_40W.pdf
[4] Datasheet from Lasertel for LT1300 S/N AAB2639
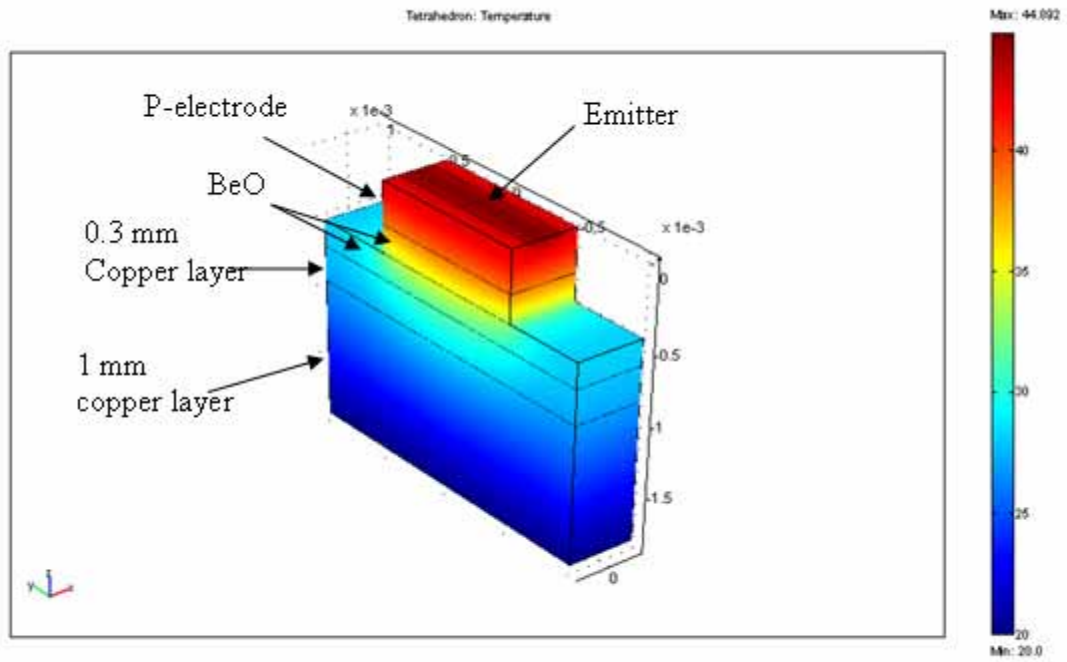
Figure 5.14: FEA computed temperature distribution of a single emitter in a 60W bar
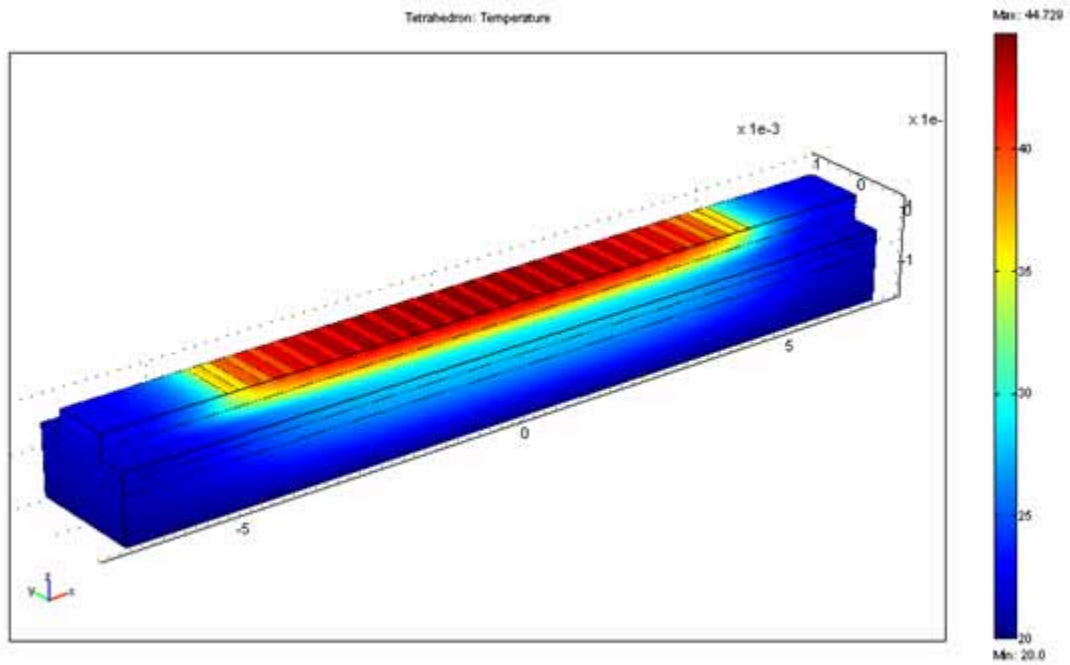
Figure 5.15: FEA computed temperature distribution of a single 60 W bar
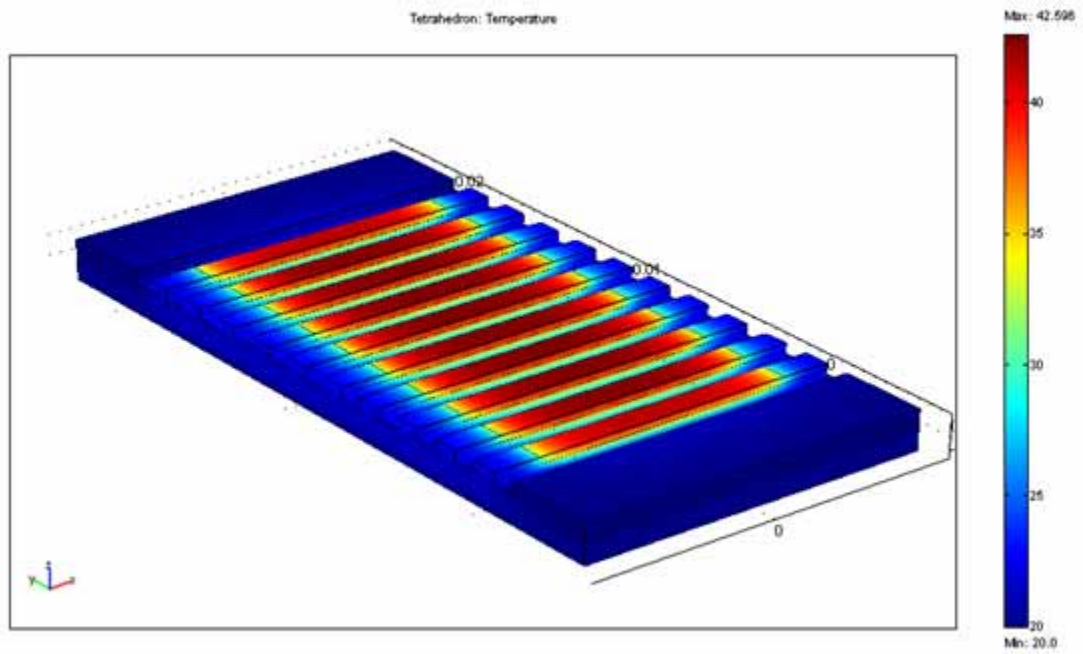
Figure 5.16: FEA computed temperature distribution of an entire BCPP array built with of 10 60W bars
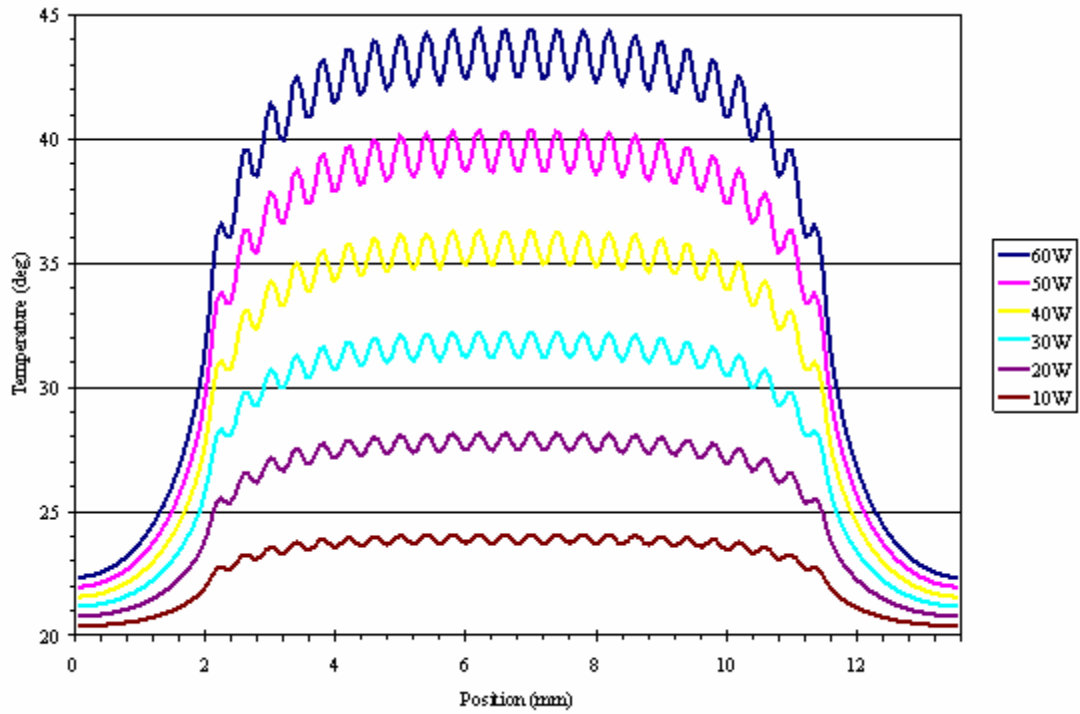
Figure 5.17 FEA computed temperature distribution of a single diode bar for different waste heat levels
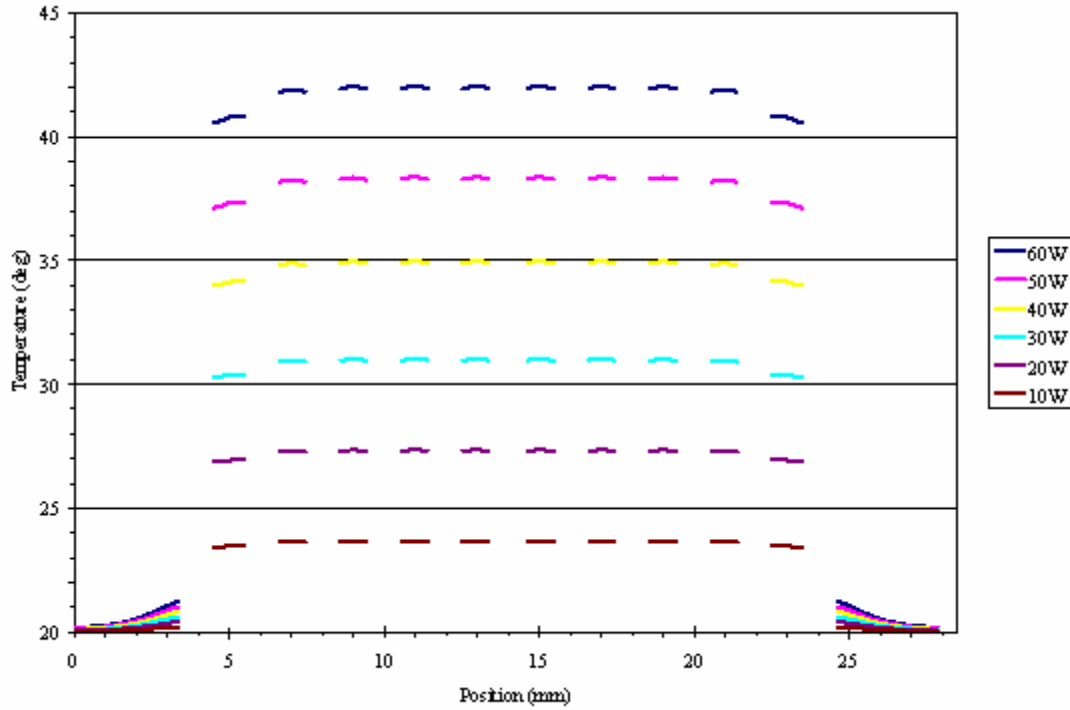
Figure 5.18: FEA computed temperature distribution in the emitter plane of the BCPP array for different waste heat levels

5.8 Experimental results

Figure 5.19 shows the top view of the BCPP array. This array is assembled by Decade Optical System, and is the very first BCPP array ever made. The BCPs are not aligned properly; hence, the laser output of each bar is directed in different directions, yet it shows the ability to aim all the beams to a certain spot if the BCPs tilt angles had been controlled properly when the array was assembled.
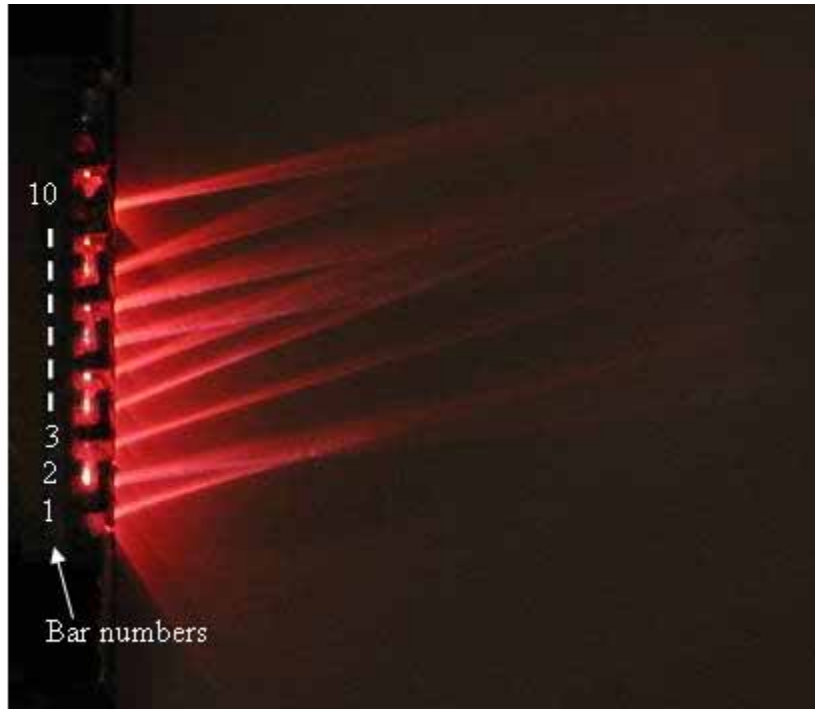
Figure 5.19: Top view of the BCPP array

Figure 5.20 shows the front view of the BCPP array and the numbering system for the bars and emitters. Since most of the beams are directed to oblique angles, the camera can take pictures at an angle to avoid the laser beams. The picture shows that bar 9 failed. Emitters 2 and 3 on bar 4 were not emitting. In bar 8, emitter 11 did not emit and emitter 12 has obviously lower strength than other emitters on this bar.

There is no good and direct way to measure the emitter temperatures because the emitters can't be directly observed. Even though an IR image cannot provide a precise temperature measurement, it still provides a qualitative temperature distribution of the BCPP array. Figure 5.21 show the IR image of the BCPP array. The image is taken with a FLIR PM290 IR camera which is placed at an angle to avoid direct illumination of the camera sensor by the laser beams. Comparing with Figure 5.20 and Figure 5.21, a hot

spot at bar 9 implies a short circuit which makes the bar fail. The positions of the failed emitters on bar 4 and bar 8 are indicated by green arrows. Both emitters show higher temperature than the other emitters implying that these two still have similar resistance compared with other emitters, but that the power passing through them is mostly converted into heat instead of light. The IR image also shows the edge effect of the bars and the array. Bar 3 and bar 4 showed higher temperatures roughly intermediate between emitter 2 and 8. There are three possible reasons that can cause this effect. One possibility is that the solder layers between the diode bar and electrodes are in poor contact in the corresponding regions. This allows more current to go through and increases the local temperature. Another possibility is the solder layer between the common substrate and the micro channel heat exchanger is thicker at this part. A thicker solder layer implies a longer cooling path and higher thermal resistance which increases the temperature of the emitters at this region. The other possibility is that the hot spot on bar # 4 generates extra heat and heats the neighboring area to a higher temperature.
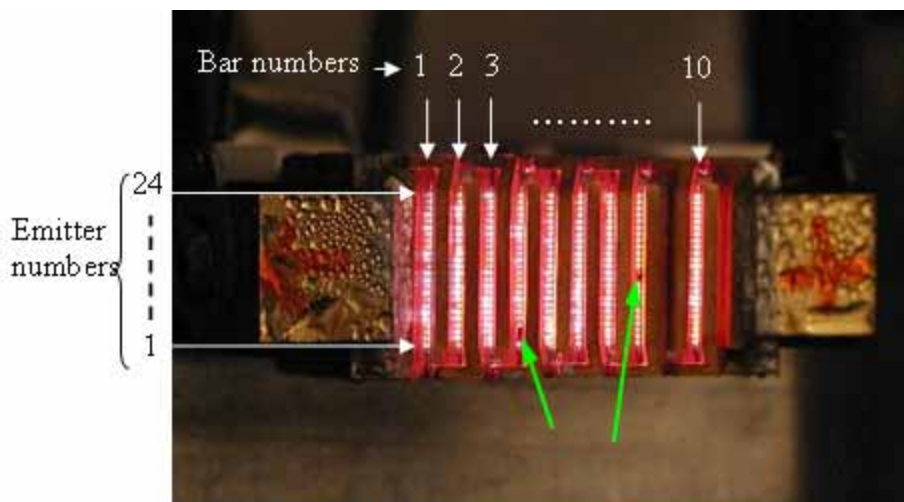
Figure 5.20: Front view of the BCPP array
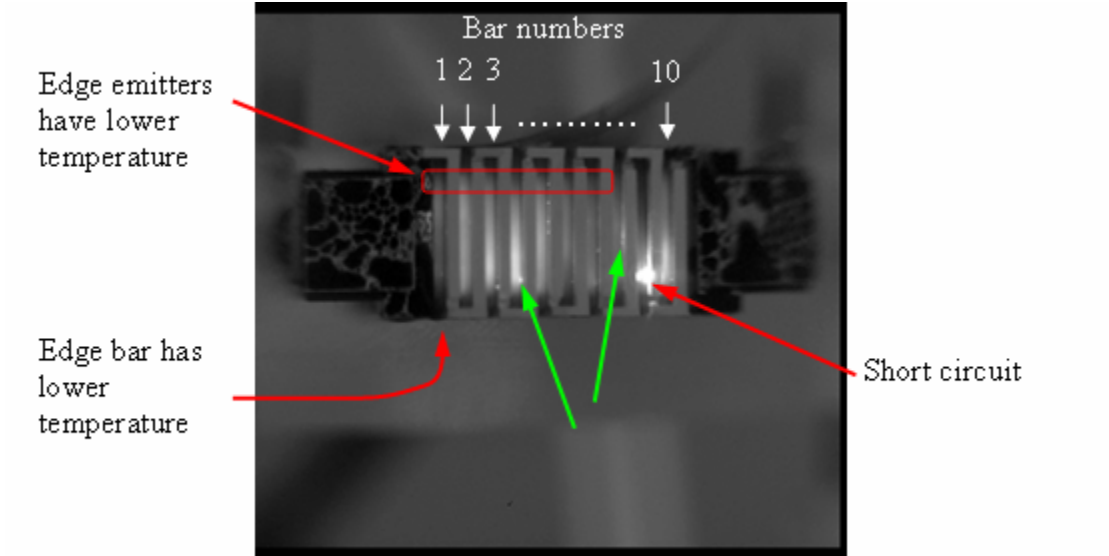
Figure 5.21: IR image of the BCPP array

A quick check of the total output spectrum was performed by using an Ocean Optics HR2000 spectrometer. The probe of the spectrometer was placed about 1 m away from the diode array to make sure the output beams were properly mixed so that the probe could receive light from most of the emitters. The experimental result is shown in Figure 5.22. When the total current is about 25 A, the peak wavelength is about 808 nm, and the FWHM is about 4 nm. However, the spectra show some long wavelength components which imply some emitters might be working at a temperature about 32°C higher than the average emitter temperature.
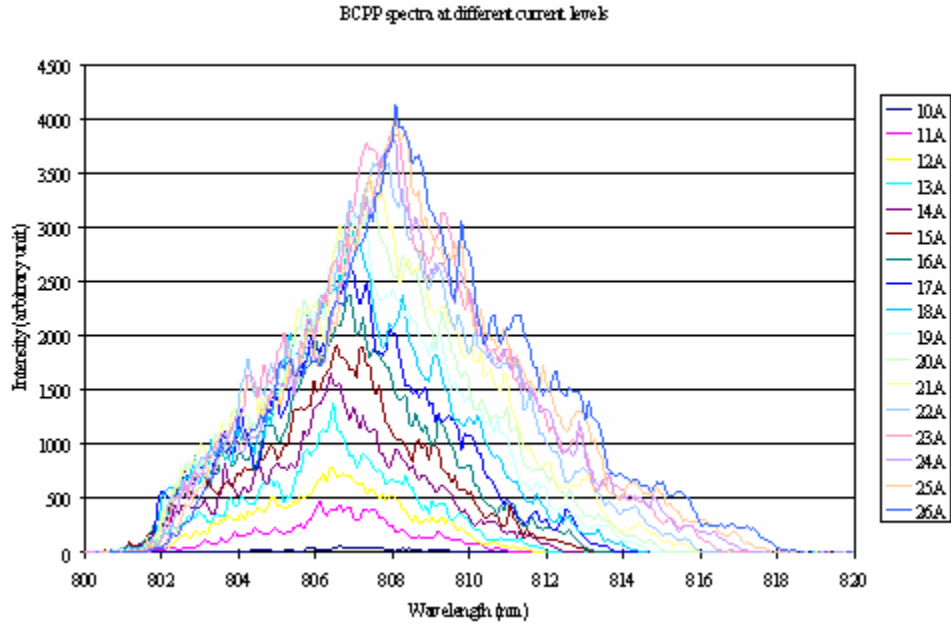
Figure 5.22: Output spectrum of the BCPP diode laser array for different current levels

Figure 5.23 shows the P-I curve and the efficiency of this BCPP array. The result shows the typical diode laser output behaviors. However, we suspected some emitters were working at an unusual high temperature as indicated by the spectral outputs shown in Figure 5.22. Hence, the maximum current applied to this array was 26 A.
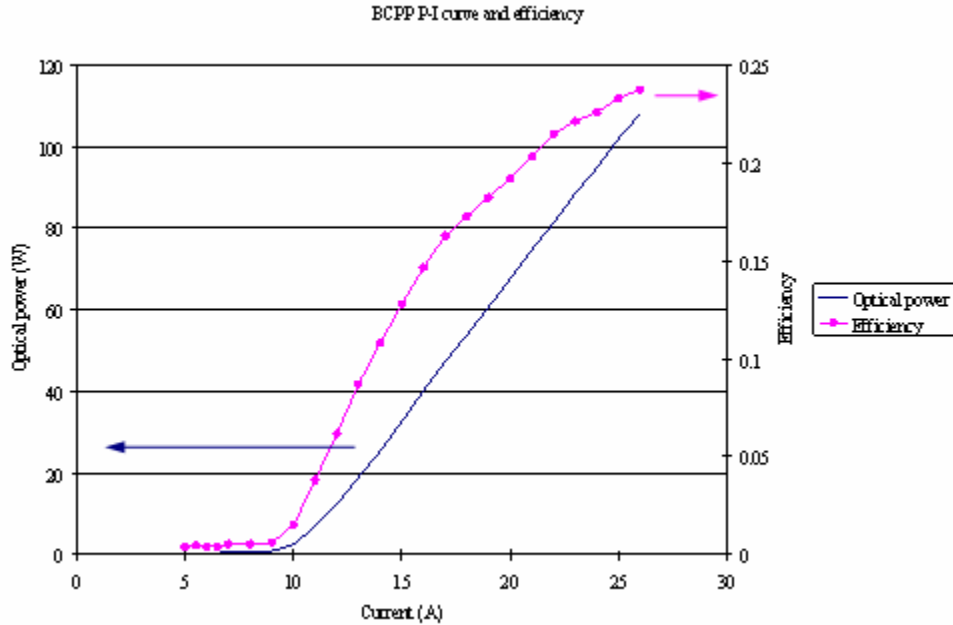
Figure 5.23: P-I curve and efficiency of the BCPP array

The emitter temperature can be calculated from its output spectrum and the temperature coefficient given in Table 5.2. By measuring the central wavelength of each emitter we can obtain the temperature distribution on the whole diode array. The wavelength measurement experiment is sketched in Figure 5.24.

The BCPP diode array was mounted on an X-Y stage. A 45° tilted microscope slide was used to redirect a small potion of the output beam horizontally. An imaging lens projected images of individual emitters on the image plane. We then used the Ocean Optics HR2000 spectrometer to measure the spectrum of each emitter. Because the output power of the array was so high, the reflected laser light from the first microscope slide was still strong enough to saturate and even damage the CCD of the spectrometer. In order to reduce the light intensity, another microscope slide was place before the

image plane. By moving the BCPP diode array position we can select which emitter image is projected on the fiber probe. In this manner all of the emitters' output spectra can be measured. Hence, the temperature distribution of the array could be calculated. Figure 5.25 shows the calculated temperature distribution of bars 1, 2, 3, 5, 6 and 7 when the applied current was 25 A where the trend of this calculated result is seen to be consistent with the IR image result. The edge effect is clear. The average temperature difference between the central emitters and the edge emitters is about 11.2°C while the simulation in Figure 5.17 shows a temperature difference about 8°C for the ideal case. Bar 5 (the central bar) and bar 1 (an edge bar) differ by about 14.5°C. The temperature of bar in the region of emitter 2 to 8 was higher than the average..

The experimental results show that this first attempt at packaging an array using BCPs is not as good as the simulation suggests. This is caused by the fact that the current assembly procedure requires that the whole array be heated up to 200°C for soldering. The thermal expansion coefficient mismatch of the copper and BeO layers makes the substrate bend toward to the front surface, or the side with BCP channels. This deformation of the substrate makes the solder layer at the center of the diode bar thicker. Also the average solder layer thickness is thicker than the ideal case. Solder layers always cause an extra thermal resistance because the thermal conductivity of the solder is lower than copper and BeO. Consequently, the temperature difference between the central emitters and the edge emitters on the same bar is higher than the simulation suggests. Moreover, because of the bending, the overall solder thickness for each single bar is also thicker in order to compensate the bending. The failed bar and emitters might also be related to improper soldering.

87
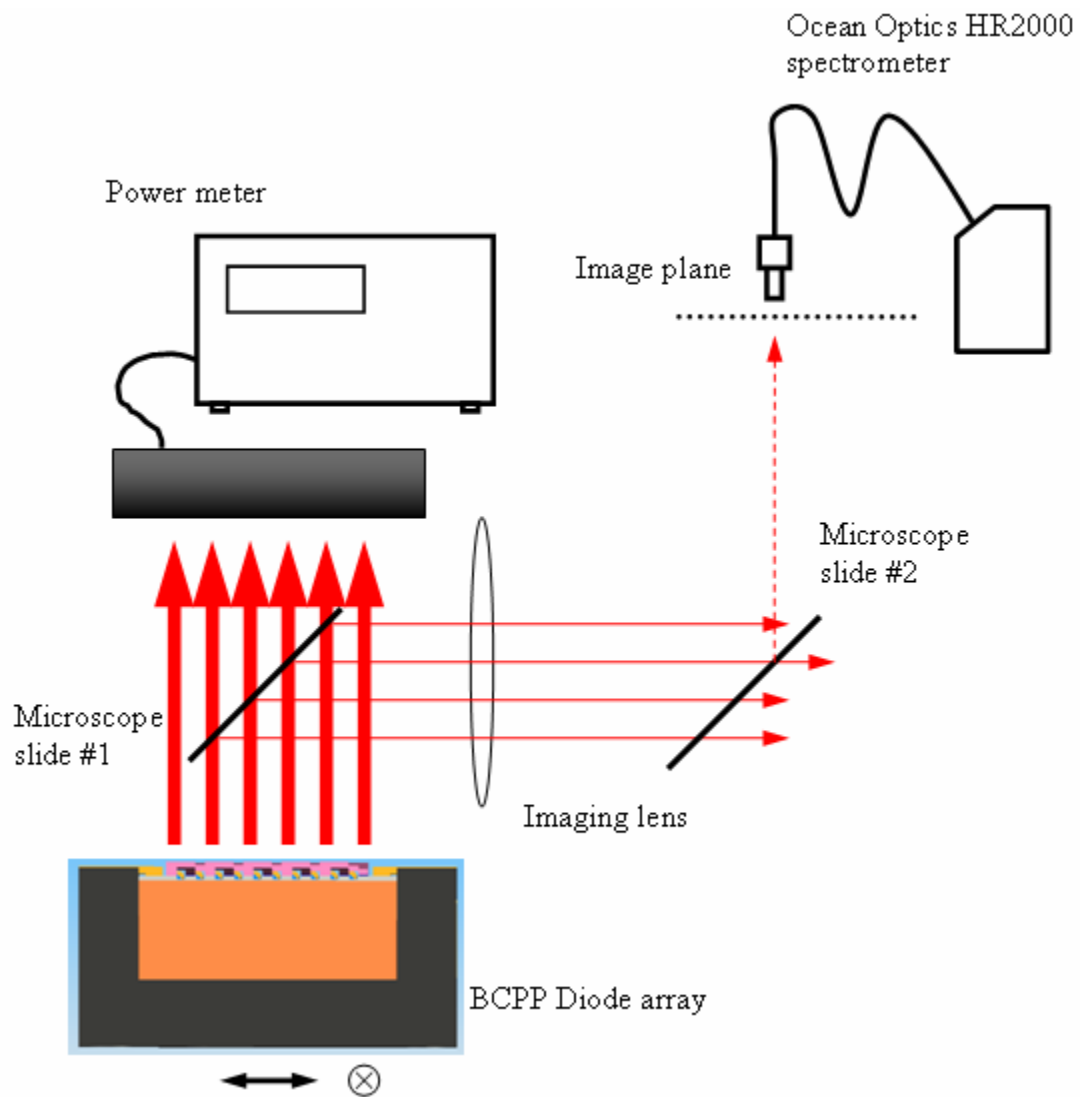
Figure 5.24: Experimental setup for measuring the output spectrum of each emitter
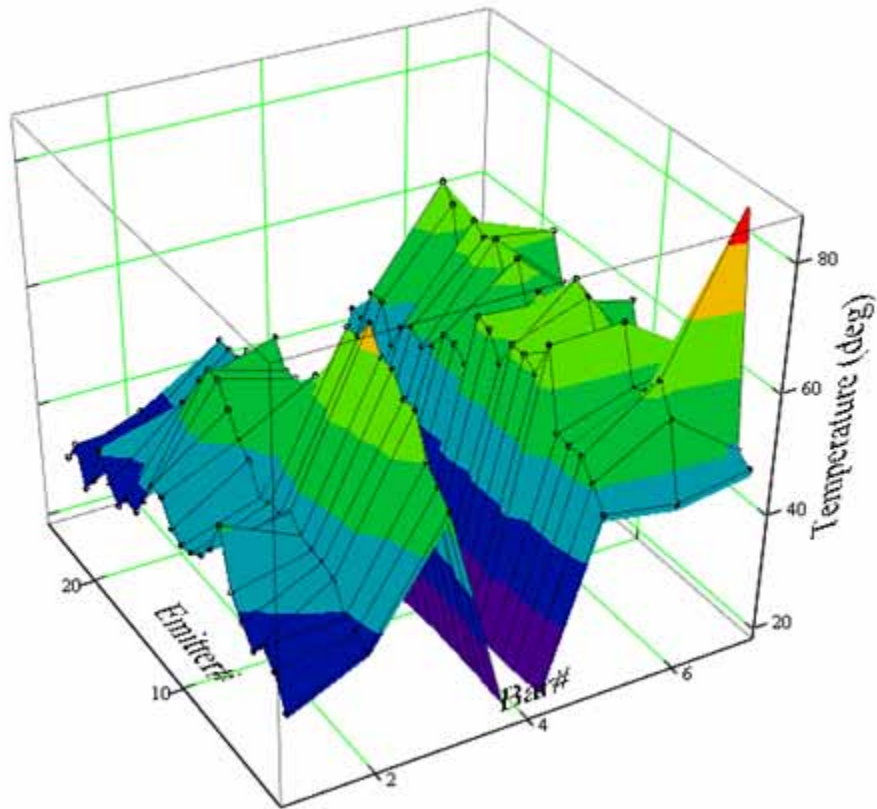
Figure 5.25: Measured temperature distribution of a BCPP diode laser array

5.9 Summary of BCPP

A better package design is essential for high power diode laser arrays. Optical, mechanical, thermal and electrical issues of the diode laser array packaging have been discussed thoroughly. Several designs of the beam control prism package have been proposed to achieve better cooling. Based on the BCPP design, a 10 bar diode array was built and tested. The experimental results show trend similar to the FEA results. However, because the thermal expansion coefficient mismatch induces deformation of the substrate, the overall solder thickness increases and the thermal resistance is higher.

Also, the thickness of the solder layer might not be uniform which makes the thermal

resistance uneven and consequently the temperature distribution is not uniform.

6. SLOW DIVERGENCE ANGLE CONTROL

The slow divergence axis is the width direction of the emitters. For an LT1200-40W diode bar, the emitter width is 150μm. The emission wavelength is 808 nm and the index of refraction of the diode laser is about 3. Because the design of the diode laser is a waveguide with two flat end surfaces the aperture is about 500 times of the emitting wavelength. Therefore, the slow divergence axis can sustain very high order transverse modes. Since a typical edge emitting diode laser is essentially a simple waveguide all the allowed transverse modes add up together. Also, the diode lasers have extremely high gain which makes ASE another contributor to the observed beam divergence angle. In reality, since the diode laser has such a high optical power, nonlinear effects such as self-focusing will induce filamentation and make the output non-uniform. Therefore, it's more reasonable to consider the slow divergence axis output as a simple line source rather than a Gaussian beam. Unfortunately, there is no simple geometric optics solution to image a line source into a point without losing power. Another problem is the emitter spacing or the fill factor. To increase the power from a diode laser bar manufacturers make wider and/or more emitters in the bar. Thus, the active areas can be relatively close to each other. The beams from different emitters will merge together in a very short distance. Once the beams mix together there is no easy way to separate beams again unless one re-images the diode bar. The main purpose for controlling the slow divergence axis of a diode bar is to make the light output a uniform line in a certain plane. Consequently, a cylindrical lens array is needed.

91

6.1 The micro optics array design for slow axis

We can use a positive micro lens to control the slow divergence axis. Figure 6.1 defines the geometric parameters along the length direction of a diode bar, the slow divergence axis direction.
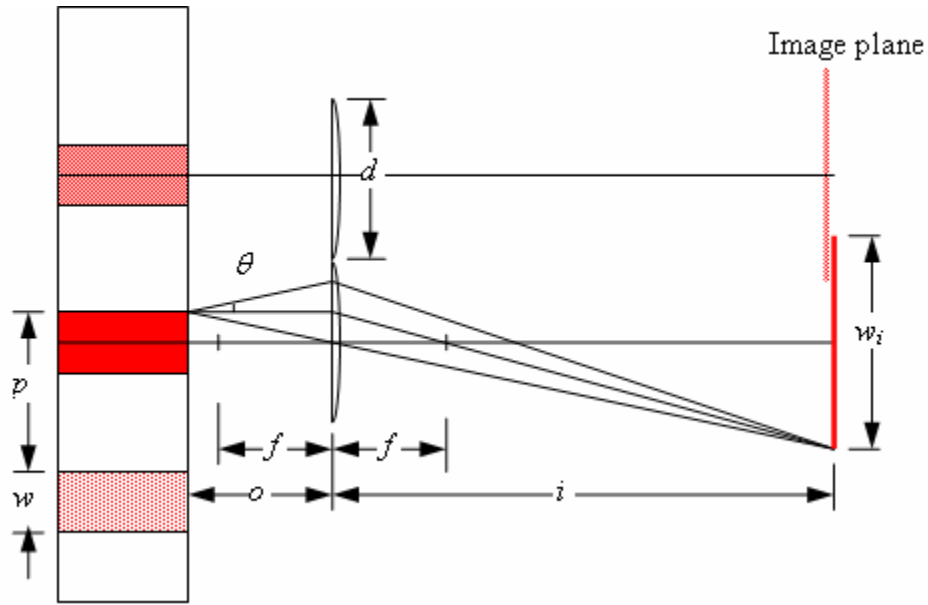
Figure 6.1: Parameters for slow divergence axis and micro optics

Even though the slow divergence angle is smaller, $\sim 10°$, than the fast axis divergence, the micro optics array has to be placed before the beams from different emitters mix. This requirement implies that the largest width of a single micro lens has to be smaller than the emitter spacing.

$$d \leq p \qquad\qquad (6.1)$$

We use the lens equation:

$$\frac{1}{o} + \frac{1}{i} = \frac{1}{f} = (n-1) \cdot \left[\frac{1}{R_1} - \frac{1}{R_2} + \frac{(n-1) \cdot t}{nR_1R_2} \right] \qquad (6.2)$$

where the magnification of the image is:

$$M = \frac{i}{o} = \frac{w_i}{w} \qquad (6.3)$$

In the following discussion and calculation, all the numbers are based on the LT-1200-40W diode bar with its specifications listed in Table 5.2. A 0.3 mm thick fused silica (index of refraction = 1.41) substrate for the micro lens array was considered in our calculations. The micro lens aperture size is limited by the emitter spacing p. Therefore, we consider d equal to the emitter spacing, 500 µm. Figure 6.2 shows a simple concept of a diffractive micro lens or a Fresnel lens and defines parameters for it.[17]
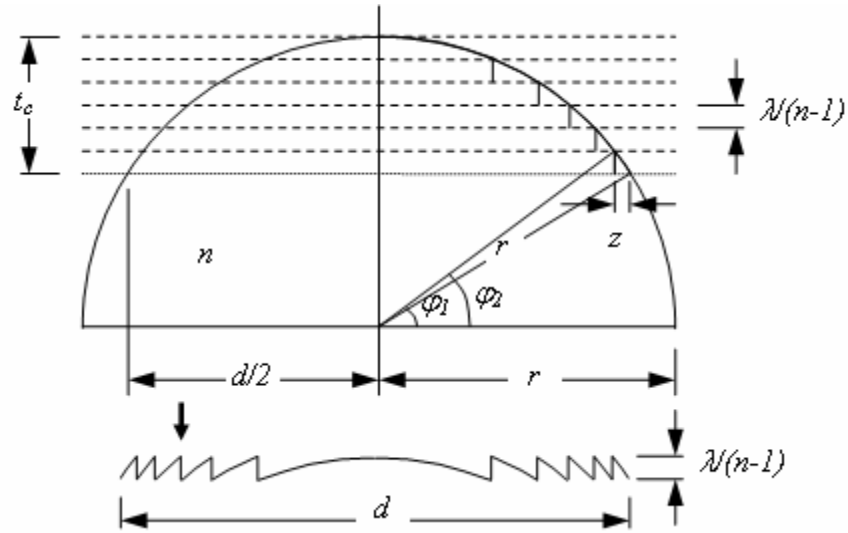
Figure 6.2: Parameters of a diffractive micro lens

Using simple geometry we can easily obtain the relationships between these parameters:

$$z = r \cdot (\cos \varphi_1 - \cos \varphi_2) \qquad (6.4)$$

93

$$\frac{\lambda}{n-1} = r \cdot \left(\sin \varphi_2 - \sin \varphi_1 \right) \qquad (6.5)$$

$$\frac{d}{2} = r \cdot \cos \varphi_1 \qquad (6.6)$$

$$t_c = r \cdot \left(1 - \sin \varphi_1 \right) \qquad (6.7)$$

The limitation of the micro lens is the smallest feature, about 1 μm, which the stepper available in our facility can make. In other words, for an eight level Fresnel lens, z is no smaller than 8 μm.

$$z \geq 8 \mu m \qquad (6.8)$$

Solving for z numerically, we obtain Figure 6.3 which shows the outermost feature size of the micro lens versus the radius of the curvature of the Fresnel lens. The minimum radius of curvature of the micro lens is 1028 μm. The corresponding focal length is 2508 μm.
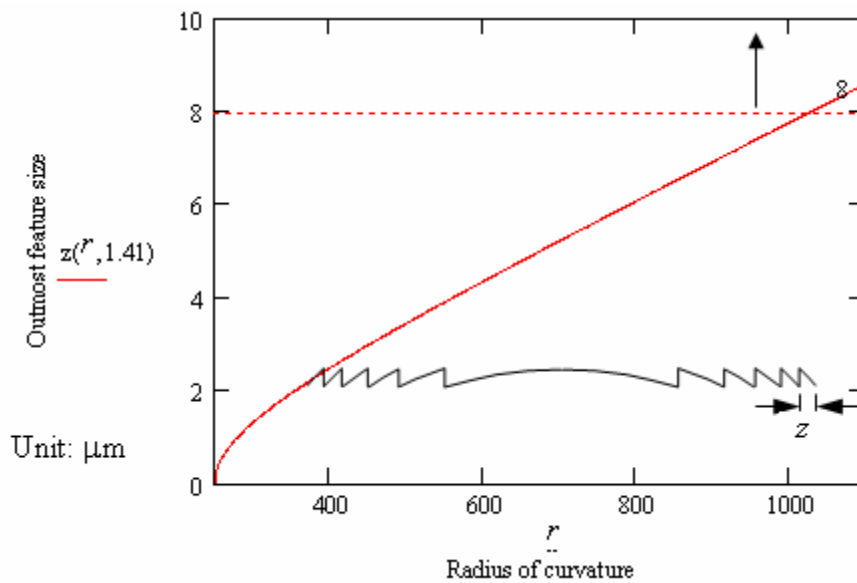
Figure 6.3: Edge feature size with respect to the radius of curvature r of micro lens

The micro optics design aims to make the NA or the acceptance angle large so that the lens accepts most of the light. In other words, a short focal length and/or large aperture micro lens has to be made. The focal length of a plano-convex lens is proportional to the radius of curvature of the convex surface as shown in Equation (6.2). We assume the output beam in the slow divergence axis direction is also a Gaussian distribution. Therefore, if we choose the acceptance angle of the micro lens to be twice the FWHM beam divergence angle, it will accept 98% of the output power.

The emitter slow divergence angle is ~ 10°; therefore, a reasonable half acceptance angle of the micro lens is ~ 10°. Figure 6.4 shows the half acceptance angle of a micro lens when the light source is at the focal point and the image is at infinity. The maximum radius of curvature giving half acceptance angle = 10° is 597 μm. The corresponding focal length is 1417 μm. However, placing the emitters in the focal plane will only form a real image at infinity. In order to form a real image at a finite distance, the object distance *o* has to be larger than the focal length *f*. The larger the object distance is, the smaller the acceptance angle will be.
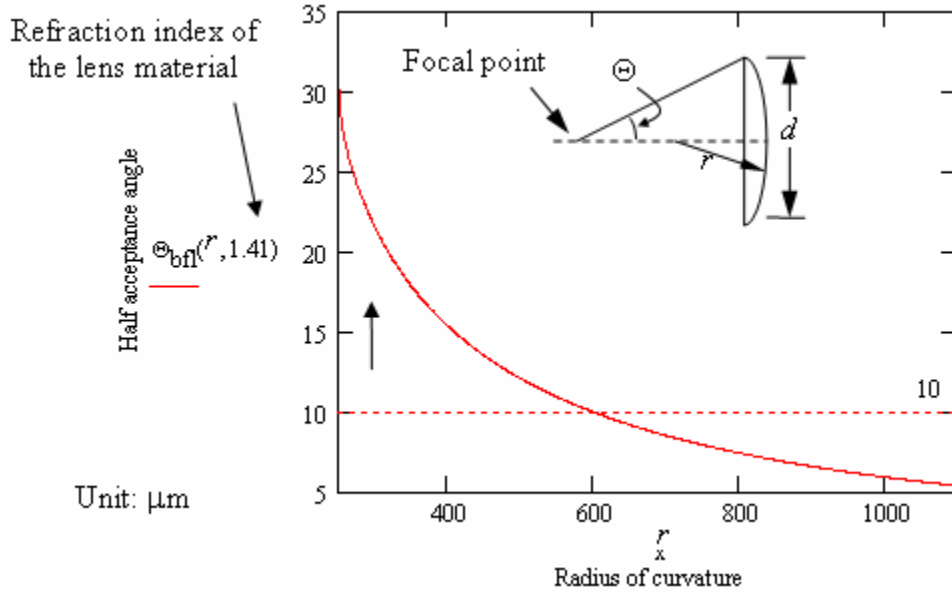
Figure 6.4: The half acceptance angle Θ with respect to the back focal length of a micro lens versus the radius of curvature, *r*

We also can define the overlap parameter:

$$\alpha = \frac{w_i}{p} \qquad (6.9)$$

For perfect imaging of the emitter, a line source as shown in Figure 6.1, this overlap parameter should be 1 to produce a uniform line in the image plane. If the emitter is Gaussian or has some other beam distribution, the overlap parameter can be larger than 1.

From Equation (6.2), (6.3) and (6.9) we obtain:

$$o = f \cdot (\frac{w}{p} + 1) \qquad (6.10)$$

In this equation, the object distance, *o*, should include the thickness of the micro lens substrate.

96

Figure 6.4 shows the half acceptance angle versus the radius of curvature of the lens producing an image at infinity. However, the goal is to find a finite image distance with the overlap parameter = 1. Under this condition, we can obtain the half acceptance angle versus lens radius of curvature as shown in Figure 6.5. To achieve a 10° half acceptance angle, the micro lens radius of curvature has to be larger than 313 μm. However, from Figure 6.3 we know that the limitation due to fabrication makes the minimum radius of curvature no smaller than 1028 μm.
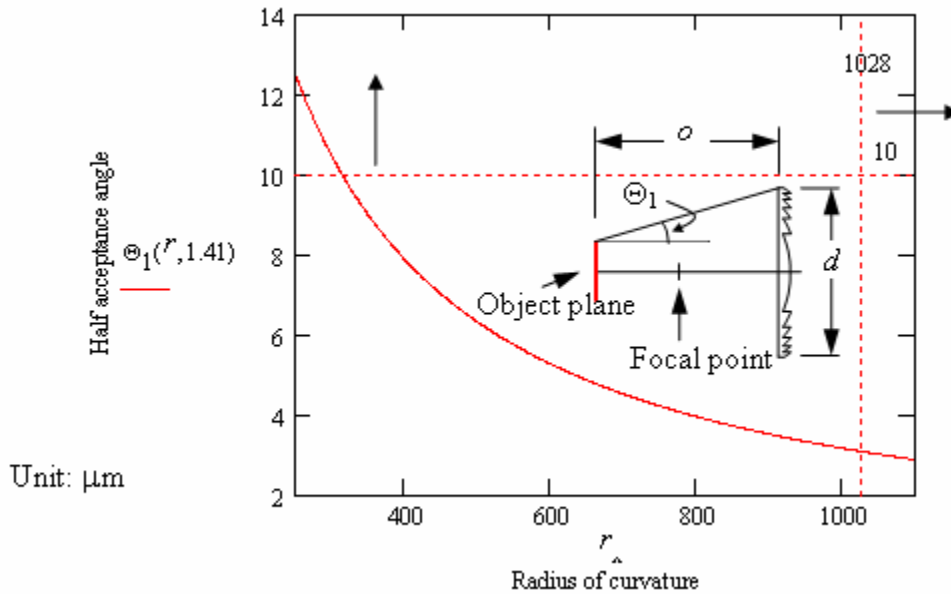
Figure 6.5: Half acceptance angle of the micro optics with overlap parameter = 1

The preceding discussion shows that it is not possible to make a single 8 level Fresnel lens to collimate the light without throwing away a considerable amount of power. Using a 4 level micro lens can increase the half acceptance angle to 5.6°, but its

diffraction efficiency is lower. Also, a 4 level micro lens will have less diffraction efficiency compared to an 8 level micro lens implying that less power will be delivered.

A typical substrate thickness is about 1 mm but a 0.3 mm thick substrate is also available. We must keep in mind that the object distance should include the thickness of the micro lens substrate and all other objects between the emitter and the micro lens. For example, the current BCP has a physical length of 1 mm. When designing the micro lens this extra optical path must be considered.

Using a material with a different index of refraction to make the Fresnel micro lens does change its feature size and the minimum radius of curvature. However, the minimum focal length of the micro lens is almost independent with its index of refraction. Figure 6.6 shows the resulted values of the minimum focal lengths for different index of refraction materials versus the micro lens aperture size. The focal lengths difference between materials having n = 1.4 and n = 1.6 is less than 2%. Consequently, there is no significant advantage using a higher index of refraction material to make the Fresnel micro lens.
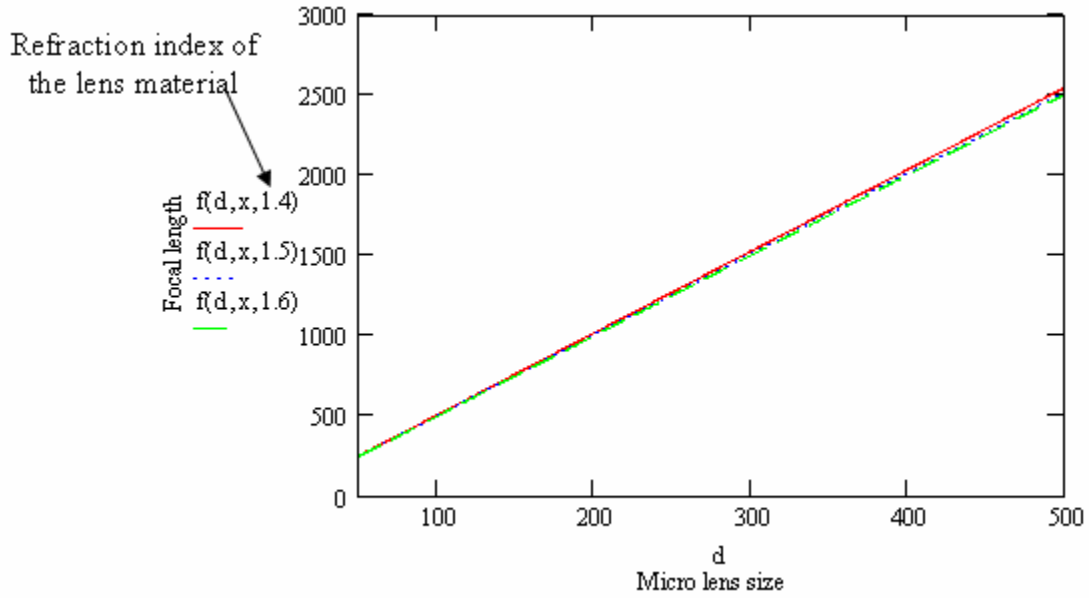
Figure 6.6: Focal lengths of the minimum radius of curvature micro lenses made from materials with different indices of refraction

6.2 ASAP simulation of micro cylindrical lens array

Figure 6.7 shows the ASAP simulation of a Lasertel LT-1400-40W bar with a 0.5 mm radius folded-ball BCP and different focal length cylindrical lens arrays. The folded ball BCP is placed 80 μm in front of the diode bar as shown in Figure 5.10. The image plane is 4 mm away from the exit surface of the BCP. Figure 6.7 (a) shows the simulation result without any micro lens array. Figure 6.7 (b) shows result of the micro cylindrical array with radius of curvature of 1028 μm, the minimum radius of curvature that can be made in our facility and (c) is the result when the radius of curvature of the micro lens is 391 μm. The emitters are exactly at the focal plane of the micro lens array. Fig. 6.7 (d) has micro lens radius of curvature 313 μm which is the focal length that

satisfies the overlap parameter = 1. Fig, 6.7 (e) is the micro cylindrical lens array that we

made which has radius of curvature 798 µm but the aperture size is 250 µm.
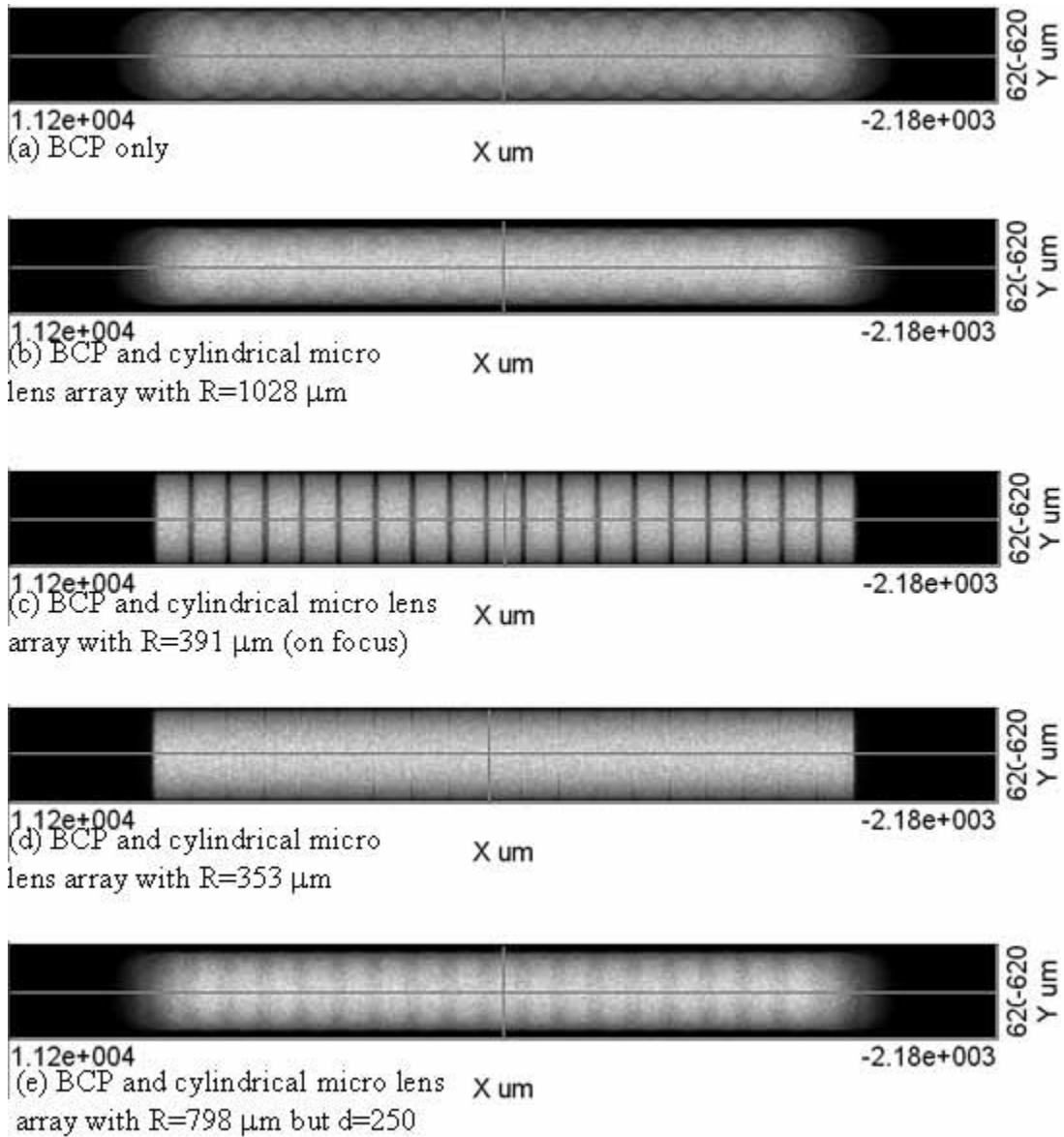
Figure 6.7: ASAP simulation results of the output beam of a LT-1300-40W diode bar using micro lens arrays with different focal lengths

From these results, it is clear that a manufacturable 8 level Fresnel micro cylindrical

lens array has only a very limited ability to improve the output beam quality. We can

conclude that a single Fresnel micro lens does not have enough optical power to control the slow divergence axis of a high power diode laser bar.

6.3 Micro cylindrical lens array combining with a cylindrical lens

Even if a micro lens array with small radius of curvature can be made, the short working distance is still not preferable. For most applications, the working distance should be few cm away from the diode laser array or even further. Therefore, another cylindrical lens might be needed to extend the working distance. This extra cylindrical lens provides an extra degree of freedom which makes the large radius of curvature micro lens feasible to control the slow divergence angle. Figure 6.8 shows the basic concept of this set up and defines the parameters. The main concept is using the micro cylindrical lens array to form virtual images of the emitters which become the virtual objects of the cylindrical lens. Therefore, this is called the virtual image set up in the following paragraphs.
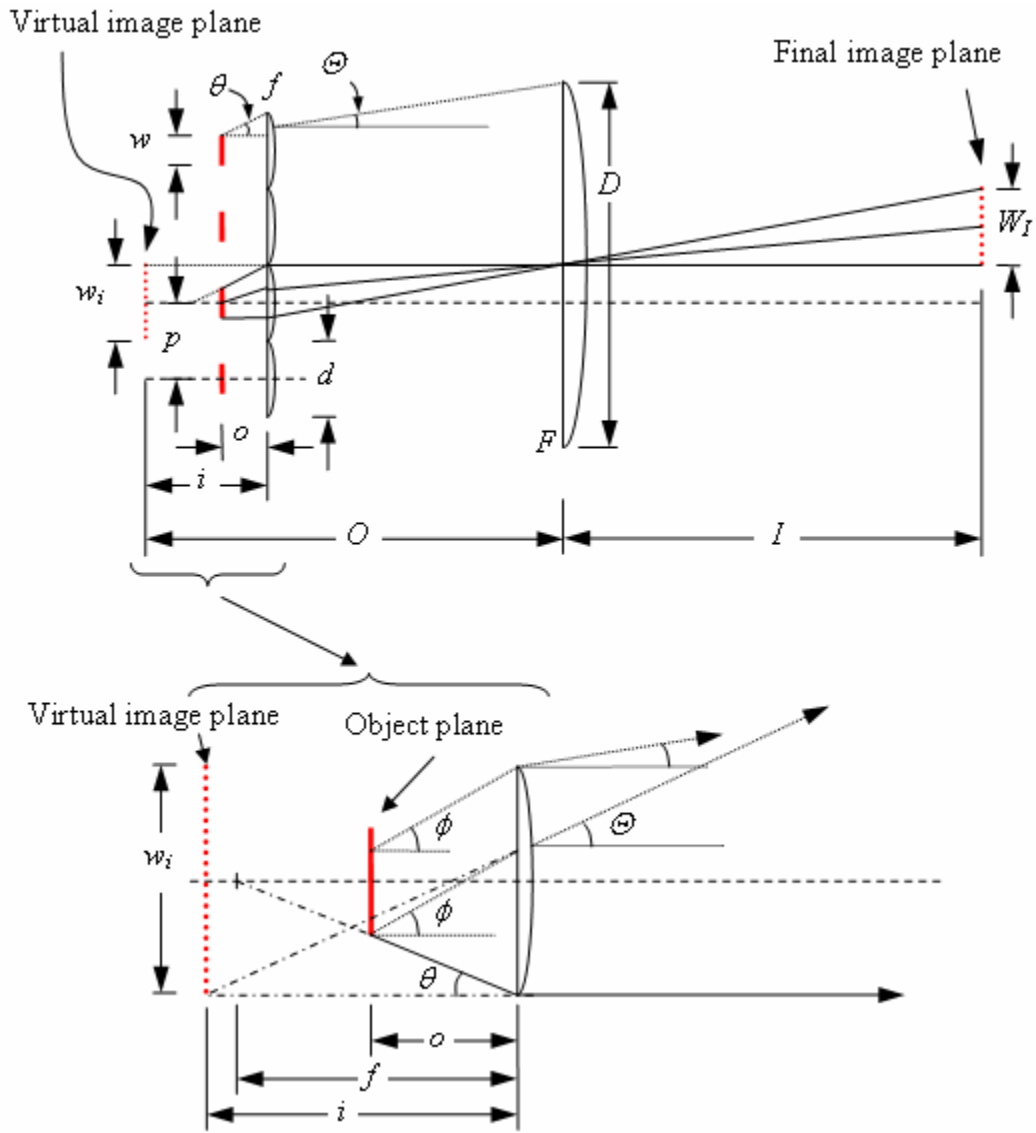
Figure 6.8: Parameters of micro cylindrical lens and cylindrical lens system

For a given focal length f of the micro cylindrical array several equations can be written down:

$$\frac{i}{o} = -m = -\frac{w_i}{w} \tag{6.11}$$

$$\frac{I}{O} = M = \frac{W_I}{w_i} \qquad (6.12)$$

$$\theta = \tan^{-1} \frac{d - w}{2 \cdot o} \qquad (6.13)$$

M and m are the magnifications of the cylindrical lens and the micro cylindrical lens. Because the micro lens forms a virtual image, the magnification, m is positive. However, the cylindrical lens forms a real image so that M is negative. A similar overlap parameter is defined in Eq. (6.9). By choosing the overlap parameter equal to 1, a continuous linear virtual image can be obtained.

Combining Eqs. (6.2) and (6.11) yields

$$o = \frac{w_i - w}{w_i} \cdot f \qquad (6.14)$$

Figure 6.9 shows the half acceptance angle versus the micro lens size of this setup. Comparing this with the previous single micro lens design in Figure 6.5, a larger half acceptance angle can be achieved by this virtual image set up when the overlap parameter = 1.
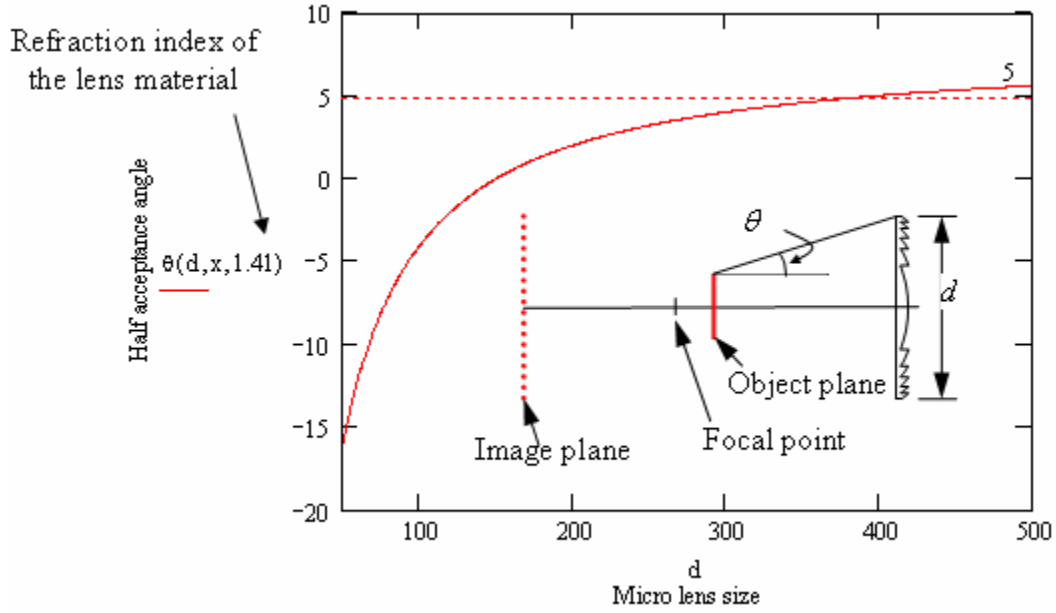
Figure 6.9: Half acceptance angle of the virtual image setup

The total power delivered to the final image plane is determined by the acceptance angle or the focal length and the aperture size of the micro cylindrical lens. From simple ray tracing we know:

$$\Theta = \tan^{-1}\left(\frac{1}{2} \cdot \frac{w - 2 \cdot \tan\phi \cdot (o + f)}{f} \right) \qquad (6.15)$$

If the overlap parameter is 1 the virtual image size will be identical to the emitter pitch. To achieve the largest acceptance angle the micro cylindrical lens size has to be equal to the emitter pitch as well. From previous calculation the minimum focal length of a micro cylindrical lens with the lens size of 500 μm is 2544 μm. The object position o is 1781 μm. If the half divergence angle ϕ is 10°, we can obtain $\Theta = 4.7°$ from Eq. (6.15). Therefore, we can decide the size of the cylindrical lens.

$$D = N \cdot p + 2 \cdot (O - i) \cdot \tan \Theta \qquad (6.16)$$

N is the number of emitters on a single bar. O, the object distance for the cylindrical lens, is chosen based on the working distance and focal length of the cylindrical lens.

Assuming the final emitter image has the same size as the virtual emitter image, or the magnification of the cylindrical lens is -1, Eq. (6.12) shows that I is equal to O and equal to twice of its focal length F. If we choose the image distance $I = 5$ cm, the cylindrical lens will have a focal length of 2.5 cm. The size of this cylindrical lens, D, is at least 1.68 cm which is equivalent to an f/1.48 cylindrical lens. Such a cylindrical lens is commercially available.

6.4 Summary of slow divergence angle control

Previous discussions show that using a single 8 level Fresnel micro cylindrical lens array is not able to control the slow divergence angle without throwing away most of the diode output power. Also the working distance is relatively short which is not practical. However, using the virtual image setup we can control and utilize more output power of the diode array and have a reasonable long working distance.

7. PUMP CAVITY DESIGN FOR DIODE LASER ARRAY PUMPED ROD SHAPED LASERS

Diode lasers are ideal light sources for pumping solid state lasers but most diode arrays are packed in diode array stacks. However, the rod shaped solid state laser is still the most commonly used gain medium. To efficiently use a stack diode laser array to pump a rod shaped laser we designed and tested easily manufacturable pump cavities that enable high pumping efficiency and uniform gain distribution. In this chapter we present the properties of two pump cavity designs with diffusive interior surfaces. Our goal was to optimize gain uniformity in a rod shape gain medium by utilizing such cavities to deliver the pump light.

7.1 Definition of non-uniformity

A simple definition of non-uniformity is proposed. This definition is an easy approach to evaluate the non-uniformity of any quantity distributed with axial symmetry. Figure 7.1 gives a simple idea of the non-uniformity. Figure 7.1 (a) shows the most basic parameters to describe non-uniformity. They are the average value, standard deviation across the whole area and the center of mass position. A smaller standard deviation implies a more uniform distribution. The center of mass gives a very rough idea about the asymmetry of the pattern. Figure 7.1 (b) shows the radial uniformity. The whole pattern is divided into several concentric rings. We take the mean value and the standard deviation of each ring as the radial non-uniformity. In the similar manner, we can define

the angular non-uniformity by dividing the whole pattern into several wedge shaped sectors and then take their average values and standard deviations to represent the non-uniformity.

I_{ave} Mean value
σ_{all} Standard deviation
(x_m, y_m) Center of mass

(a) Fundamental quantities

Radial section
$I(r)$ Mean value
$\sigma(r)$ Standard deviation

Angular section
$I(\theta)$ Mean value
$\sigma(\theta)$ Standard deviation

(b) Radial non-uniformity

(c) Angular non-uniformity
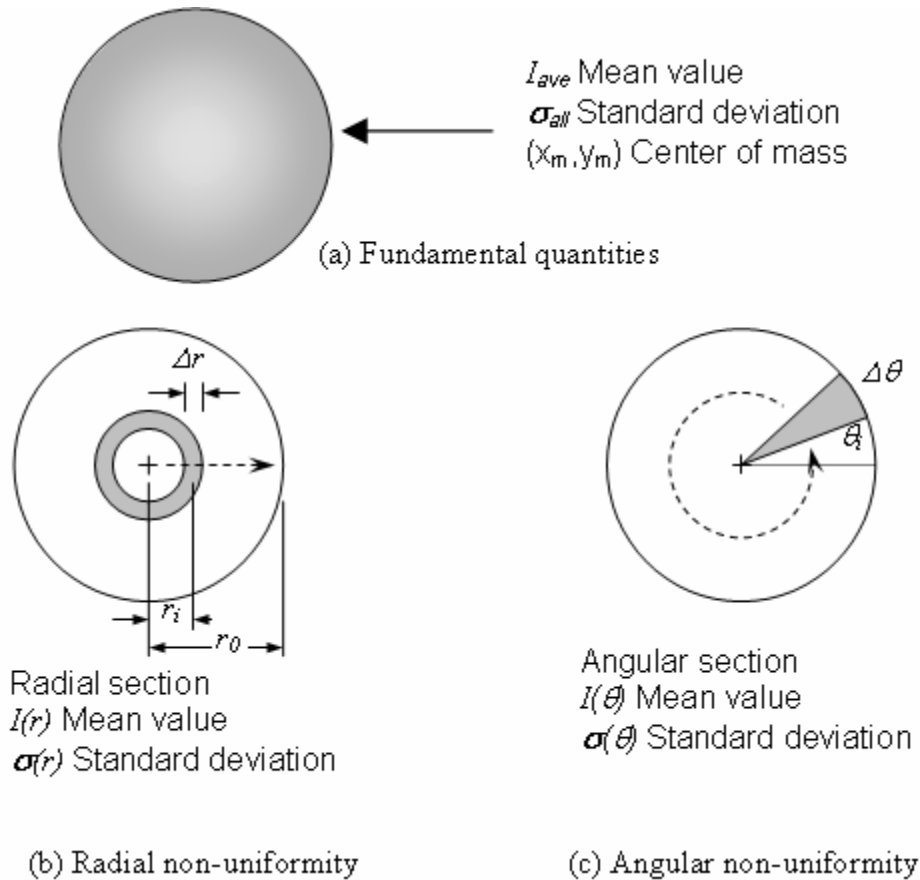
Figure 7.1: Different definitions of non-uniformity

By using the radial non-uniformity and angular non-uniformity, we can easily figure out the distribution of the quantity we measure and turn it into four uniformity plots. Figure 7.2 shows an example of such non-uniformity plots. Figure 7.2 (a) is an example of gain distribution. Plot (b) shows the radial distribution of the gain. The solid line represents the average values in different rings. The dash lines represent the range of

average value plus and minus one standard deviation. The dotted lines give the maximum and minimum values of the quantities in each ring. Figure 7.2 (c) shows the similar feature as (b) but it presents the angular uniformity. Figure 7.2 (d) is the radial standard deviation and (e) is the angular standard deviation.

The red arrows indicate the higher gain distribution areas which is located at the edge of the rod and at angle close to 90°. They relate to the red arrows in Figure 7.2 (e). The green arrows indicate the lower gain areas in the two wider areas around 190° and -50° which also relates to (e). Also, because of the higher and lower gain areas are located closer to the edge, the edge has a larger standard deviation value as shown in Figure 7.2 (d).
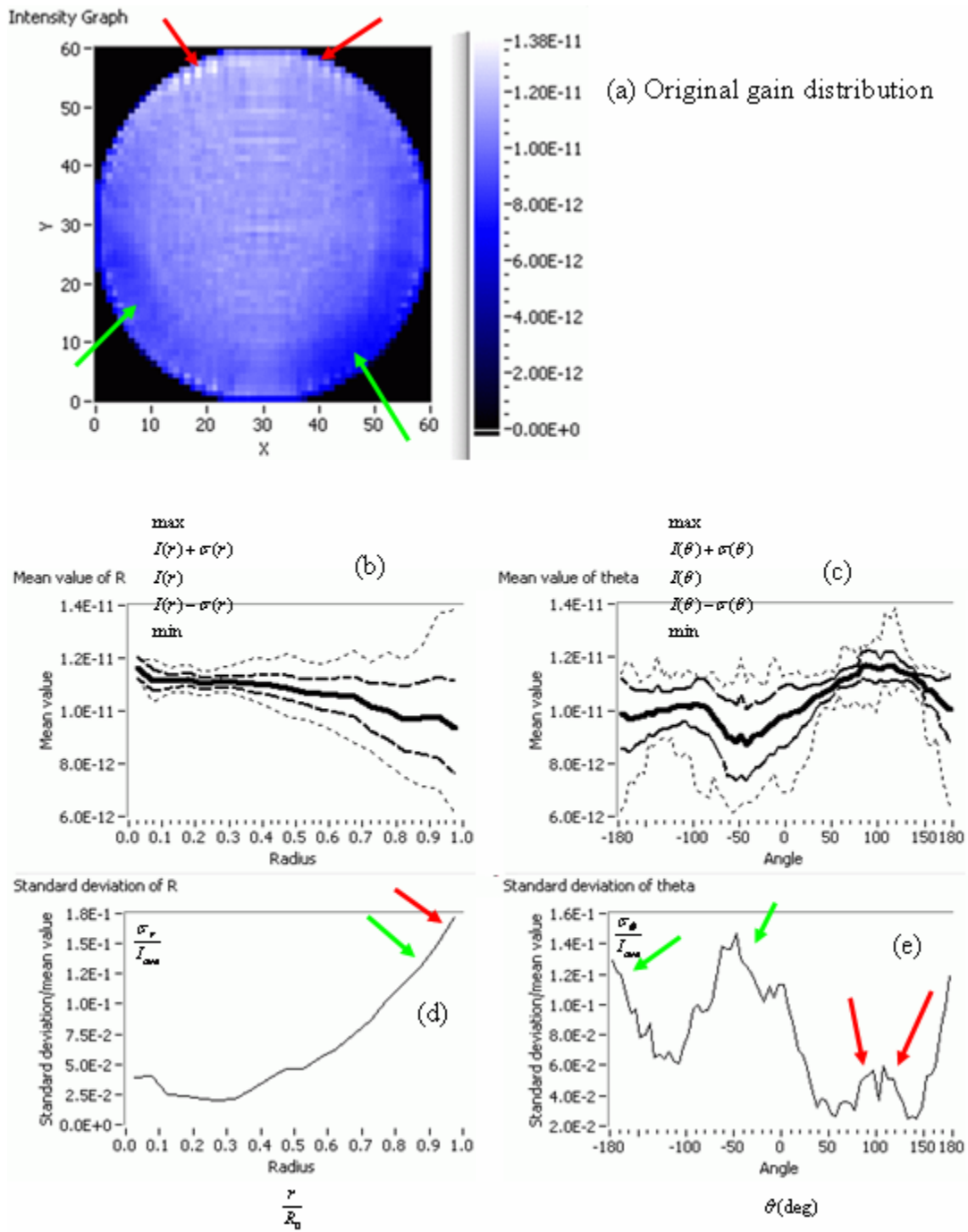
Figure 7.2: Non-uniformity plots

7.2 Measurement of the fluorescence pattern

The fluorescent pattern inside the gain media represents the gain distribution. Figure 7.3 shows the configuration of the experiment. In simple term, we just consider that the rod has an index of refraction of 1. For the real case, we have to consider Snell's law, but essentially the concept is the same. A lens is used to project the rod image to a CCD camera. From the geometric optics we know the rays from point A form a real image at point A' then the rays keep on going and smear out to a much wider area between point B' and point D' at the image plane. From another point of view, if the aperture size is infinity large, the signal we obtain at point p' on the CCD contains all the information from every single element in the rod as long as the ray passes through point p. Therefore, using a large aperture is not a proper way to measure the florescence pattern. If we limit the aperture size to a point on the optical axis, only the ray comes from point A to point p can be projected to point p'. In other words, the signal we measure at point p' is the integration of the fluorescence of all points along line Ap in the rod with their rays traveling in the Ap direction. From simple geometry again, if we use a longer focal length lens, the distance between point B and point p will be smaller implying that the angle between line Ap and the optical axis is smaller. If we use a lens with a long enough focal length which makes the separation between B' and p' less than the pixel size on the CCD, we can consider the image on the CCD is the integration of the fluorescence distribution along the rod axis. When making a laser resonator the laser light propagates along the rod axis. Therefore, using a long focal length and small aperture lens to get the fluorescence along the rod axis is a simple, practical and reasonable way to observe the gain distribution.
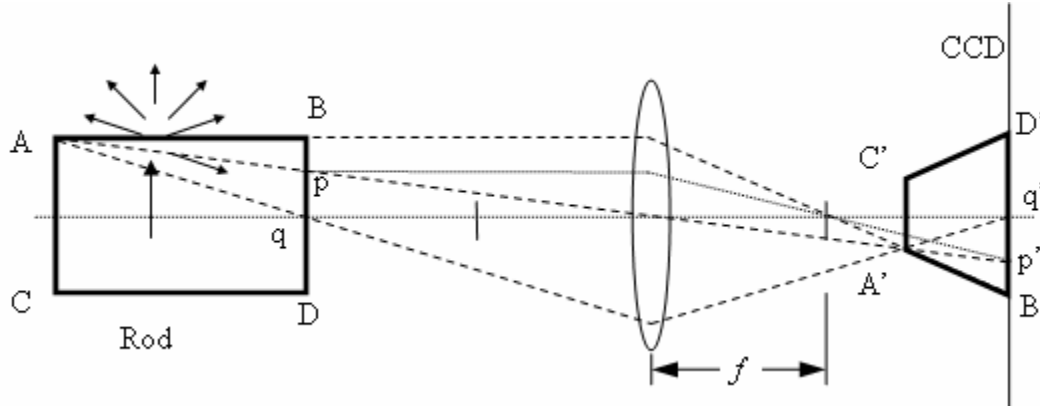
Figure 7.3: Simple schematic of imaging fluorescent pattern of rod gain media

Another phenomenon which should be noticed is called "bat-ears". We observed that the very edge of the rod image is a bright ring. This is due to the fact that the ground barrel surface scatters fluorescence light coming from all the points in the rod and re-directs that into arbitrary directions. Therefore, the barrel is brighter and from the experimental set up we know the barrel image will be project to the position along line B'p' on the image plane. Therefore, a bright ring is projected on the CCD. This ring gives the appearance of a "bat-ear" as in the Batman© cartoon when the fluorescence intensity is plotted across a diameter. The pattern is very helpful to the experimenter because by observing its symmetry one can align the rod to be on axis with the detection system.

7.3 Cavity designs and simulations

Solid state laser pump cavity designs are based mostly on using flash lamp pump sources.[18] Diode laser arrays can not be considered a linear light source as are flash

lamps. Hence, the design concepts for pump cavities are different from flash lamp pump cavities.

We propose two new cavity designs for pumping rods with diode laser arrays. They are the "D" cavity and the rooftop cavity which were chosen because they are easy to manufacture by simple milling machine operations. Figure 7.4 shows the simple sketch of the "D" and the rooftop cavities. Ideally, the D cavity has most of the light enter the rod from the back side. The rooftop cavity has a unique off-center rod position. A rooftop pump cavity was proposed in 1981 for an optical pumped dye laser cell.[19,20] If the pump light is collimated and illuminates from the bottom of the cavity, the rooftop cavity provides a uniform pumping from all four directions as shown in the Figure 7.4 (b).

(a) "D" cavity
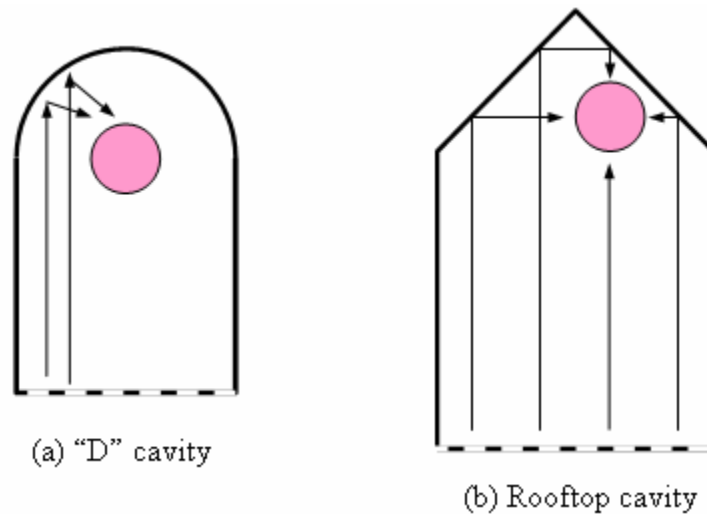
(b) Rooftop cavity

Figure 7.4: "D" cavity and rooftop cavity and their design concepts

For computational studies we assumed the cavity was made of Spectralon with Lambertian diffusive surfaces having reflectivity of 98.5%. The laser rod was 3 mm in diameter with a ground or frosted cylindrical surface. The diode array for pumping was

powered by the spray-cooled array of four Coherent 808 nm B1-40C-19-30-A bars described in Chapter 3.

A typical diode array has a finite linewidth about 2.5 nm full width at half maximum (FWHM) or even wider. Therefore, the absorbed pump power distribution is determined by the pump spectral contains corresponding to different absorption coefficients in the gain medium. Assuming no gain saturation, the pattern of the absorbed pump power distribution is the linear combination of the single wavelength pump patterns. The total absorption efficiency is the contribution of the absorption efficiency of each individual wavelength as shown in Equation (7.1) where $P(\lambda)$ is the power output at wavelength λ and $\eta(\lambda)$ is the absorption efficiency at wavelength λ.

$$\eta = \frac{\int_\lambda \eta(\lambda) \cdot P(\lambda) d\lambda}{\int_\lambda P(\lambda) d\lambda} \tag{7.1}$$

Figure 7.5 shows the Nd:YAG absorption spectrum and the typical diode laser output spectrum centered at 807 nm, 808.5 nm and 810 nm. Figure 7.6 shows the Nd, Cr:GSGG absorption spectrum and the same diode laser output spectrum. The peak absorption of the Nd, Cr:GSGG is 1.5 nm different from the Nd:YAG and the peak absorption coefficient is slightly higher. Also, there is another absorption peak at 804.4 nm.
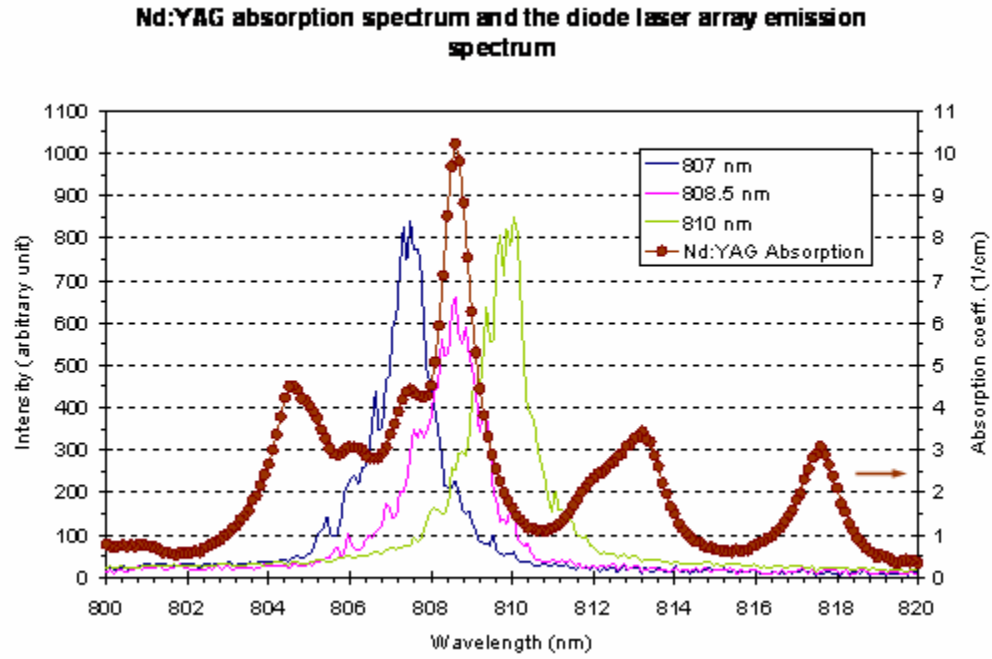
Figure 7.5: Nd:YAG absorption spectrum and the diode laser array output spectrum
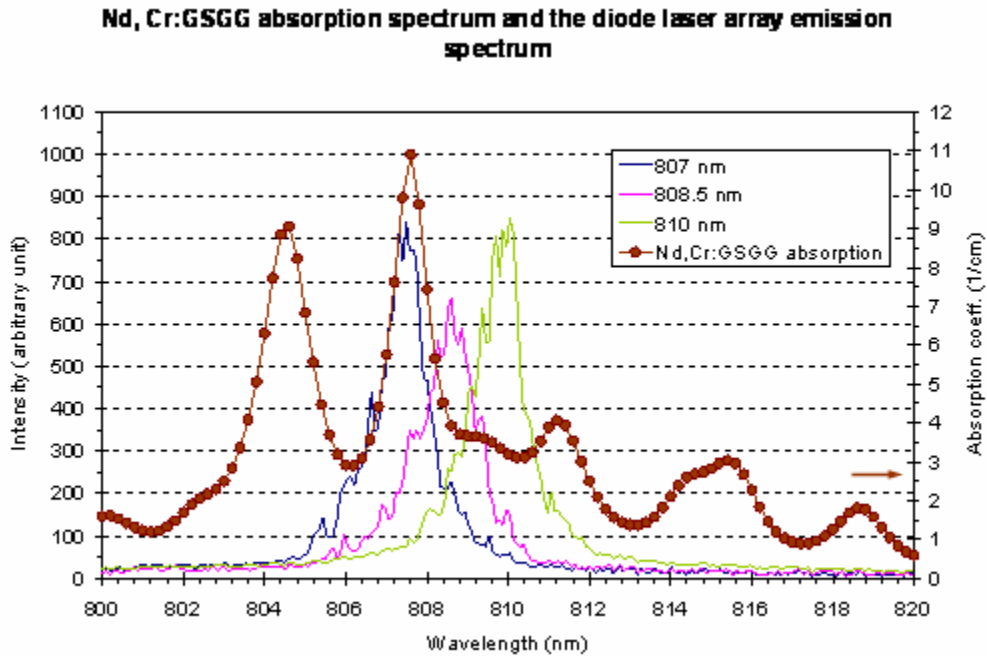
Figure 7.6: Nd,Cr.:GSGG absorption spectrum with both Nd, Cr doping density $2\times10^{20}/cm^3$

All of the simulations performed used the multi-wavelength approach. We calculated the absorption pattern every 4 nm. By linearly combining the absorption patterns we obtained the multi-wavelength absorption pattern corresponding more closely to the actual pattern in a real pumped laser rod. The following simulations considered that the pump light was centered at 808.5 nm.

In one case, the simplest, a free standing rod without a pump cavity was considered with the rod located 15 mm away from the diode array. The simulation result and the calculated non-uniformity are shown in Figure 7.7. The largest radial non-uniformity is almost 62% and the largest angular non-uniformity is about 40%. The overall non-

uniformity is about 36%. Without a pump cavity, not only is the absorption efficiency low, but the uniformity is poor.
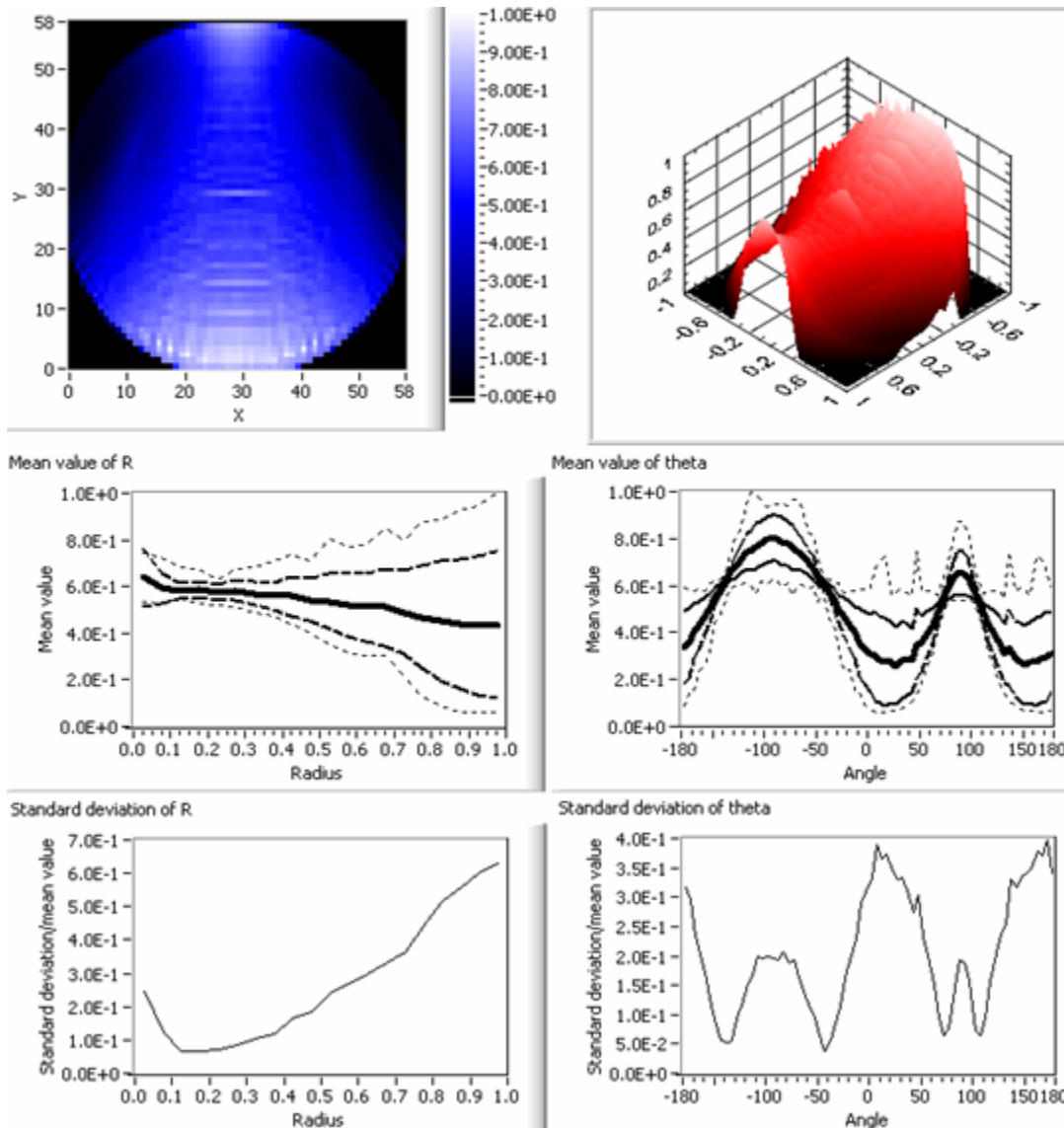
Figure 7.7: Distribution and non-uniformity of the Nd:YAG absorbed pump power distribution pattern in a free standing rod with pump light centered at 808.5 nm

We also performed calculations for a cusp pump cavity and an elliptical pump cavity such as have been used for flash lamp pumped rod lasers. In both of these cavity

designs, the internal surface is assumed to be polished, and the surface reflectivity is 100%. Figure 7.8 shows the cusp pump cavity and elliptical pump cavity simulation results. The largest radial non-uniformity for the cusp is above 40% and the largest angular non-uniformity is about 22%. Its overall non-uniformity is about 25%. In the elliptical pump cavity case, the radial non-uniformity is about 40%, the largest radial non-uniformity is more than 50% and the overall non-uniformity is 41%. Therefore, we concluded that the polished elliptical pump cavity was not suitable for our purpose. The cusp cavity design gave better result, but the uniformity was still not good enough.
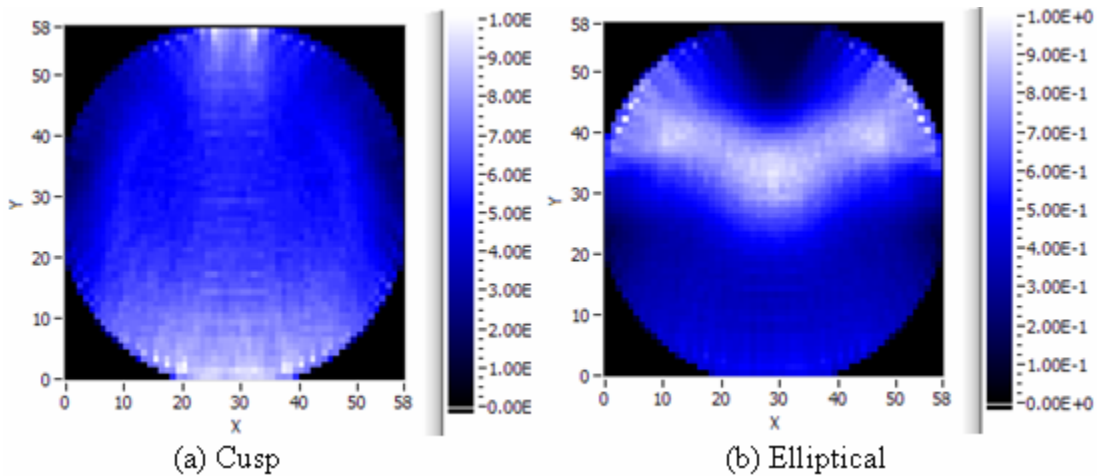
(a) Cusp   (b) Elliptical

Figure 7.8: The cusp and the elliptical pump cavity simulation results for the distribution of absorbed pump power

The "D" pump cavity interior was taken as Lambertian, the "D" was chosen as a half cylinder with radius of 5.7 mm and the distance from the rod center to the diode bars was 13 mm. Figure 7.9 shows the simulation and calculation results for the "D" cavity. The maximum radial non-uniformity is 15% and the maximum angular non-uniformity is 23%. The overall non-uniformity is 18%.
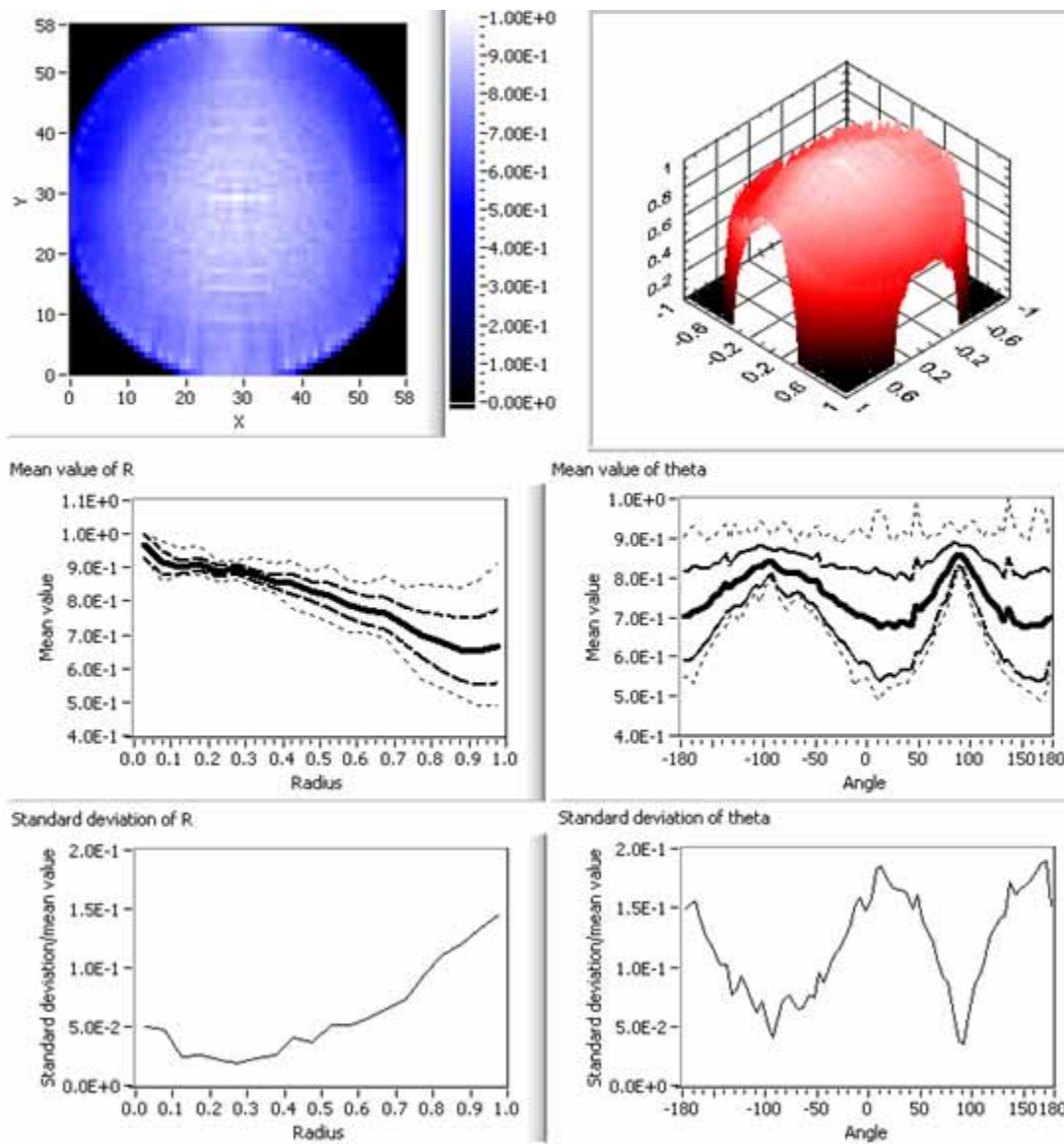
Figure 7.9: Simulation and the calculation results for the Nd:YAG absorbed pump power distribution in a "D" cavity with pump light centered at 808.5 nm

The rooftop cavity interior was also assumed to be Lambertian. Because of the off center feature, the cavity width has to be exactly 4 times the rod diameter and the roof angle is 90°. The distance between the rod center and the diode array plane was taken as 13 mm. Figure 7.10 shows the simulation and calculation result of the rooftop pump

118

cavity. The maximum radial non-uniformity is about 18% located at the very edge. The maximum angular non-uniformity is about 15%, but the overall non-uniformity is only 11%.
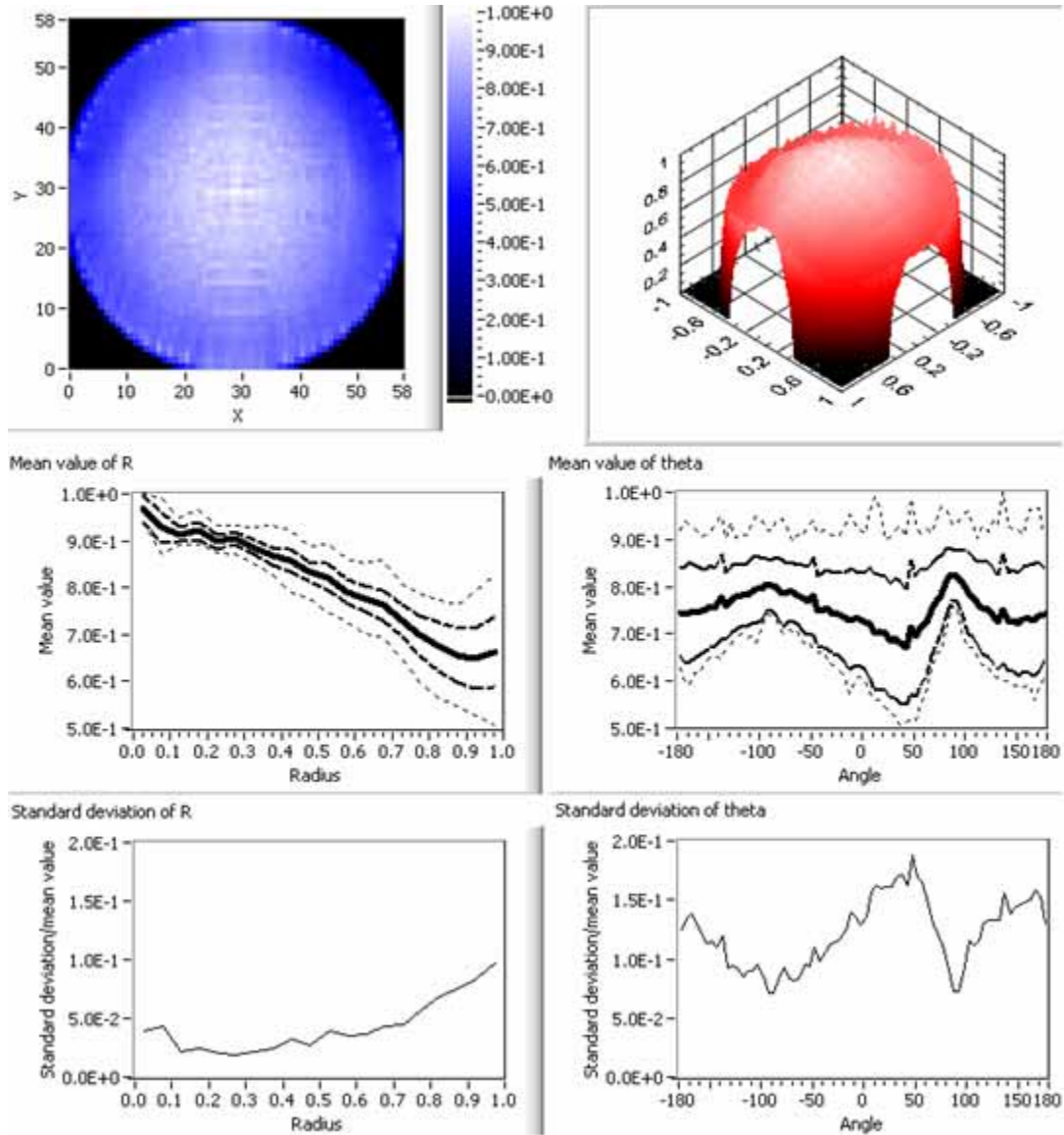
Figure 7.10: Simulation and the calculation results for the Nd:YAG absorbed pump power distribution in a rooftop cavity with pump light centered at 808.5 nm

Both the "D" and the rooftop cavities show great improvements in uniformity over the free standing rod or even the cusp cavity design.

119

We also completed a thorough and systematic study of the rooftop cavity. Figure 7.11 shows the absorption efficiency and the overall non-uniformity plotted as functions of the cavity surface reflectivity. The navy blue solid line indicates the rod absorption efficiency, the pink solid line represents the cavity absorption efficiency and the red solid line is the light leakage from the edge of the rod to external space. The brown line with circular dots shows the overall non-uniformity over the whole rod. This figure shows that the surface reflectivity does influence the absorption efficiency strongly. The rays bounce many times in the pump cavity. Also, the overall non-uniformity only changes slightly when the surface reflectivity decreases.
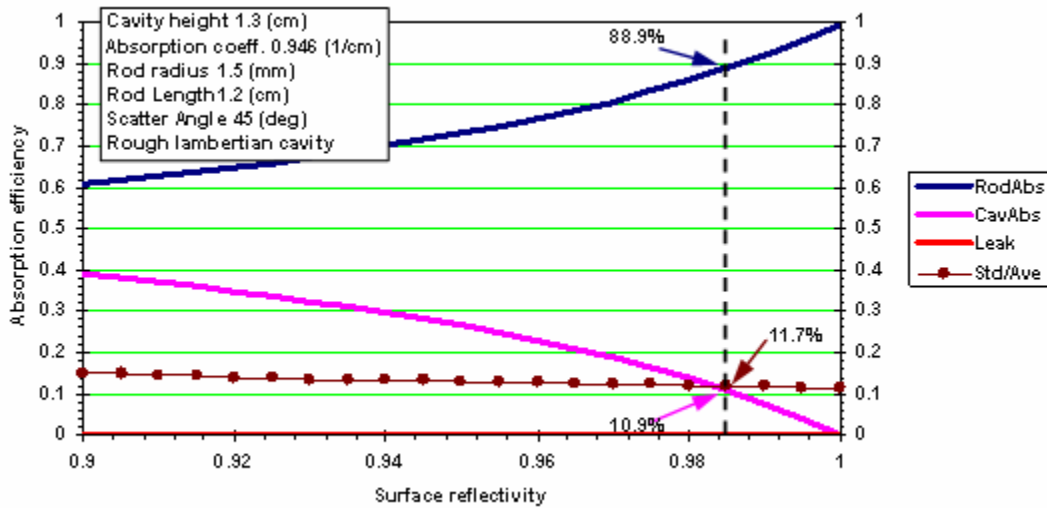
Figure 7.11: Absorption efficiency and gain uniformity versus cavity surface reflectivity

Figure 7.12 shows the influence of the distance between the diode array and the rod center. When the distance is longer, the rod has a more uniform absorption pattern but the absorption efficiency decreases. When the distance exceeds 1.5 cm, extra distance no

longer results in improved uniformity. Consequently, 1.5 cm is probably the optimized array-to-rod difference for such rods and array dimensions as we consider. Also the lower absorption efficiency for the larger distances implies that the multiple bounces of the rays trapped in the Lambertian pump cavity reduce the absorption efficiency.
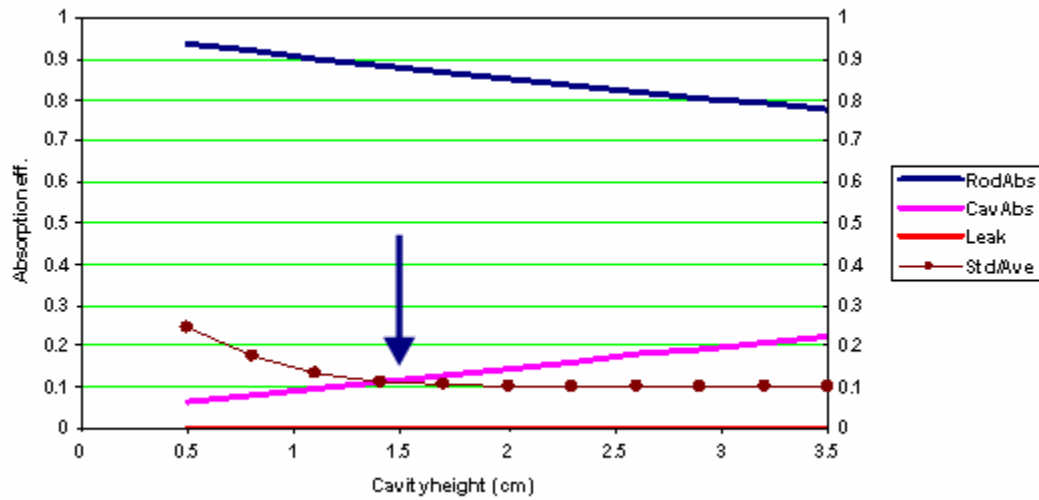
Figure 7.12: The absorption efficiency and the overall non-uniformity versus the cavity height or the distance between diode array and the rod center

Figure 7.13: shows that the rod surface roughness doesn't influence the absorption efficiency. A smoother rod surface causes a less uniform absorption pattern because of the lens effect of the rod surface. However, when the scattering angle exceeds 45°, the overall non-uniformity becomes independent of the scattering angle.
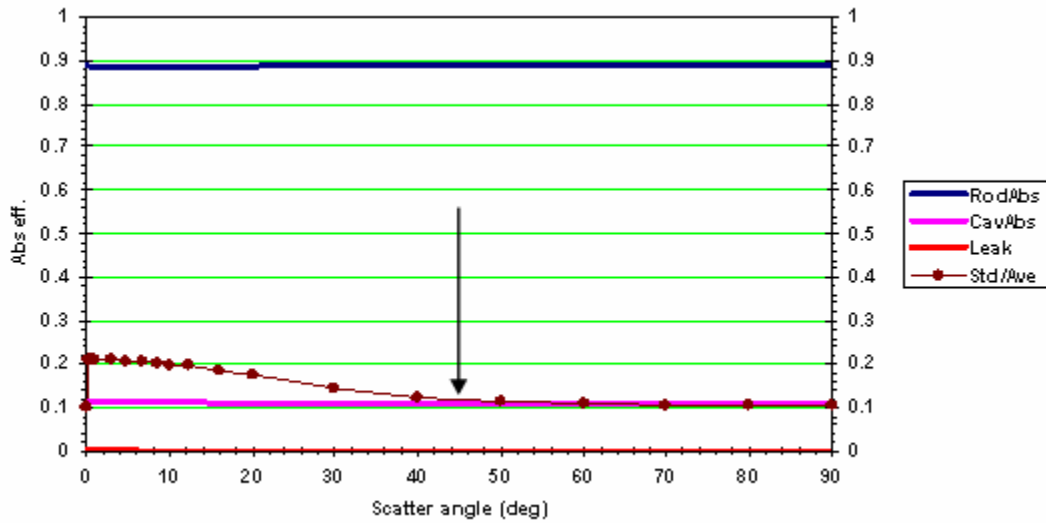
Figure 7.13: The absorption efficiency and the overall non-uniformity versus the rod surface scattering angle

Figure 7.14 shows the absorption efficiency and the overall non-uniformity versus the absorption coefficient of the rod. The absorption coefficient can be written in a normalized form. By multiplying the absorption coefficient and the radius we obtained the unitless αR absorption coefficient as shown in Figure 7.15. This normalized absorption coefficient makes possible to utilize the results of Figure 7.15 for a rod with different dopant concentration and/or radius. When $\alpha R = 1.5$, the overall non-uniformity has a minimum value.

Figure 7.16 shows the ASAP simulation of the absorption pattern in rods with different absorption coefficients. When the absorption coefficient is small, only a small fraction of the light is absorbed. Therefore, the absorption distribution is flat and the standard deviation is small as shown in Fig. 7.16 (a). When the absorption coefficient is increased, because of the symmetry, central part of the rod will have more incident light density at the center of the rod. Therefore, the center has increased absorption density as

in Fig. 7.16 (b). However, when the absorption coefficient becomes still higher Beer's law tells us that the edge will absorb more light and the pattern smooth out as shown in Fig. 7.16 (d). Eventually, with much higher absorption coefficient pump light is absorbed at the edge of the rod. The resulting gain distribution is shown in Fig. 7.16 (e).
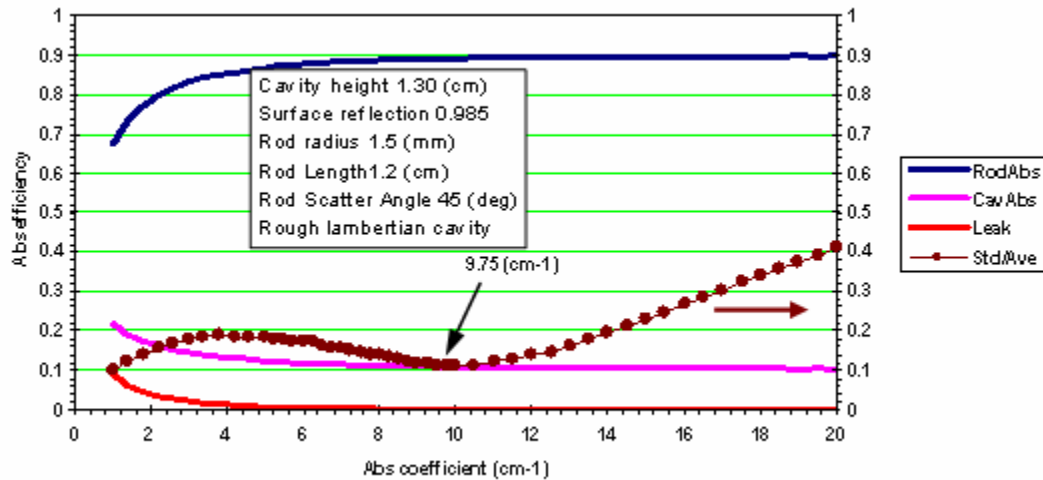
Figure 7.14: The absorption efficiency and the overall non-uniformity versus the absorption coefficient of the laser rod
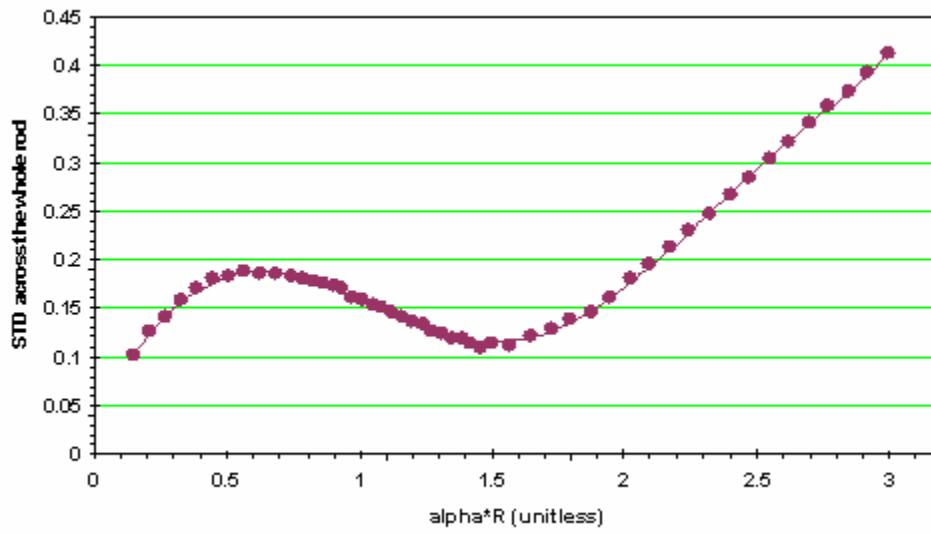
Figure 7.15: The standard deviation or the gain uniformity versus normalized absorption coefficient

(a) $\alpha = 1\ \mathrm{cm}^{-1}$

(b) $\alpha = 4\ \mathrm{cm}^{-1}$

(c) $\alpha = 8\ \mathrm{cm}^{-1}$

(d) $\alpha = 10\ \mathrm{cm}^{-1}$

(e) $\alpha = 16\ \mathrm{cm}^{-1}$
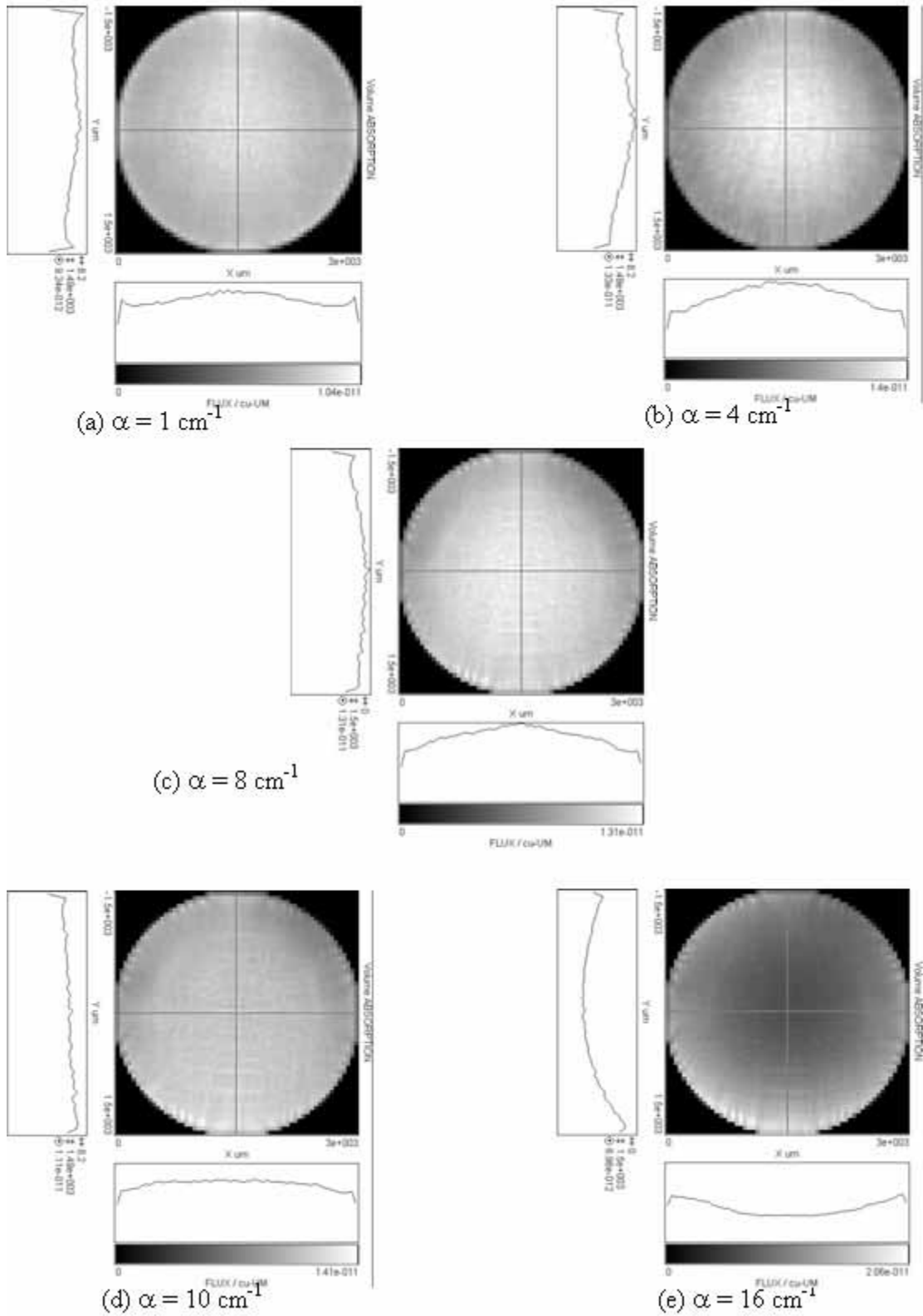
Figure 7.16: Absorption pattern for different absorption coefficients by using rooftop pump cavity

125

7.4 Experimental results

The fluorescence pattern inside the gain media represents the gain distribution and the absorbed pump power distribution. Therefore, we measured the fluorescence pattern to determine the gain distribution. Our experimental set up is shown in Figure 7.17. A small aperture size and long focal length imaging lens was used to form the final image on a CCD camera to obtain the correct fluorescent pattern.[21] The diode array was set at about 808 nm and the fluorescent output wavelength was about 1 μm; consequently, we used a RG830 filter to block the pump light and transmit the fluorescence. Correct alignment was achieved by adjusting the system until an axially symmetric image was obtained.

The diode bars were aligned parallel to the rod axis. In other words, the rod axis was perpendicular to the fast divergence axis of the emitters.
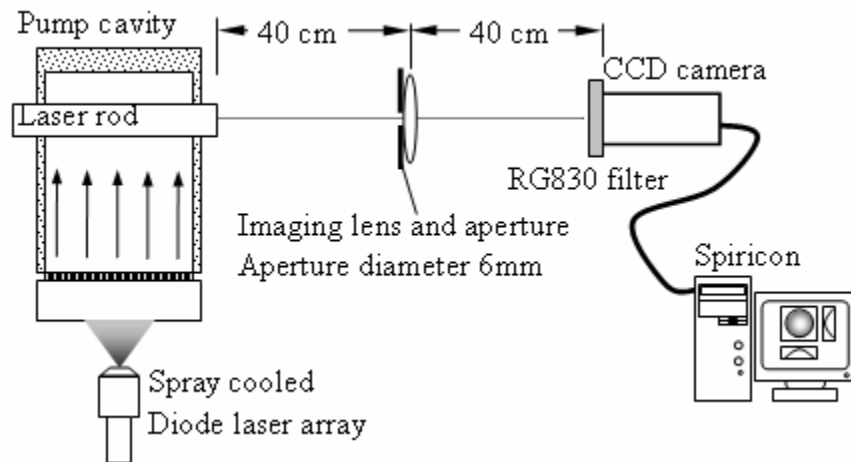
Figure 7.17: The experimental set up for measuring the fluorescent pattern from laser rods in the "D" and rooftop pump cavities.

Three pump cavities were made; one was a Spectralon "D" cavity, another was a spectralon rooftop cavity and the third was a sand blasted and gold-plated aluminum "D" cavity. Two sets of end plates were made; the first set of end plates placed the rod at the center of the cavity and the other set was displaced by 1.5 mm to the side which is exactly the radius of the rod.

A free standing laser rod was pumped to confirm the simulation result. Its fluorescent pattern and the calculation results are shown in Figure 7.18. The maximum radial non-uniformity is 33% and the maximum angular non-uniformity is 22%. The overall non-uniformity is also 22%. In this picture, the edge ring or what we called the "bat-ears" is obvious. There are two areas is this picture on the upper left and right with lower fluorescence or lower gain as the green arrows indicate. We call these regions the "pig ears". Comparing this experimental result with the simulation in Figure 7.7 (b) shows that the major difference is that the absorption at the side of the rod farther from the array is higher. Because the pump light enters from the bottom of the rod, these rays are scattered by the lower half of the rod. Even though the surface is rough we still can consider the rays to be "focused" by the curved surface. Most of the pump light has lower absorption coefficients than the peak absorption coefficient in our simulation so that the light penetrates deeper into the rod and is "focused" to the back of the rod. Even though the individual ray carries less energy the focusing effect increases the energy density. As a result, higher absorption is observed at the side of the rod furthest from the array. This implies that a good cavity design has to increase the light illumination from the side of the cavity farther from the diode array. Our "D" and rooftop cavities design seek to achieve this objective
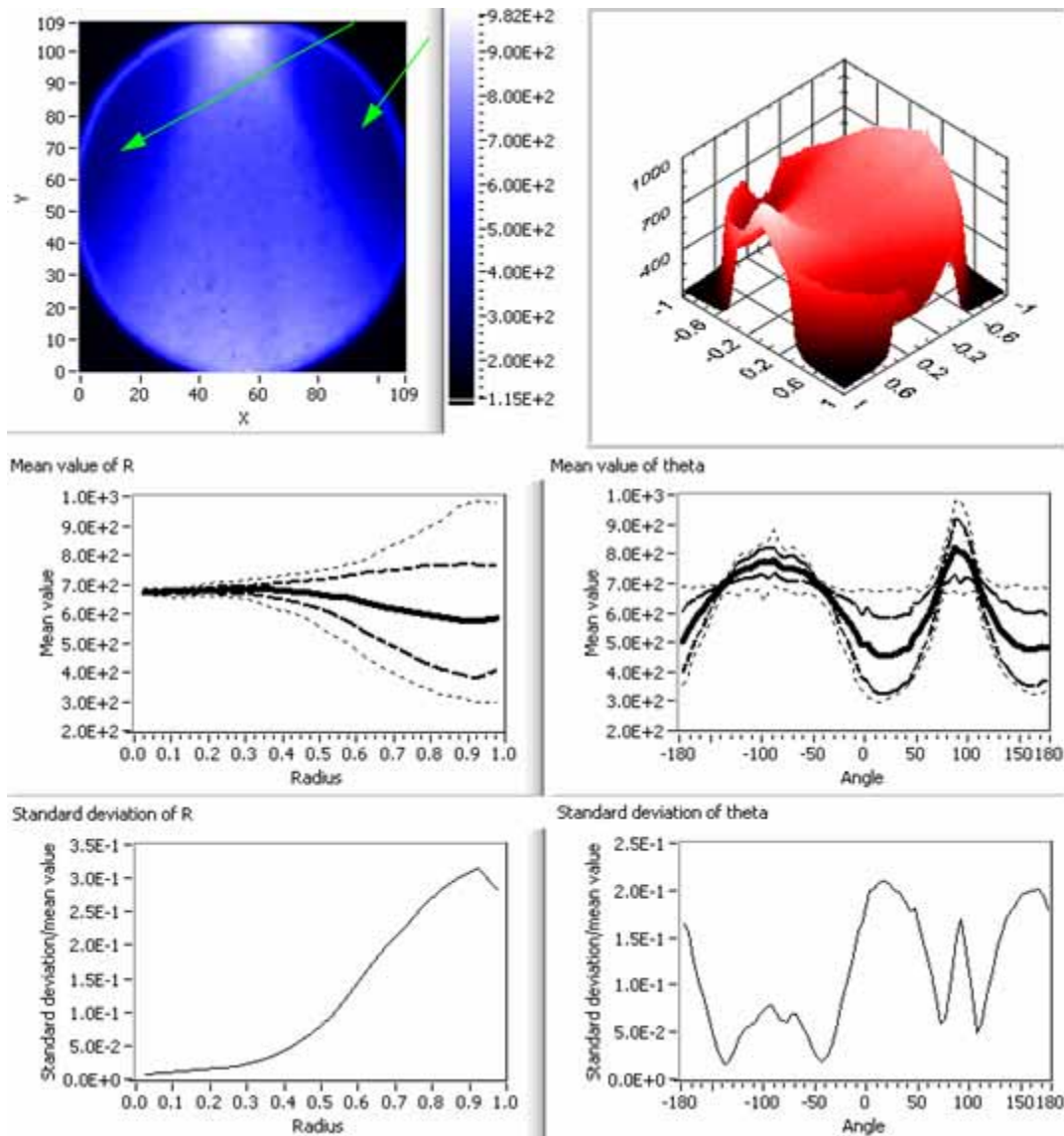
Figure 7.18: Measured free standing Nd:YAG rod fluorescent pattern

Figure 7.19 shows measured and calculated results for the "D" cavity. The maximum radial non-uniformity is about 12% and the angular non-uniformity is less than 12%. The overall non-uniformity is no more than 10.6%. Figure 7.20 shows the rooftop cavity results. The maximum radial non-uniformity is about 8%. The angular non-uniformity is less than 12% and the overall non-uniformity is 9.4%. The "bat ears" were observed in all the measured results. At the first glance we can see that all four pictures

show the "pig ears", but compared with the free standing rod, the uniformity along the pump direction is significantly improved by using a pump cavity.
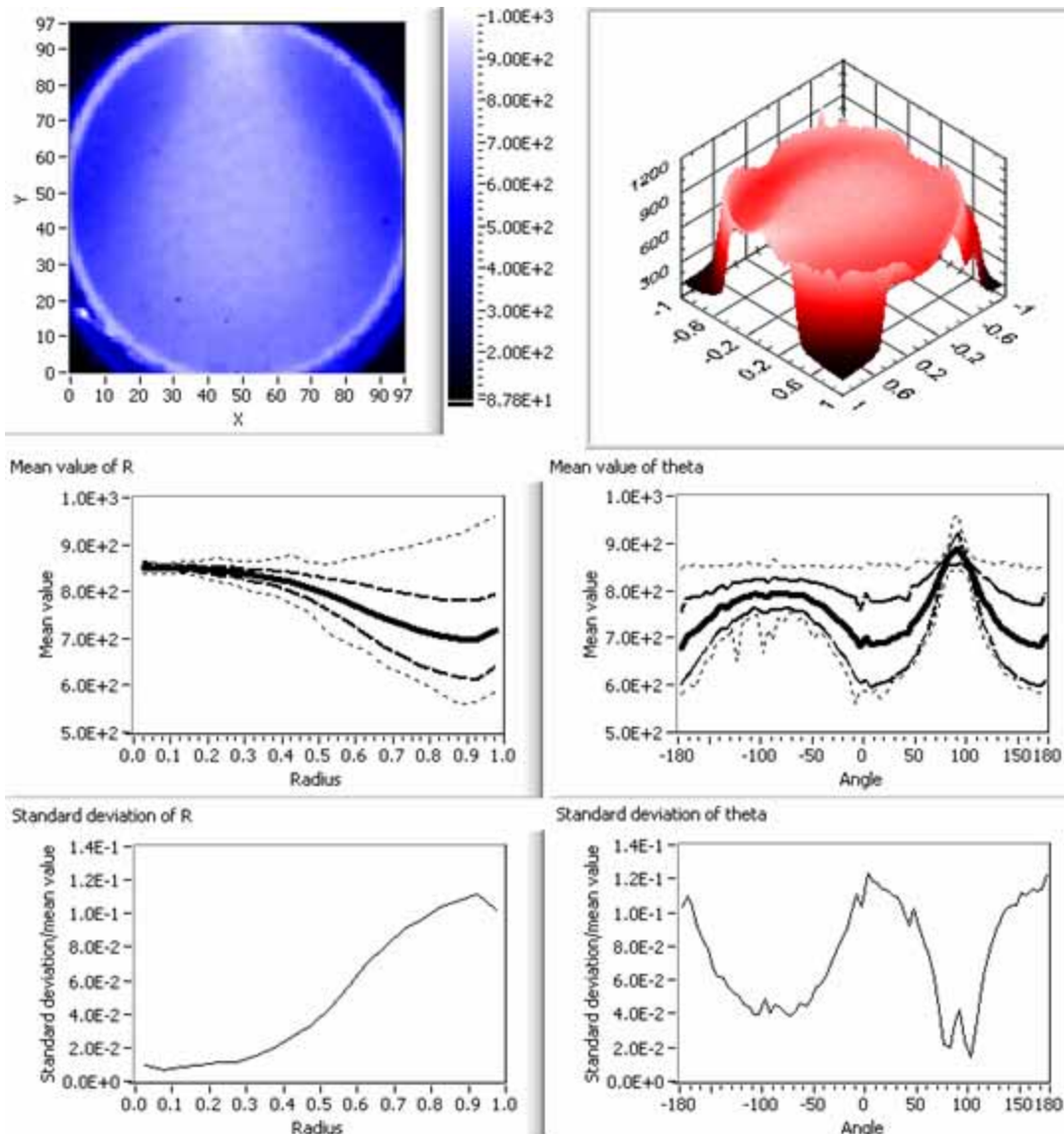
Figure 7.19: Measured Nd:YAG fluorescent pattern in the D cavity
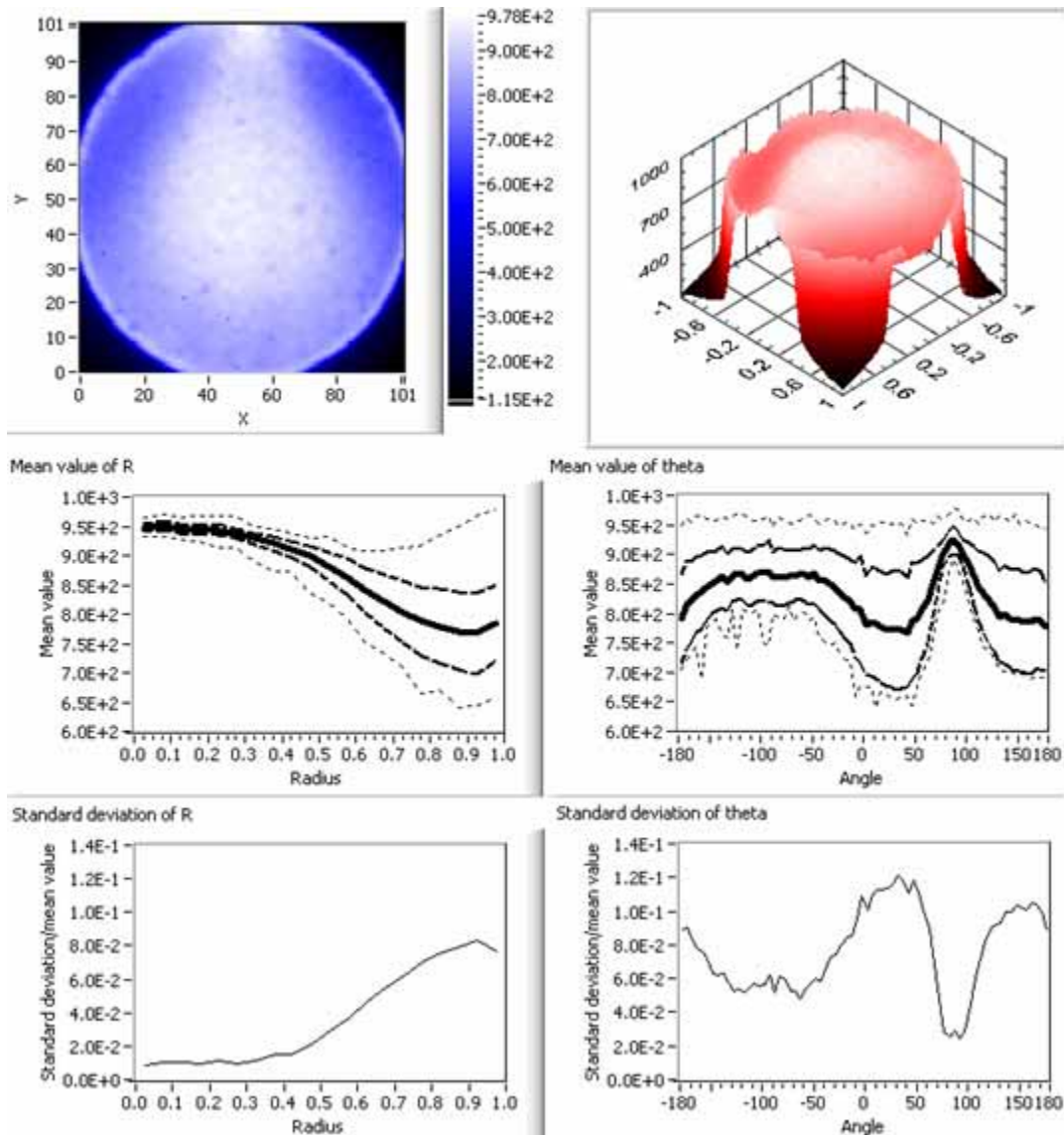
Figure 7.20: Measured Nd:YAG fluorescent pattern in the rooftop cavity

Table 7.1 shows the simulated and measured non-uniformity results of the different pumping features. Our experiment results confirm the trend of ASAP simulation results. The "D" and rooftop cavities reduce the non-uniformity efficiently. The measured non-uniformity is less than the ASAP simulation because the pixel number of the ASAP simulation is about 40% less than the measured CCD camera data.

Table 7.1 The simulation and experimental non-uniformity results of different pumping setup

	ASAP simulation			Experiment		
	Radial	Angular	Overall	Radial	Angular	Overall
Free standing rod	62%	40%	36%	33%	22%	22%
Elliptical	40%	50%	41%	-	-	-
CUSP	40%	22%	25%	-	-	-
"D"	**15%**	**23%**	**18%**	**12%**	**12%**	**10.6%**
Rooftop	**18%**	**15%**	**11%**	**8%**	**12%**	**9.4%**

Figure 7.21 compares the Nd:YAG rod fluorescent pattern in different pump cavities. Figure 7.22 is the same experiment but using Nd, Cr:GSGG instead. The gold-plated "D" cavity and spectralon "D" cavity do not show significant differences. The Rooftop cavity experiment shows higher fluorescence in the center. Also, the rooftop pattern is slightly tilted comparing with the "D" cavity. However, the observed "pig ears" do not differ significantly between the different pump cavity designs.
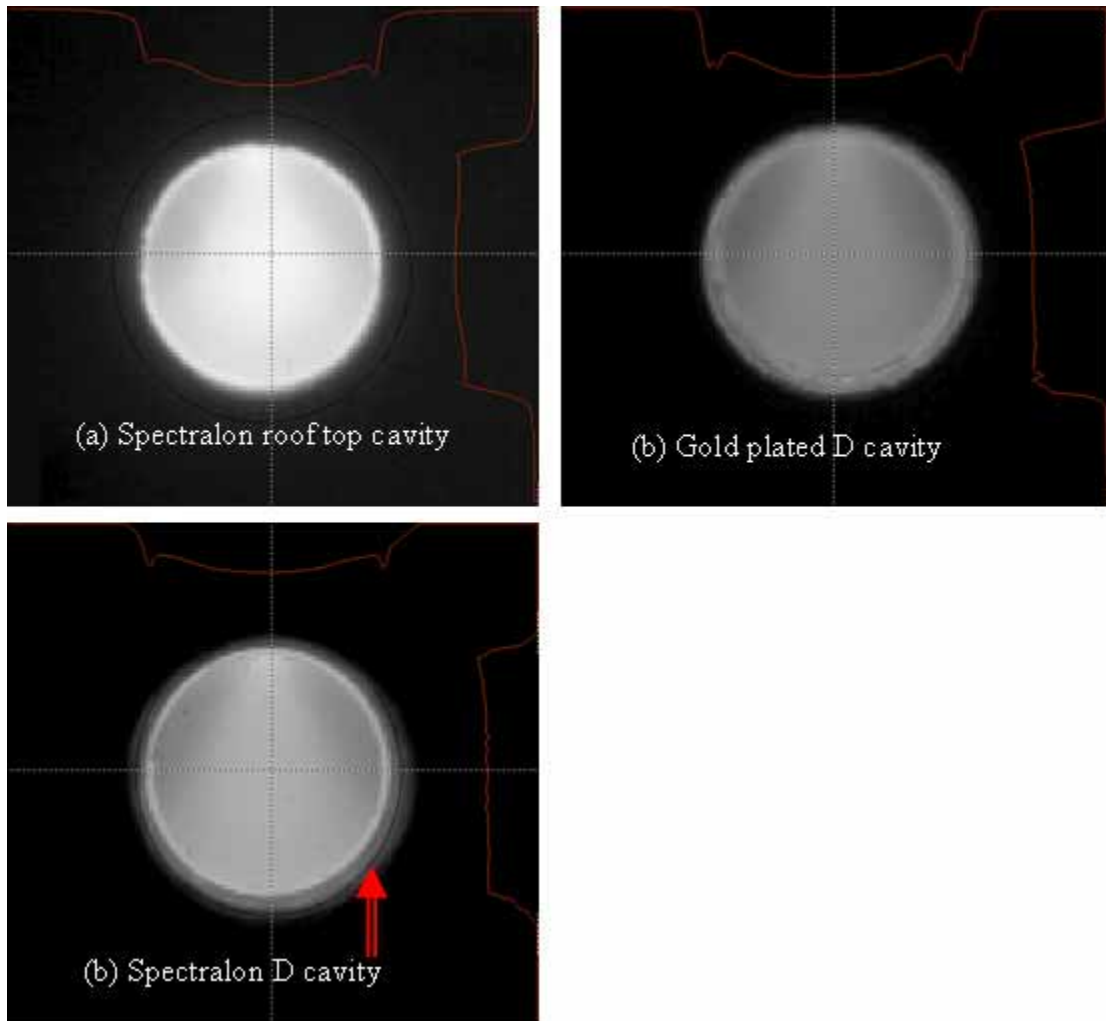
Figure 7.21: Nd:YAG rod in different cavities pumped by diode laser array centered at 808 nm
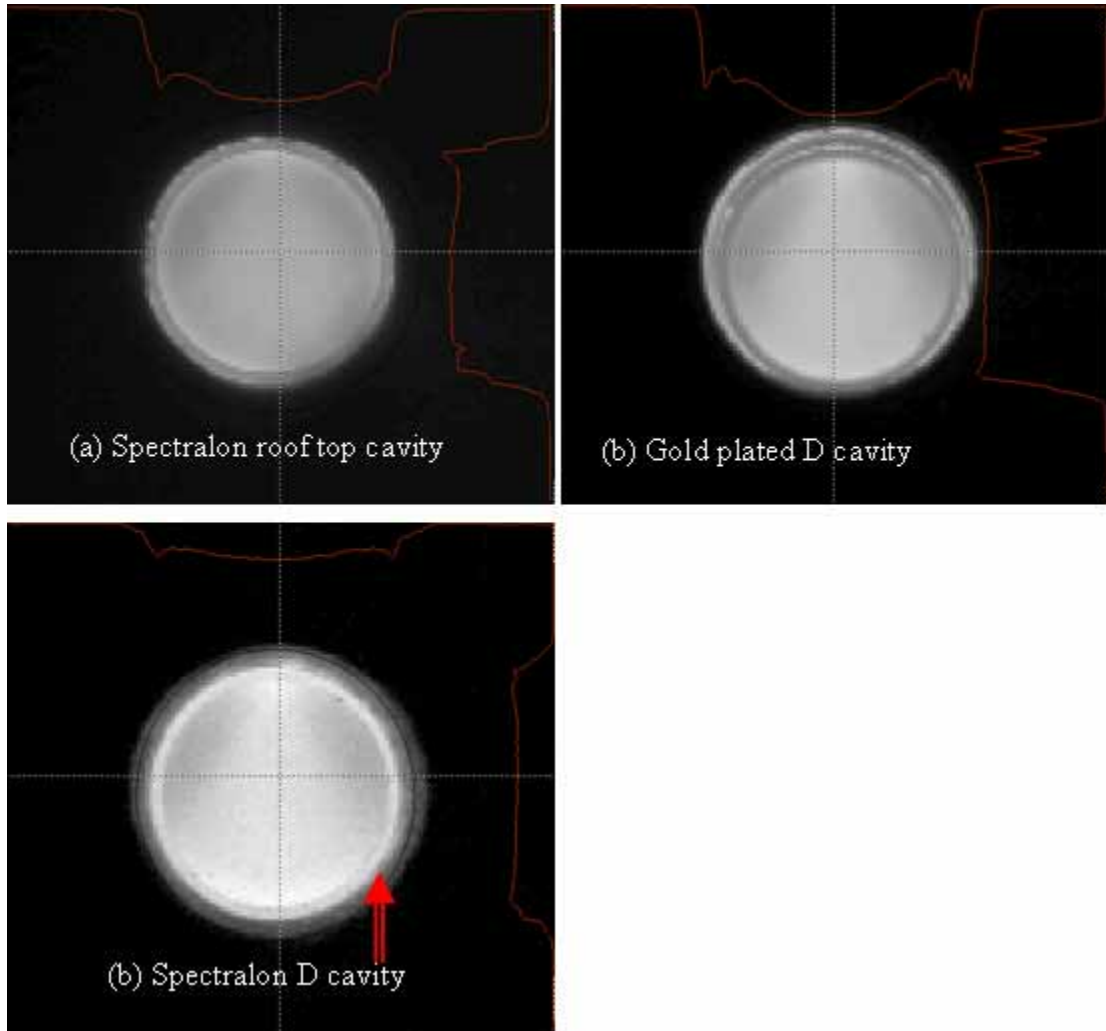
Figure 7.22: Nd, Cr:GSGG rod in different cavities pumped by the diode laser array centered at 808 nm

7.5 Summary of pump cavity design

We use ASAP to simulate the absorbed pump power distribution in a rod shaped gain medium pumped by a diode laser array inside different pump cavities. Using ASAP we perform several systematic studies of different parameters of the pumping set up to study the behavior of the absorption inside the rod. Our study shows:

1. The cavity reflectivity strongly influences the absorption efficiency of the rod.

2. The non-uniformity is slightly dependent on the cavity reflectivity.

133

3. A large distance between the rod and the diode array can reduce the absorption efficiency.

4. If the distance between the rod and the diode array is smaller than 1.5 mm, for the rod and array dimension we considered, the absorption pattern will be less uniform.

5. The rod surface roughness doesn't influence the absorption efficiency.

6. When the rod surface scattering angle is smaller than 45°, uniformity is reduced.

7. The rod absorption coefficient has an optimized value for the best uniformity when αR = 1.5.

We made three pump cavities: a Spectralon rooftop cavity, a spectralon "D" cavity, and a gold plated "D" cavity. All the cavities were tested and a free standing rod experiment was also performed. Our experimental results show:

1. The free standing rod and other cavity designs have a similar fluorescent pattern containing the more weakly pumped regions called "pig ears". However, the cavities do make the fluorescent pattern more uniform than for the free standing rod.

2. The experimental results show good agreement with our ASAP simulations.

Our cavity designs provide a simple, feasible and low cost solution to utilize commercially available diode array stacks to pump laser rods efficiently and uniformly.

8. FUTURE WORK

8.1 BCP

Beam control prisms are conceptually simple because they are the combination of mirrors and lenses. The geometric optics properties of BCPs are either well-known or been discussed in Chapter 4. Therefore, the improvement in the future will be focused on the aberration correction and manufacture process.

8.1.1 Aberration correction

Aberrations are inevitable for circular surface BCPs. Since BCPs are large NA optical elements, they will suffer from strong aberrations. The aberrations will form interference fringes which are not preferred for most applications. Using a conic surface can eliminate aberration as we have discussed in Chapter 4. We propose two other ways to reduce or even eliminate aberrations in this section. One is to use GRIN material and the other is to use micro optics.

8.1.1.1 GRIN material

Typically, a commercially available GRIN lens still has aberrations. Spherical aberration is dominant but the aberration of a typical GRIN lens is about or less than one wavelength[22] which is smaller than a ball lens. GRIN cylindrical lenses are ideal for correcting the fast divergence angle of a diode bar. Therefore, we can consider a new type of BCP based on a GRIN cylindrical lens. Figure 8.1 shows the combination of a GRIN cylindrical lens and a 45°-90°-45° prism. The 45°-90°-45° prism is optically contacted with the GRIN cylindrical lens. The GRIN cylindrical lens collimates and the prism redirects the light. This BCP has a longer working distance than other BCPs. However, the angular tuning capability of this combination is relatively poor.
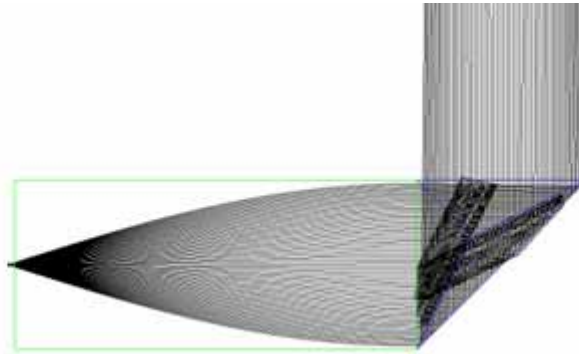
Figure 8.1: A GRIN cylindrical lens combines with 45°-90°-45° prism

A cylindrical surface gives considerable spherical aberration when the folded-ball BCP design is used. This is an inevitable problem for commonly used optical materials. The marginal rays have a shorter focal length and the chief rays have a longer focal length. Therefore, a lower index of refraction outer layer can increase the focal length of the marginal rays. If a proper index of refraction distribution is chosen, the lens can be

aberration-free. Figure 8.2 shows the ray tracing of a GRIN rod lens which index of refraction distribution is shown in Figure 8.3. The outmost layer index is about 1.3 and a well-defined focal point can be obtained. Sol-Gel materials can have index of refraction as low as 1.2 making this design possible. Not only can GRIN materials work as a BCP but they also make other high NA applications possible. Another benefit inherited from the folded-ball design is that the focal point is independent from the BCP tilt angle. Even if a GRIN lens does not have an index of refraction profile as shown in Figure 8.3 spherical aberration will still be reduced compared with a uniform index BCP.
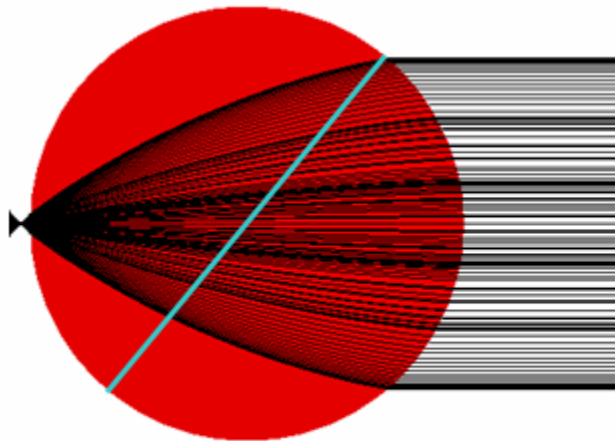
Figure 8.2: Radial GRIN lens ray tracing result

$$n(x,c) := 1.5 + c \cdot x^2$$
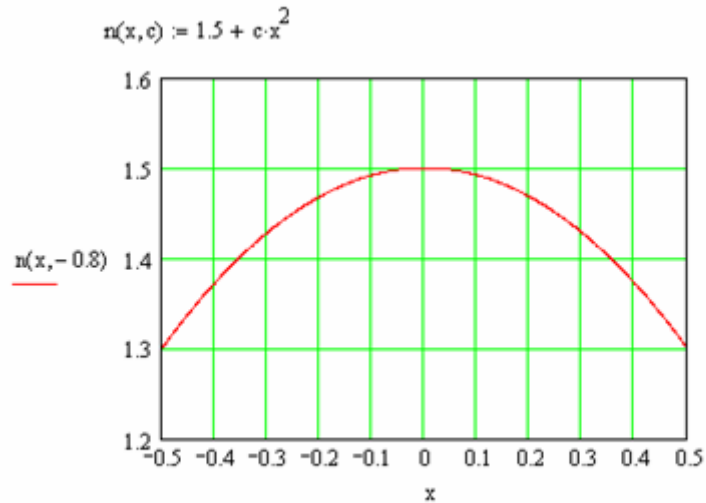
Figure 8.3: GRIN index profile for the small spherical aberration ball lens

8.1.1.2 Micro optics

Once the specific design of the BCP is decided, we can use ray tracing or analytic means to solve the wavefront aberration of the lens. Once the wavefront is determined, a micro optics lens array can be made within inverse wavefront shape to compensate the wavefront and make the new wavefront into a desired shape. Figure 8.4 shows the concept of using micro optics to correct the aberrations.
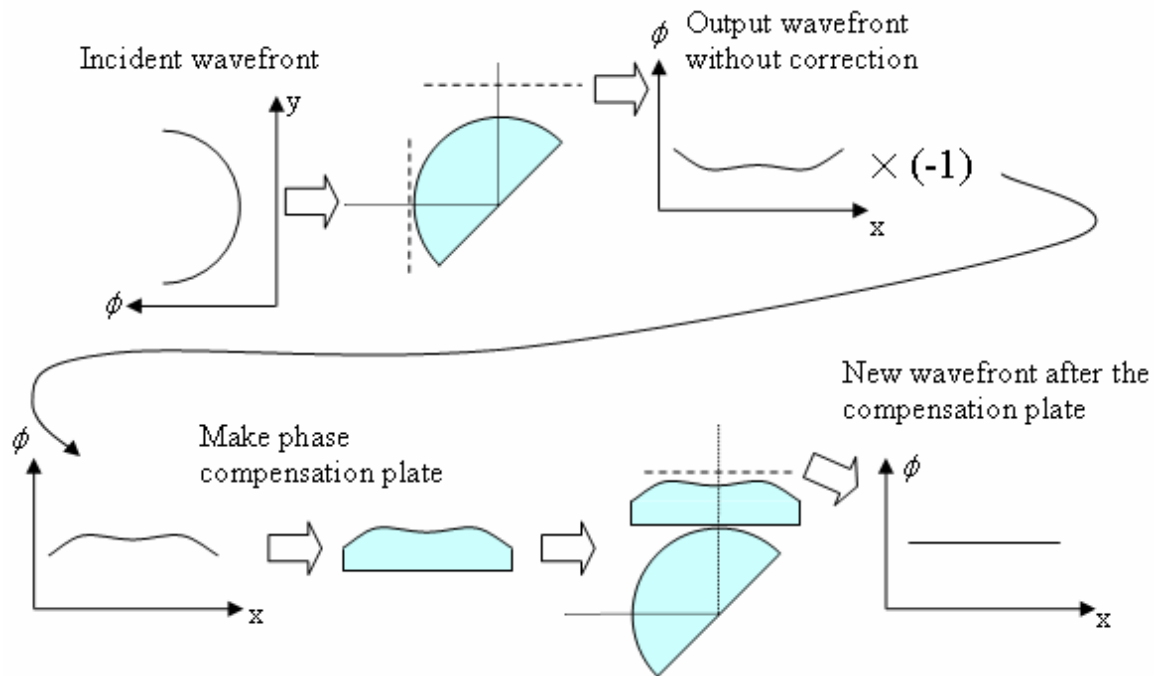
Figure 8.4: Concept of using micro optics to correct aberrations

8.1.2 Manufacturing process

Since basic BCPs are cylindrical lenses, optical plastics like PMMA can be shaped into a BCP by plastic extrusion. Molten plastic or synthetic fiber can be extruded through a flat, horizontal die onto a chilled roller (cast film) or quenching water bath. Injection molding is also another possibility. These methods make mass-production of BCP possible. Another benefit of injection molding is it may make it possible to combine the BCP with slow divergence angle control micro lenses in a single optic.

8.2 BCPP

In Chapter 5 we discussed various issues of BCPP thoroughly. However, current BCPP designs still have some problems and disadvantages. In this section, several improvements of BCPP are proposed.

8.2.1 New packaging design with less distortion

Table 8.1 lists several commonly used materials for diode packaging. In our design, we used direct bond copper on a BeO substrate.

Table 8.1 Thermal expansion coefficients of commonly used materials for diode packaging (293K)[5]

Material	Typical Thermal Conductivity, W/cm/K	Thermal Expansion Coefficient, ppm/K
CVD Diamond	10-18	1.5
Alumina	0.25	8
Aluminum Nitride	1.7	4.6
Beryllia	2.5	6.4
CuW/90/10	1.7	6.5
Silver	4.1	19
Copper	3.9	17
Silicon	1.5	4.1
GaAs	0.44	6.5
BeO[6]	2.6	8.0

Direct bonding of copper to BeO is a process that takes place at a temperature exceeding 1000°C.[23] Because of the thermal expansion coefficient mismatch between BeO and copper, both sides of the BeO must be bonded with copper layers in order to balance the stress. Soldering diode bars and electrodes on such a BeO substrate requires heating all parts to ~200°C. Because the diode array operation temperature is only slightly above room temperature the thermal expansion coefficient mismatch of the BeO

---

[5] http://www.p1diamond.com/prop_ref.html

[6] http://www.stellarind.com/3beo.htm

substrate, diode bars and electrodes will cause stress and bending of the whole array. However, in our current design, 11 channels cut through the upper copper layer into the p-electrodes. It causes the stress to be out of balance when the whole substrate is heated. A simple estimation of the length difference in a 3 cm long copper layer on BeO is about 5.4×10^{-3} cm. This length difference makes the substrate bend forward towards the p-electrode side of the substrate with a radius of curvature of ~ 55 cm. The height different between the two ends will be ~ 0.8 mm which will be a major problem when soldering the diode bars and n-electrodes. After the whole array cools down, the substrate may not recover its original shape. If the substrate still has residual distortion this bending will make the solder layer between the substrate and the cooling plate have an uneven thickness and may reduce the uniformity of the temperature distribution.

Two methods are proposed for future substrate designs to reduce the thermal expansion mismatch problem. Figure 8.5 is based on the original BeO substrate design with deeper channels which reach the copper layer on the other side of the BeO substrate. The BeO layer is cut into several isolated blocks. Therefore, when the substrate temperature increases, the deformation can be significantly reduced because the back copper layer can expand more freely. However, an extra layer of insulation material might be needed to fill in the bottom of the channels in order to keep the BCPs on axis.
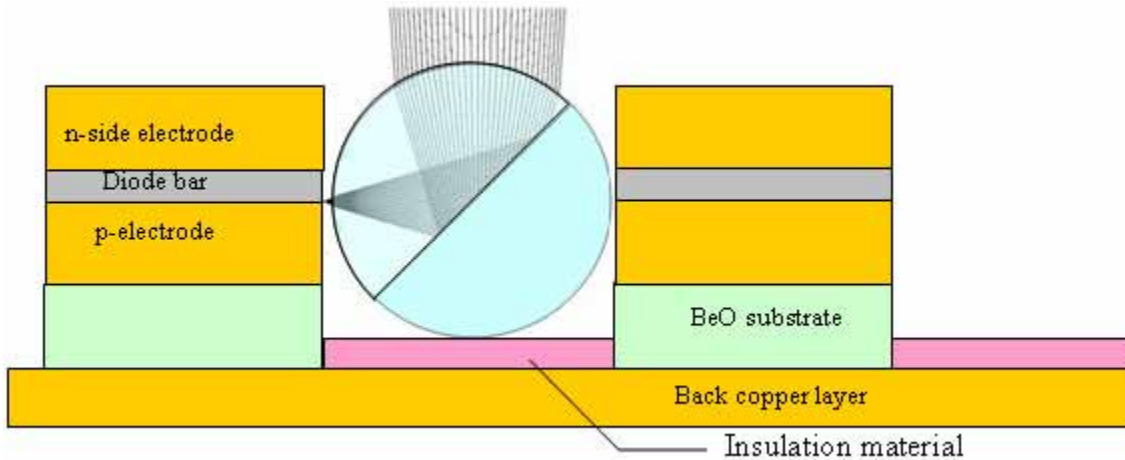
Figure 8.5: Improved BeO substrate design

A piece of CVD diamond or a thin plate of BeO can be metallized on both sides. Then this piece of insulating plate can be cut into strips which are the same width but longer in length than the diode bars. As Figure 8.6 shows, we can stack the electrode, diode bar and CVD diamond or BeO stripe together with solder layers in between each part. The dimensions of all the parts are similar or even identical to our current BeO substrate design described in Chapter 5. All the sub-modules can then be placed on a common substrate which may be the top of a spray cooling chamber or the cold surface of other cooling devices. The common substrate material can be copper or even a piece of CVD diamond. After the soldering process, BCPs can be placed in the channel. Using this assembly method, thermal stress can be greatly reduced by the less stiff solder layers. The other major advantage of this method is all the parts and the necessary assembly techniques are available and well-developed. However, the major trade-off of this design is that the extra solder layers increase the thermal resistance.
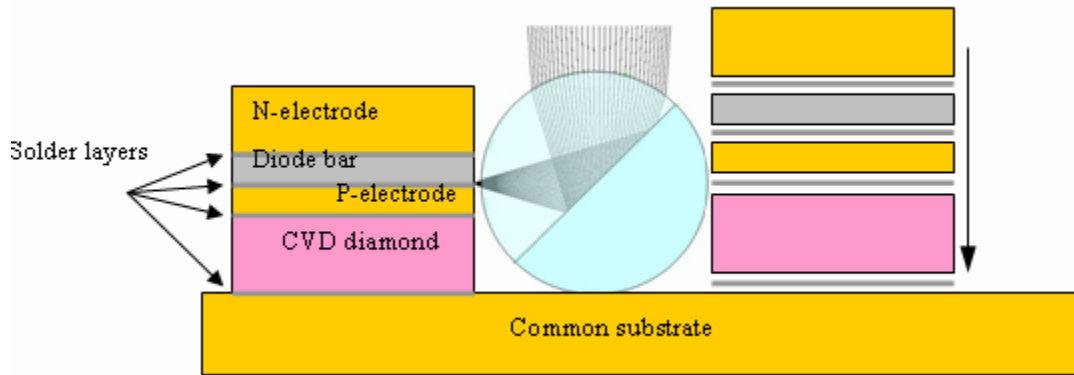
Figure 8.6 CVD diamond stripe BCPP design

8.2.2 Shaped substrate

A non-uniformly cooled diode laser bar will have undesired thermal stress and a broad laser emission spectrum. The finite element analysis results for our current package clearly shows the edge effect in Figure 5.15 and Figure 5.16. Our experimental results also confirm the trend of the simulation results as seen in Figure 5.21 and Figure 5.25. Because the edge emitters have better cooling in the current design, their temperature is lower than those in the middle of the array. We can't easily cool central emitters better but we can reduce the cooling of the edge emitters. The most straightforward method is to shape the substrate.

We propose two different shaped substrate designs to make edge emitters have higher thermal resistance. The design shown in Figure 8.7(a) has a smaller contact area with the cooling device. This design increases the thermal resistance of the edge emitters because their cooling path is longer than it is for the other emitters.

Figure 8.7(b) shows an ice-cube-tray cooing surface design which applies for a spray cooling device. Edge emitters have a relatively longer cooling path in this setup.

Therefore, the temperature of the edge emitters will be higher than if the cooling surface were uniform. This design also increases the mechanical stiffness of the substrate for spray cooling. This ice-cube-tray structure also guides the spray jet and vapor back into the chamber and to the condenser coil.
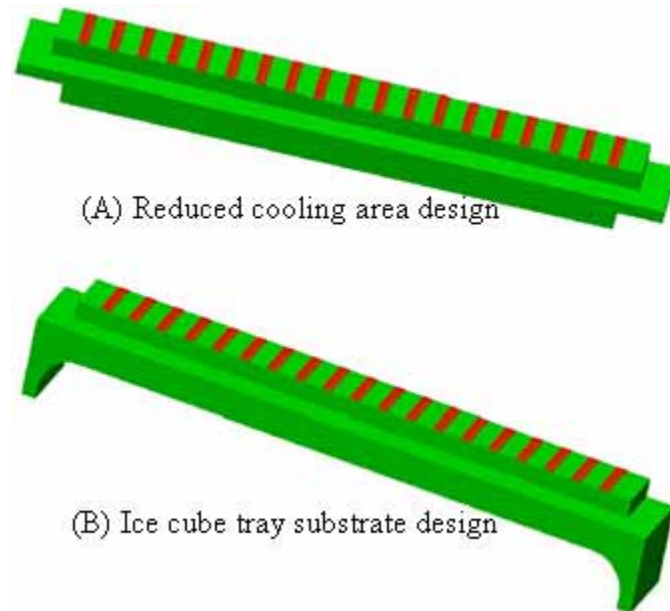

Figure 8.7: Shaped substrate designs for achieving better temperature uniformity

Not only the edge emitters of a diode bar suffer from the edge effect, but also the edge diode bars of a diode array have lower temperature compared with the bars in the middle. Therefore, we can also using the similar shaped-substrate concept to achieve better uniformity.

A FEMLAB FEA simulation was performed for calculating the temperature distribution of the reduced cooling area shaped substrate design. The simulation is based on the same BCPP design described in Chapter 5 but the back copper surface and the 1 mm copper layer have a smaller footprint. We assumed the heat transfer coefficient for

spray cooling is 180,000 W/m^2·K and computed the temperature distributions shown in Figure 8.8 that would develop for several different widths of the copper layer that is directly cooled. The current BCPP design uses a back copper layer that is 13.6 mm wide. The maximum temperature difference between emitters in this case is about 12°C. The optimized back copper layer width is about 9.4 mm. With this back copper layer width the maximum temperature difference between the emitters is only 1.3°C.

The temperature distribution of the entire array is shown in Figure 8.10 and Figure 8.11. Comparing these two figures with Figure 5.17 and Figure 5.18 we see that the central emitter temperature of the shaped-substrate design is about 5°C higher, but the temperature distribution is much more improved. The temperature difference between bars is even smaller as shown in Figure 8.11.
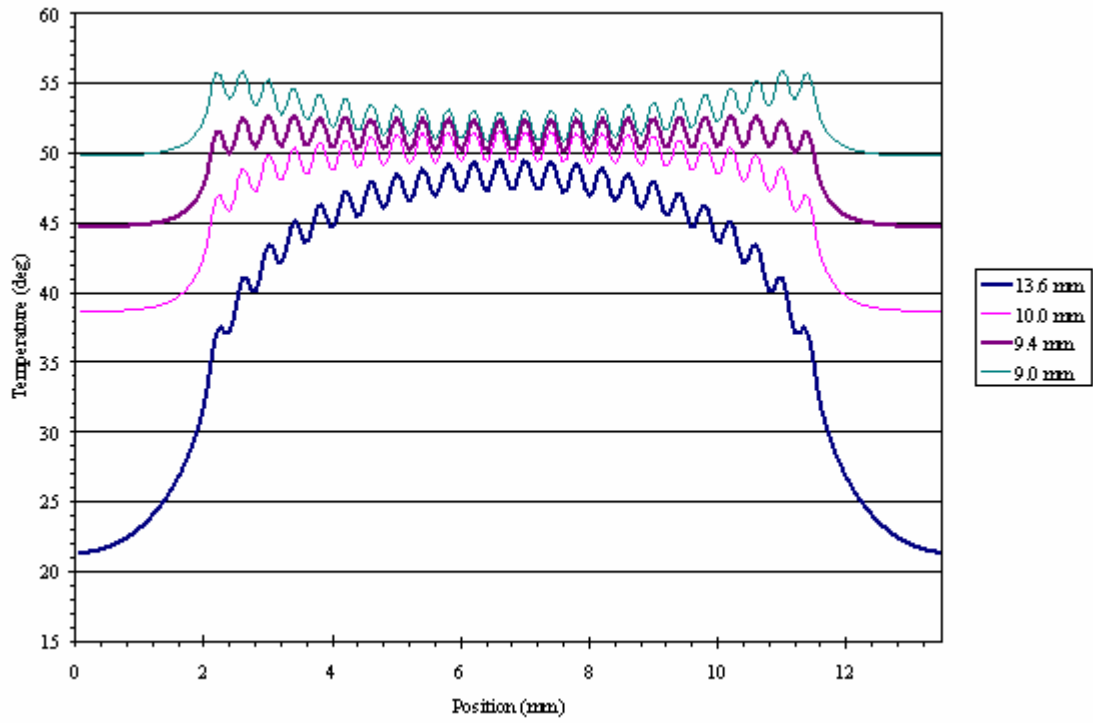
Figure 8.8: Temperature distribution of a single bar on the reduced-cooling-area shaped substrate design with different shaped back copper and cooling surface widths
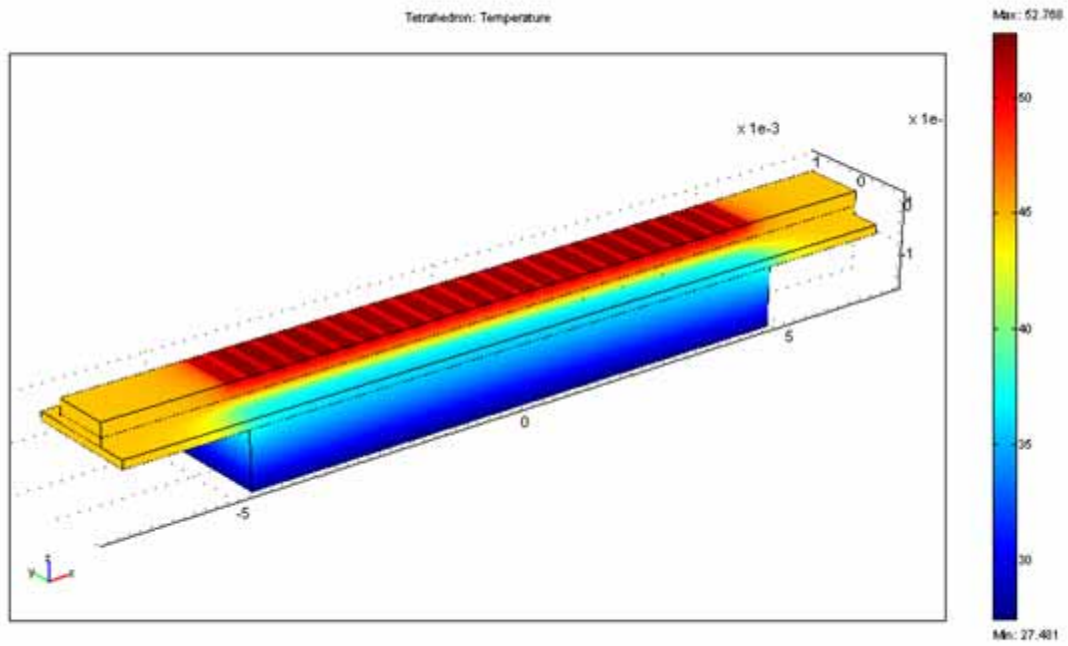
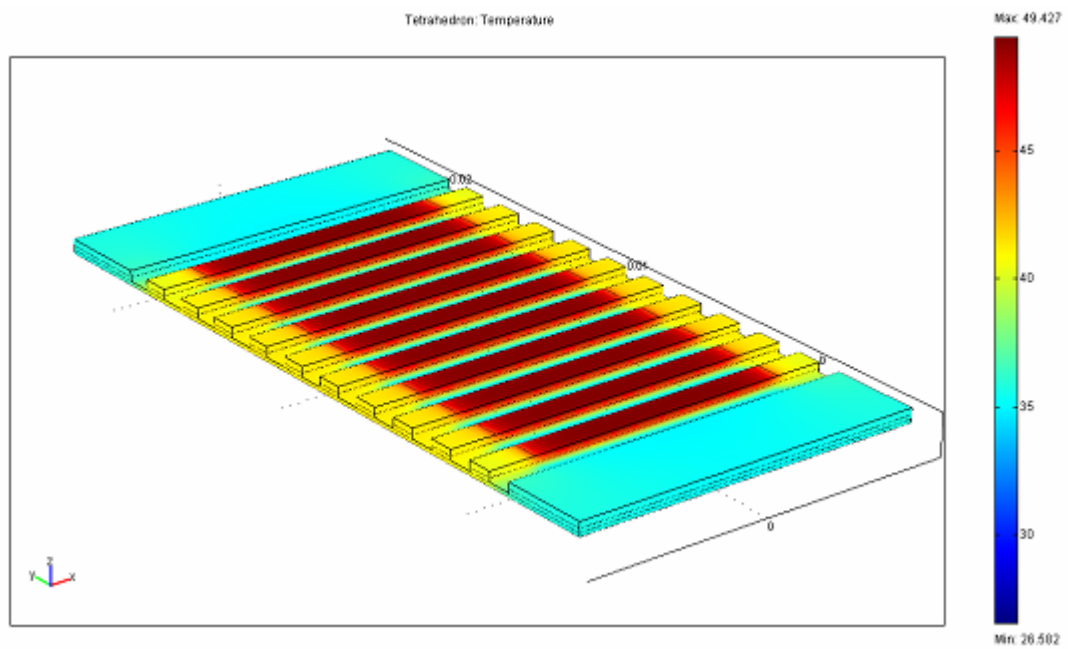Figure 8.9: Single bar simulation of shaped substrate designs

Figure 8.10: Whole array simulation of a shaped substrate design

148
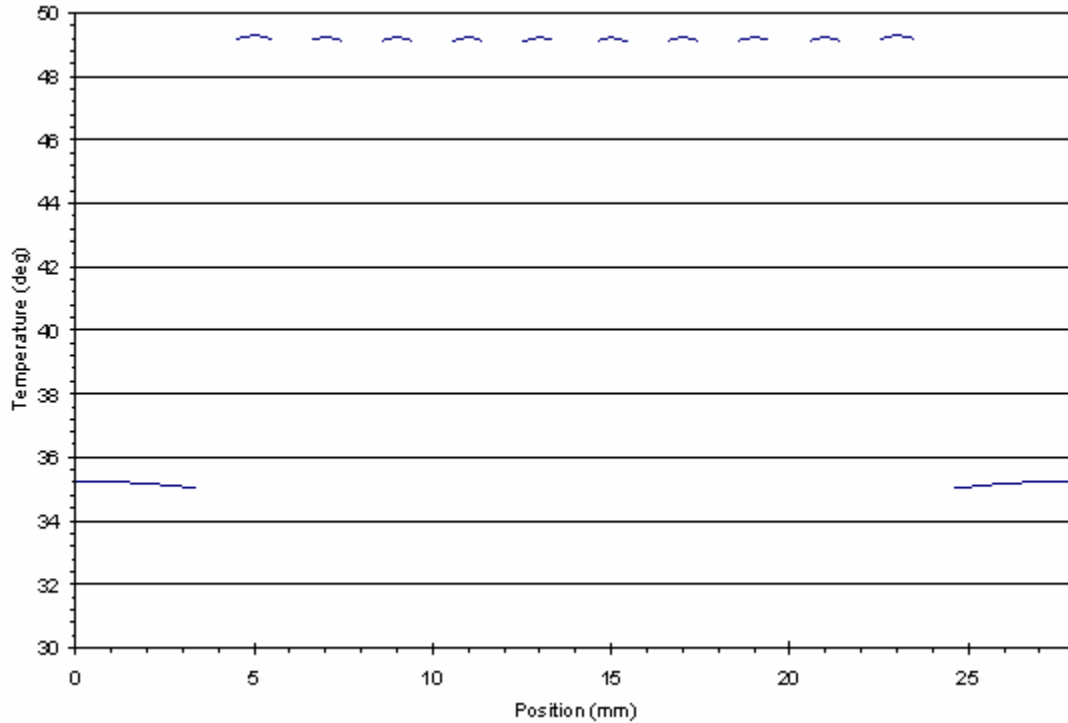
Figure 8.11: Temperature distribution of different bars on the shaped substrate

8.2.3 Tunable BCP

In Chapter 4, the angular tuning of BCP was discussed but our current designs concentrate on fix beam angle BCPs. Eq. (4.2) gives the positioning tolerance which also indicates the angular tuning range of the BCPs. Figure 5.19 also shows that beam direction angular tuning can be easily achieved. A small displacement of the BCP along Z axis can change the beam angle. Consequently, we can place a piezoelectric transducer at the bottom of the BCP channel. By changing the voltage applied to the PZT the beam angle can be changed to a different direction. Figure 8.12 is a sketch of the concept of the real time beam direction angular tuning design. A tunable BCP can be a high power

149

laser scanner or a scanning illumination light source. Several different types of actuator devices such as ultrasonic motors, piezoelectric transducers, and MEMS can be used for rotational movement to enable larger angular tuning range.[24]
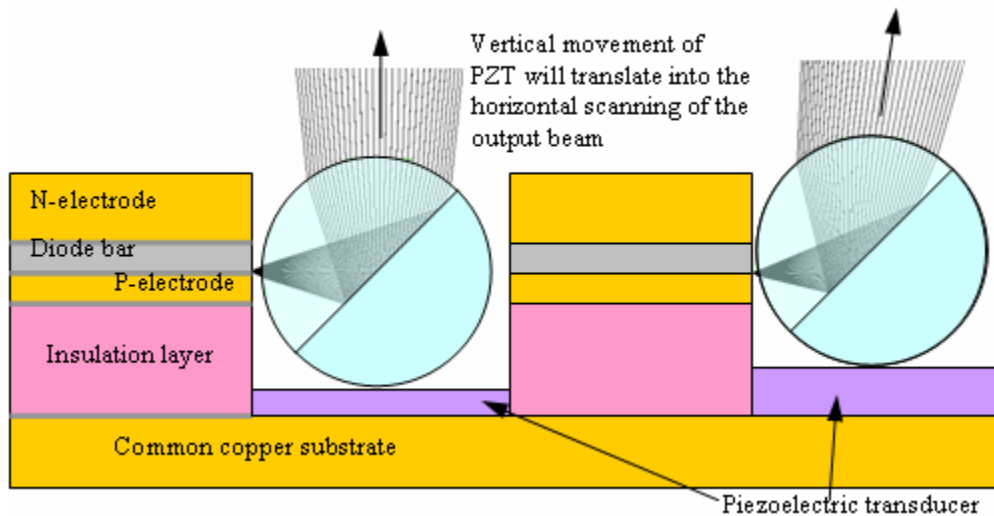
Figure 8.12: Conceptual design of real time beam direction angular tuning by using a PZT transducer

8.3 Slow divergence axis control

The slow divergence axis control of the diode laser was discussed thoroughly in Chapter 6. There we showed that a single 8 level Fresnel micro cylindrical lens device can not have full control of the slow axis divergence angle without losing a considerable amount of the laser power. However, if molded plastic optics[7] can be used it is possible to make a miniaturized cylindrical lens array with suitable NA. Another benefit of using molded plastic optics is that the slow divergence angle control can be integrated with the BCP. Also, aspherical lens surfaces can be made to correct the spherical aberration in

both slow and fast divergence axes corrections. Using plastic optics can also reduce the cost of BCPs substantially. However, the trade-off is that the index distribution within a molded component may be inhomogeneous it may experience stress birefringence.

8.4 Pump cavity design

Even though the "D" and rooftop cavity designs reduce the non-uniformity of the gain distribution in the laser rod more study of cavity designs is necessary. The "pig ears" have to be eliminated in order to reach optimum uniformity. Consequently, new cavity designs have to focus on delivering more pump light entering the rod from the side furthest from the diode laser array stack. It is also important to reduce the number of bounces of the rays in the cavity to improve the efficiency.

Figure 7.8 (b) shows the absorbed pump power distribution pattern of a smooth elliptical pump cavity with rod axis centered on one focal line and diode bars in the plane of the other focal line. This shows the similar absorption at the face closer to the diode bars. Nevertheless, most of the light enters the rod from the side further from the diode array stack, actually right at the position of the "pig ears" of the "D" and rooftop cavities. If the surface is diffusive, as is that of Spectralon, the simulation result is similar to the "D" and rooftop cavities' distribution with "pig ears" at the same position. Therefore, cavity surface roughness or scattering properties clearly play a very important role in determining the absorbed pump power uniformity. Cavity surfaces with the roughness between Lambertian and specular might give a more uniform gain distribution.

---

[7] http://www.sunex.com/CustomOptics/plastic-optics.htm

All the previous simulations consider only the rod in the pump cavity. A practical experimental setup contains a water jacket and flowing water to cool the rod. Therefore, a more realistic simulation needs to consider the effect of these cooling elements in the cavity on the distribution of absorbed power. Figure 8.13 is the preliminary experimental fluorescence distribution in a Nd:YAG rod in a rooftop cavity with water jacket and water in the jacket. The overall non-uniformity in this experiment is only 6% which is even better than previous simulation results and experimental results without water jacket and water. This is caused by the lens effects of the extra elements that make the light spread more than when they are absent. However, the extra elements require extra bounces in the pump cavity which will reduce the overall pump efficiency.
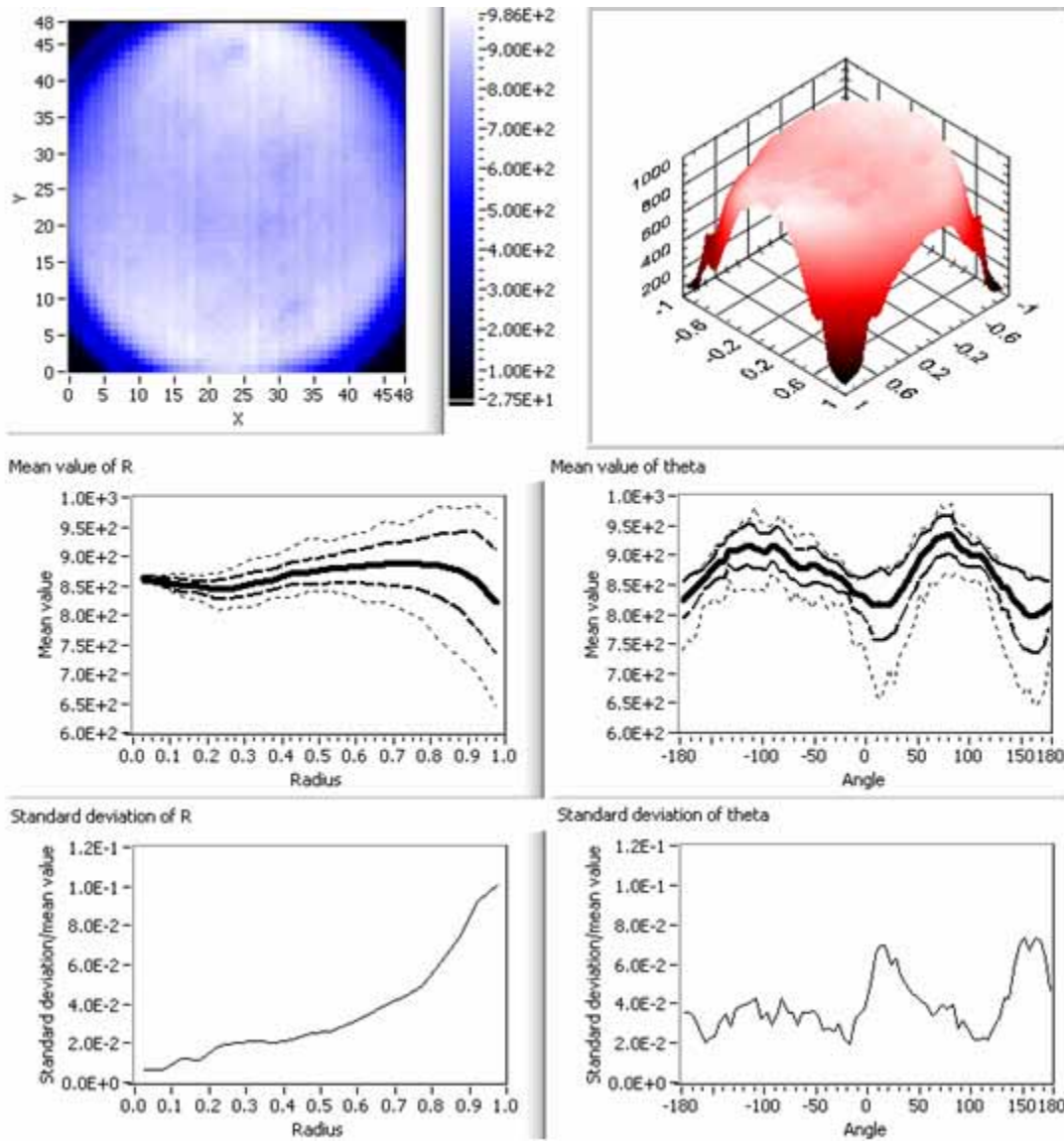
Figure 8.13: Preliminary experimental result of a rooftop cavity with a rod cooling water jacket inside the cavity

APPENDIX: BCP ACCEPTANCE ANGLES CALCULATION

Part A: MathCAD code and calculation of the acceptance angle for a folded-ball BCP

Acceptance angles calculation for folded-ball BCP

Redefine trigonometry in deg

$$sind(x) := sin(x \cdot deg)$$

$$asind(x) := asin(x) \cdot \frac{180}{\pi}$$

$$cosd(x) := cos(x \cdot deg)$$

$$acosd(x) := acos(x) \cdot \frac{180}{\pi}$$

$$tand(x) := tan(x \cdot deg)$$

$$atand(x) := atan(x) \cdot \frac{180}{\pi}$$

$$R := .5 \quad \text{Unit : mm}$$

Upper acceptance angle calculation

$$\beta_1(n,\beta) := asind\left(\frac{sind(\beta)}{n}\right)$$

$$\alpha(n,\beta,\delta) := 2 \cdot \beta_1(n,\beta) - \delta$$

$$\phi_1(n,\beta,\delta) := \beta - \alpha(n,\beta,\delta)$$

$$a_1(n,\beta,\delta,R) := R \cdot sind(2 \cdot \beta_1(n,\beta) - \delta)$$

$$\Delta_1(n,\beta,\delta,R) := R - R \cdot cosd(\alpha(n,\beta,\delta))$$

Lower acceptance angle calculation

$$bfl_m(n,\beta,\delta,R) := \frac{a_1(n,\beta,\delta,R)}{tand(\phi_1(n,\beta,\delta))} - \Delta_1(n,\beta,\delta,R)$$

$$\Delta_2(n,\beta,\delta,R) := R - R \cdot cosd(\delta)$$

$$\phi_2(n,\beta,\delta,R) := atand\left(\frac{R \cdot sind(\delta)}{\Delta_2(n,\beta,\delta,R) + bfl_m(n,\beta,\delta,R)}\right)$$

Upper acceptance angle vs. material index of refraction
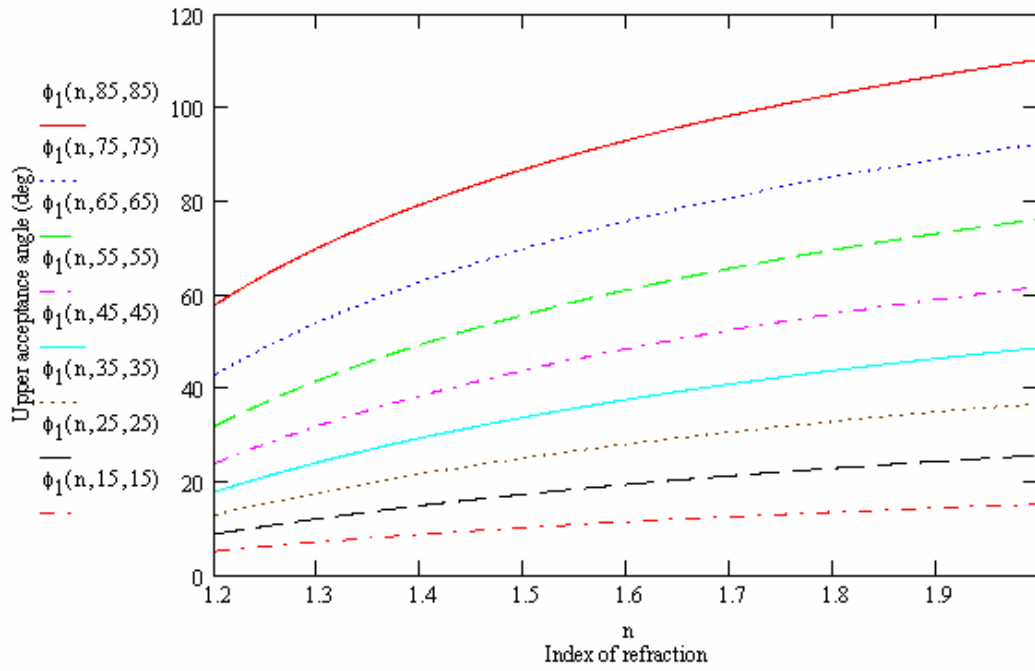
Lower acceptance angle vs. material index of refraction
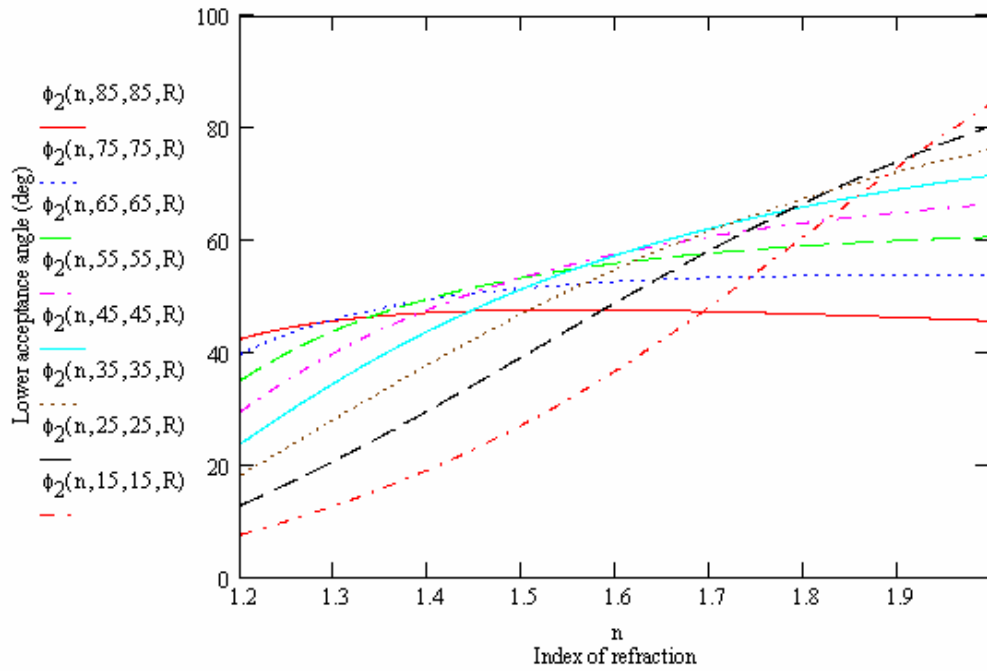
Part B: MathCAD code and calculation of the acceptance angle for a curved-exit BCP

Plano - convex BCP (Curved-exit)

Redefine trigonometry in deg

Material BK7   Radius of curvature

$$sind(x) := sin(x \cdot deg)$$

$$n := 1.51 \qquad R := 0.5 \qquad Unit:mm$$

$$asind(x) := asin(x) \cdot \frac{180}{\pi}$$

Focal length

Back focal length

$$cosd(x) := cos(x \cdot deg)$$

$$f(n,R) := \frac{R}{n-1}$$

$$BFL(n,R) := f(n,R) \cdot \left[1 - \frac{\left(R + \frac{R}{\sqrt{2}}\right) \cdot (n-1)}{n \cdot R} \right]$$

$$acosd(x) := acos(x) \cdot \frac{180}{\pi}$$

$$tand(x) := tan(x \cdot deg)$$

$$F(n,R) := \frac{f(n,R)}{R \cdot \sqrt{2}} \quad F \text{ number}$$

$$atand(x) := atan(x) \cdot \frac{180}{\pi}$$

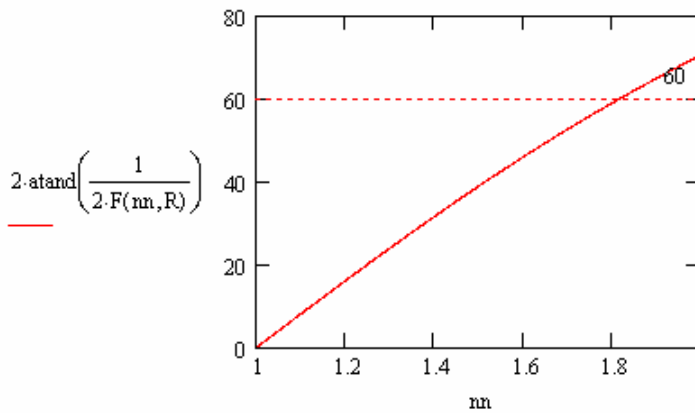Back focal length vs. material index of refraction

$BFL(nn,R)$
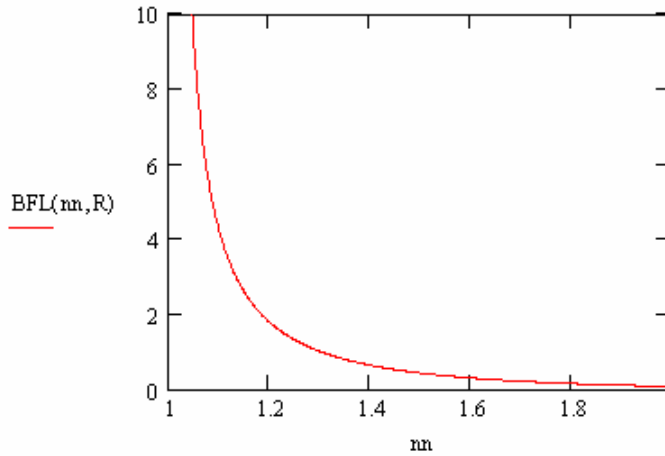
Back focal point inside BCP condition

$$x := 1.6$$

$$root(BFL(x,R),x) = 2.413$$

The index of refraction has to be larger than 2.413 to make the back focal point inside the BCP. Therefore, it's not an issue.

Full acceptance angle at 90 deg beam angle vs. material index of refraction

$$2 \cdot atand\left(\frac{1}{2 \cdot F(nn,R)}\right)$$

157

$$\theta_r(n,\theta) := \text{asind}\left(\frac{\text{sind}(\theta)}{n}\right) \quad \text{Refraction angle from Snall's law}$$

$$t_c(n,R,\theta) := R + \frac{R}{\sqrt{2}} \cdot \frac{1}{\text{cosd}(\theta)} \quad \text{BCP effective physical thickness}$$

$$\text{bfl}(n,R,\theta) := f(n,R) \cdot \left[1 - \frac{t_c(n,R,\theta) \cdot (n-1)}{n \cdot R}\right] \quad \text{Back focal length}$$

$$\psi(n,\theta) := 90 + \text{asind}\left(\frac{\text{sind}(|\theta|)}{n}\right) + |\theta| \quad \text{Beam angle equation}$$

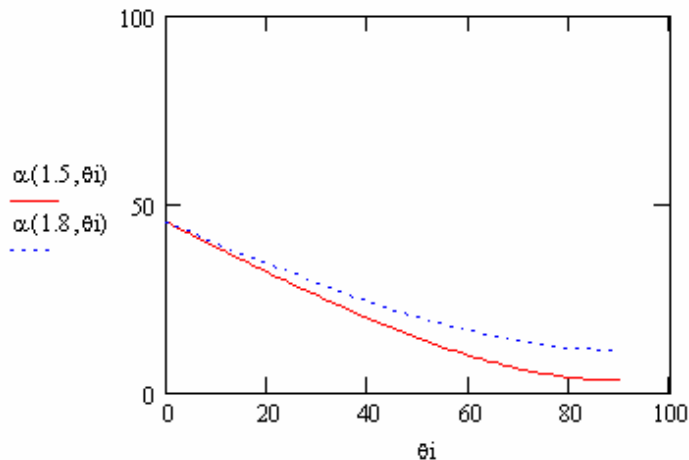$$\theta i := -90 .. 90$$

Output beam angle vs. incident angle when n=1.51

$$\alpha(n,\theta) := 45 - \theta_r(n,\theta)$$

158
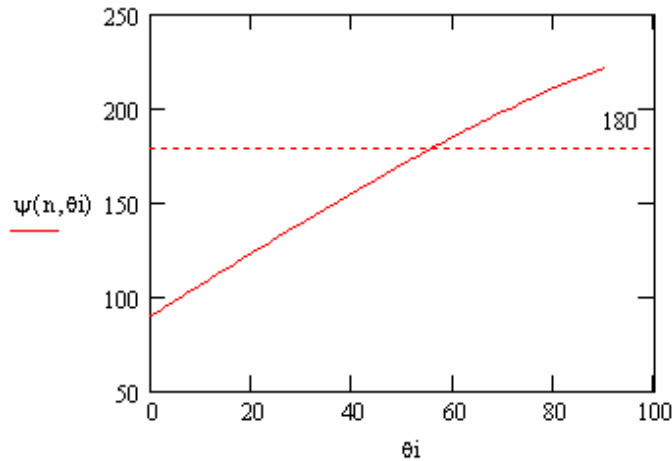
Effective lens semi-diameter at higher part at exit pupil

$$D(n, R, \theta) := 2R \cdot \text{sind}(\alpha(n, \theta)) \qquad \text{Incident angle } \theta$$

$$F(n, R, \theta) := \frac{f(n, R)}{D(n, R, \theta)} \qquad \text{F number}$$

$$nn := 1.8$$
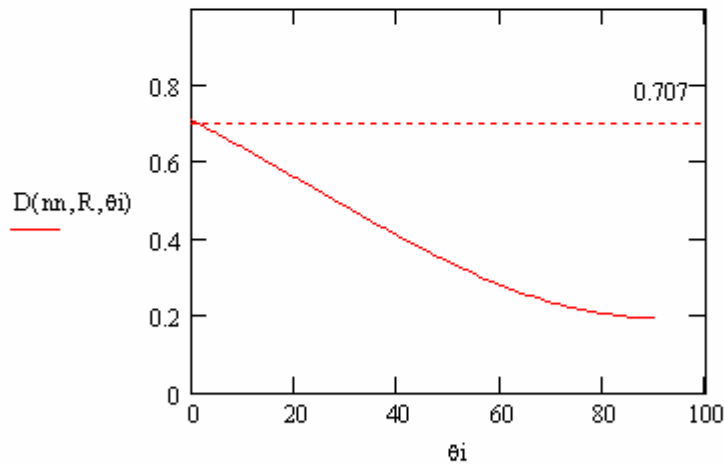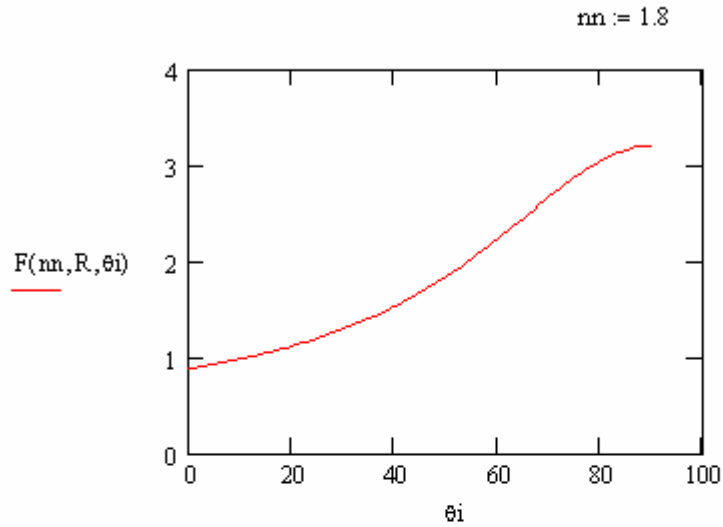
$$\text{root}(\text{bfl}(1.8, R, x), x) = -1.844 \times 10^{7}$$

When n=1.414 TIR occurs at the very edge of the prism

$$\theta_{ac}(n, R, \theta) := \text{atand}\left[\frac{D(n, R, \theta)}{2 \cdot \left[f(n, R) - (R - R \cdot \text{cosd}(\alpha(n, \theta)))\right]}\right]$$

$$R - R \cdot \text{cosd}(\alpha(n, \theta)) \qquad 2 \cdot \left[f(1.4, R) - (R - R \cdot \text{cosd}(\alpha(1.4, 90)))\right] = 2.5$$

$$D(1.4, .5, 0) = 0.707$$

159

Calculation of high acceptance angle

$\theta := 10$

$root\big(\psi(n,\theta) - 100, \theta\big) = 6.018$

$\theta_{ac\psi}(n,R,\psi_0) :=$
$\begin{vmatrix} \big[p \leftarrow (180 - \psi_0)\big] & \text{if } \psi_0 < 90 \\ p \leftarrow \psi_0 & \text{otherwise} \\ x \leftarrow 10 \\ \theta \leftarrow root\big(\psi(n,x) - p, x\big) \\ \theta_{ac}(n,R,\theta) \end{vmatrix}$

System is symmetry to $\psi = 90$ deg

ψ is the beam angle. Typical case is $\psi = 90$ deg

High acceptance angl vs. material index of refraction

$\theta_{ac\psi}(nx,R,90)$ —

$\theta_{ac\psi}(nx,R,110)$ · · ·

$\theta_{ac\psi}(nx,R,130)$

$\theta_{ac\psi}(nx,R,150)$ — ·

$\theta_{ac\psi}(nx,R,180)$
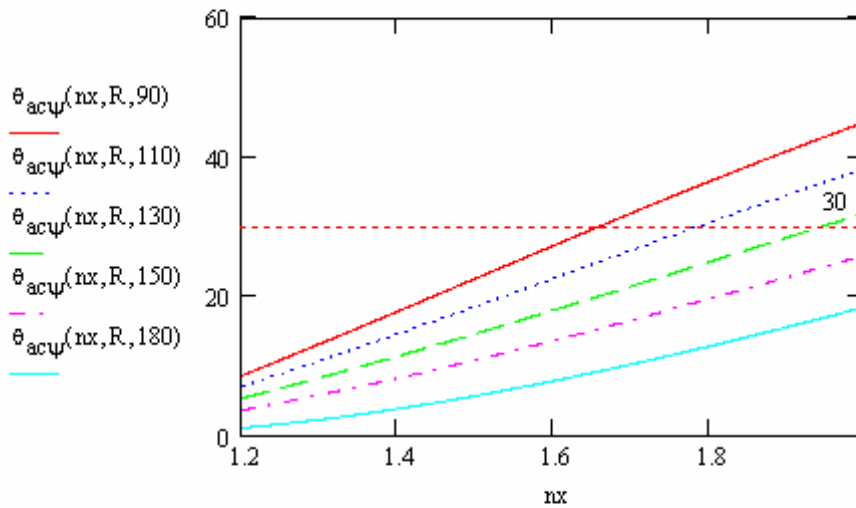
Effective lens semi-diameter for the lower part at the exit pupil

$DD(n,R,\theta) := 2 \cdot R \cdot sind\big(\theta_r(n,\theta) + 45\big)$

Calculation of low acceptance angle

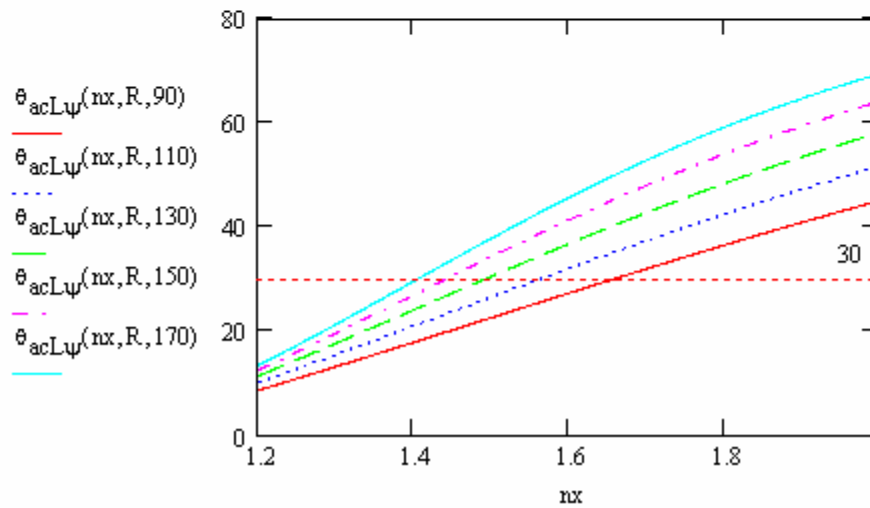$$\theta_{acL}(n,R,\theta) := \text{atand}\left[\frac{DD(n,R,\theta)}{2\cdot\left[f(n,R) - \left(R - R\cdot\text{cosd}\left(\theta_r(n,\theta) + 45\right)\right)\right]}\right]$$

$$\theta_{acL\psi}(n,R,\psi_0) := \begin{array}{|l}
\left[p \leftarrow \left(180 - \psi_0\right)\right] \quad \text{if} \quad \psi_0 < 90 \\
p \leftarrow \psi_0 \quad \text{otherwise} \\
x \leftarrow 10 \\
\theta \leftarrow \text{root}\left(\psi(n,x) - p, x\right) \\
\theta_{acL}(n,R,\theta)
\end{array}$$

Low acceptance angl vs. material index of refraction

$\theta_{acL\psi}(nx,R,90)$
———

$\theta_{acL\psi}(nx,R,110)$
·······

$\theta_{acL\psi}(nx,R,130)$
———

$\theta_{acL\psi}(nx,R,150)$
— · —

$\theta_{acL\psi}(nx,R,170)$
———

161

LIST OF REFERENCES

[1] M. Peter, V. Rossin, K. Tai et al., presented at the SSDLTR, Alburquerque, NM, 2004 (unpublished).

[2] M. Kanskar, Z. Dai, T. Earles et al., presented at the SSDLTR, Alburquerque, NM, 2004 (unpublished).

[3] J. Singh, *Semiconductor optoelectronics : physics and technology*. (McGraw-Hill, New York, 1995).

[4] R. Diehl, *High-power diode lasers : fundamentals, technology, applications*. (Springer, Berlin ; New York, 2000).

[5] Y. H. Lee, J. L. Jewell, A. Scherer et al., Electronics Letters **25** (20), 1377 (1989).

[6] J. G. Endriz, M. Vakili, G. S. Browder et al., IEEE Journal of Quantum Electronics **28** (4), 952 (1992).

[7] R. Beach, W. J. Benett, B. L. Freitas et al., IEEE Journal of Quantum Electronics **28** (4), 966 (1992).

[8] F. P. Incropera and D. P. DeWitt, *Introduction to heat transfer*, 3rd ed. (Wiley, New York, 1996).

162

9   L. C. Chow, M. S. Sehmbey, and M. R. Pais, in *Annual Review of Heat Transfer* (1997), Vol. 8, pp. 291.

10   L. C. Chow, J.J. Huddle, S. Lei, D. P. Rini, A. Marcos, T. Chung, S. J. Lindauer II, M. Bass, and P. J. Delfyett, presented at the SAE Power System Conference, San Diego, CA, Oct 2000 (unpublished).

11   D. P. DeWitt, F. P. Incropera, *Introduction to Heat Transfer*, 3 ed. (John Wiley & Sons, 1996).

12   X. Wang, USA Patent No. 6,327,285.

13   J. H. Kim, R. J. Lang, A. Larsson et al., Applied Physics Letters **57** (20), 2048 (1990).

14   W. D. Goodhue, J. P. Donnelly, C. A. Wang et al., Applied Physics Letters **59** (6), 632 (1991).

15   R. Hwu, USA Patent No. 6,259,713.

16   E. Hecht, *Optics*, 3 ed. (Addison-Wesley, New York, 1998).

17   M. Kufner and S. Kufner, *Micro-optics and lithography*. (VUBPress, Brussels, Belgium, 1997).

18   W. Koechner, *Solid-state laser engineering*, 5th rev. and updated ed. (Springer, Berlin ; New York, 1999).

19   D. S. Bethune, Appl. Opt. **20** (11), 1897 (1981).

[20] W. Wright and I.S. Falconer, Optics Communications **67** (3), 221 (1988).

[21] T. Chung, *Thermal management, beam control, and applications of high power diode laser arrays*. (University of Central Florida, Orlando, 2004).

[22] T. W. Cline and R. B. Jander, Applied Optics **21** (6), 1035 (1982).

[23] J. E. Kuneman and Joseph F. Doclspm, USA Patent No. 4563383 (1984).

[24] J. Bryzek, K. Petersen, and W. McCulley, IEEE Spectrum **31** (5), 20 (1994).